Isa Brandão

Towards the understanding of the deepest layers of solar-like pulsators

Departamento de Física e Astronomia
Faculdade de Ciências da Universidade do Porto
Setembro de 2012

Isa Brandão

Towards the understanding of the deepest layers of solar-like pulsators

Tese submetida à Faculdade de Ciências da
Universidade do Porto para obtenção do grau de Doutor
em Astronomia

Departamento de Física e Astronomia
Faculdade de Ciências da Universidade do Porto
Setembro de 2012

-

...to Sérgio, my parents and my grandmother...

Acknowledgements

I would like to start by thanking both my supervisors, Dra. Margarida Cunha and Prof. Dr. Jørgen Christensen-Dalsgaard, without whom the realization of this thesis would not have been possible. I would like to give a very special thank to Prof. Dr. Jørgen Christensen-Dalsgaard for his hospitality and unconditional support during my three month working visit at Aarhus University. Although his physical presence was not always possible during these four years of my PhD, he was always there whenever I needed.

I am very fortunate to have Dra. Margarida as my supervisor. Her enthusiasm, wisdom, encouragement, guidance and support have been invaluable to me. Thank you very much for everything.

I want to thank all of people that were involved directly or indirectly in this thesis, including those not mentioned here by name. I would like to give a very special thanks to all the people in my group in Centro de Astrofísica da Universidade do Porto, for helping and supporting me during my PhD. Particularly, I thank to Prof. Dr. Filipe Gameiro, Prof. Dr. Mário Monteiro, Dr. Michaël Bazot, Dr. Fernando Pinheiro and Dr. João Marques who showed to be always available for helping me in several topics regarding this thesis. I am indebted to all my collaborators, especially to those with whom I spent some time when I was abroad, namely Gülnur Doğan and Orlagh Creevey.

A very special thanks goes also to Nelma Silva and Joana Sousa for their unconditional support. I would like to thank all my office colleagues for the very funny moments and fruitful conversations. They gave me huge support at the last stages of my thesis writing, namely Arlindo Trindade, Elsa Ramos, Vasco Neves, Tiago Campante, Ana Lameiras, David Oliveira and Pedro Almeida.

I would like to thank to my family and relatives from all of my heart, my parents and Sérgio. I special thank my mother for her patience, love and support during my life and my grandmother for her faith and love (miss you). I heartily thank Sérgio for his love, patience, support, encouragement, and help throughout this entire journey. Days would not have been

easy without you...I am also very grateful to D.ª Maria José for everything, to Dr. Abel Magalhães and Dra. Paula Pires. I thank Tareco and Furna for their existence and Neale Walsch for his words of wisdom.

I am indebted to FCT for its finantial support through a grant SFRH / BD / 41213 /2007, and also to the project PTDC/CTE-AST/098754/2008. I gratefully acknowledge my host institution, Centro de Astrofísica da Universidade do Porto, for the facilities provided me during my PhD. I also acknowledge the hospitality at Aarhus University and Instituto de Astrofísica de Canarias where I was very well received during my working visit. A special thanks goes to Anette Skovgaard and Dr. Pere L. Pallé.

I also would like to give a special thank to Dr. Andrea Miglio and Dra. Maria Pia di Mauro for their interest in my work and for agreeing to be my thesis reporters.

Summary

With the recent launch of the *Kepler* satellite, thousands of stars are being monitored to provide high-quality seismic data. These seismic data combined with non-seismic surface stellar observables can provide valuable information about the global properties of pulsating stars, such as their mass, radius and age. Nevertheless, it is in their interiors, inaccessible to our eyes, that most of the information regarding stellar structure and evolution is contained. This information may be inferred from asteroseismic studies. In particular, the deepest layers of a star, namely the stellar core, are of great importance in that context. For the reason just mentioned, significant effort has been put into the development of seismic diagnostic tools, i.e. combination of oscillation frequencies, in order to extract information about the interior of pulsating stars.

The work presented in this dissertation deals with the analysis of the potential that the non-seismic, but mostly the seismic data, obtained for pulsating stars can provide about their interiors.

Chapter 1 introduces the two type of pulsators that will be focus of this thesis, namely the rapidly oscillating A peculiar (roAp) stars and the solar-type pulsators. It gives an overview on asteroseismology, how it can be applied to derive stellar properties, and the present status of the field. It also gives a general overview of the basic physics and properties of stellar pulsators and the potential of asteroseismic inference.

In Chapter 2, I adress the problem of the computation of the bolometric flux of chemically peculiar stars which is of relevance for the study of a particular class of pulsating stars, namely the roAp stars. The resulting value for the bolometric flux can be used to accurately determine two fundamental parameters of the stars, namely their effective temperature and luminosity. I present the results obtained by applying this method to two particular roAp stars.

In Chapter 3, I adress the problem of forward modelling of solar-like pulsators. I present results on the modelling of three pulsators of this type based on non-seismic and seismic

data. Due to our inability to model properly the surface layers of stars, the frequencies of the model that best represents the internal structure of a star are shifted in relation to the observed ones. The empirical formulation that has been suggested in the literature to correct for this shift was considered and its successfulness is discussed.

Chapter 4 concerns the study of small convective cores that might be present at some stages during the main-sequence evolution of stars slightly more massive than the Sun. Three diagnostic tools suggested in the literature were computed from the oscillation frequencies for a large set of stellar models to check what information they hold about stellar cores. The dependence of these diagnostic tools on the mass, age and different physics considered in the models is discussed.

Finally, in Chapter 5, I summarize the results obtained in the three previous chapters.

Sumário

Com o recente lançamento do satélite *Kepler,* milhares de estrelas estão a ser monitorizadas com o objetivo de se obterem dados sísmicos de alta qualidade. Estes dados sísmicos combinados com os dados observacionais clássicos, podem fornecer informação valiosa acerca das propriedades globais das estrelas variáveis, como a sua massa, raio e idade. No entanto, é no seu interior, inacessível aos nossos olhos, que se encontra a maior parte da informação relativa à estrutura e evolução estelar. Esta informação pode ser inferida através de estudos sísmicos. Em particular, as camadas mais internas de uma estrela, nomeadamente o núcleo, são de grande importância neste contexto. Por esta razão, tem sido feito um enorme esforço no sentido de desenvolver ferramentas de diagnóstico sísmico, i. e. combinações de frequências de oscilações, de modo a se extrair informação acerca do interior de estrelas variáveis.

O trabalho apresentado nesta dissertação lida com a análise dos dados obtidos de estrelas variáveis, mas principalmente com o potencial dos dados sísmicos que, podem fornecer informações únicas acerca do interior das estrelas.

O Capítulo 1 introduz os dois tipos de estrelas pulsantes que serão o foco nesta tese, nomeadamente as estrelas tipo A peculiares que oscilam muito rapidamente (roAp) e as estrelas pulsantes tipo solar. Fornece uma visão global da asterosismologia, descrevendo como é usada para derivar propriedades estelares e relatando o seu estado de arte atual. Também fornece uma visão global da física básica e das propriedades das estrelas pulsantes e o potencial das inferências asterosísmicas.

No capítulo 2, é abordado o problema do cálculo do fluxo bolométrico de estrelas quimicamente peculiares, que é relevante para o estudo de uma classe particular de estrelas pulsantes, nomeadamente as estrelas roAp. O valor calculado para o fluxo bolométrico pode ser usado para determinar, de um modo exato, dois parâmetros fundamentais das estrelas, nomeadamente a temperatura efetiva e luminosidade. Este método é aplicado a duas estrelas roAp particulares e são apresentados os resultados.

No capítulo 3, é abordado o problema da modelação de estrelas pulsantes tipo solar. São apresentados os resultados obtidos na modelação de três estrelas pulsantes deste tipo baseado nos dados não sísmicos e sísmicos. Devido à nossa incapacidade de modelar as camadas mais externas das estrelas, existe um desvio entre as frequências calculadas para o modelo que melhor representa a estrutura interna de uma estrela e as frequência observadas. Consideramos a formulação empírica que foi sugerida na literatura para corrigir esse desvio discutindo a sua aplicação e o seu sucesso.

O capítulo 4 lida com o estudo de pequenos núcleos convectivos que poderão existir nalguns estados de evolução, ao longo da sequência principal, de estrelas ligeiramente mais massivas que o Sol. Três ferramentas de diagnóstico sugeridas na literatura foram calculadas a partir das frequências de oscilação, para um conjunto grande de modelos estelares, de modo a verificar-se que informação detêm acerca dos núcleos estelares. Discutiu-se a dependência destas ferramentas de diagnóstico na massa, idade e diferente física considerados nos modelos.

Finalmente, no capítulo 5, é sumariado os resultados obtidos nos três capítulos anteriores.

Contents

List of Tables

List of Figures

Chapter 1

Introduction

Stars are the source of life. Most of the elements that we are made of are produced in the central regions of the stars, well in their deep interiors, during the main-sequence and post-main-sequence phase of the life of a star. It is in the stellar core that nuclear reactions occur, the lighter elements being fused into heavier ones thus sustaining the star's life. These elements are released into the star's surroundings after its death. But, how can we probe the inner regions of a star when all the light that we receive from it is emitted in the superficial layers, thus having no memories of the star's interior? Asteroseismolgy, the study of "stellarquakes" is the answer to this question, as it can provide us with invaluable information about the stellar's interior, that would otherwise be out of reach.

Asteroseismology is a technique used for the study of pulsating stars, i.e. stars that oscillate due to waves propagating within their interiors. As seismic waves generated by earthquakes propagating through the Earth's interior provide us with valuable information about the inner structure of our planet (e.g., Montagner & Roult 2008; Rawlinson et al. 2010; Khan et al. 2011), the study of stellar pulsations provide us with an unique opportunity to probe the interior of the stars (e.g., Aerts et al. 2010). In particular, information about the deepest layers of pulsating stars is of great importance since this region is determinant for their evolution. Through providing this information, asteroseismology provides us also with the opportunity to improve our understanding of stellar structure and evolution.

The first detections of the oscillatory motion in the atmosphere of the Sun, as local modes, were made in the early 1960s by Leighton et al. (1962). This has opened a new era in our understanding of the Sun's internal structure and dynamics, paving the way for the development of a new research field, known as helioseismology. The first detections and identification of solar oscillations, as global modes, is attributed to Claverie et al. (1979).

Helioseismology has proved to be very successful in probing the internal structure of our Sun. The vast amount of data on solar oscillations collected over the past two decades made possible a considerably accurate determination of the Sun's internal sound speed (c) and density (ρ) profiles, the determination of the location of the solar helium second ionization zone and the base of the convective envelope, the detailed testing of the equation of state and the inference of the solar internal rotation (e.g., Christensen-Dalsgaard 2002; Basu & Antia 2008; Chaplin & Basu 2008; Howe 2009, and references therein).

Many stars other than the Sun are known to pulsate since the early years of the 20th century. The study of pulsations in these stars led to the development of asteroseismology. However, by that time, only high amplitude (or classical) oscillations could be detected. These oscillations, unlike the case of solar oscillations, are intrinsically unstable, resulting from the growing of small disturbances.

The detection of solar-like oscillations in stars other than the Sun had long been an illusory goal due to their very small amplitudes. However, with the development of very precise spectrometers such as HARPS at the ESO La Silla 3.6-m telescope and UVES at the 8.2-m UT2 of the VLT at ESO Paranal in Chile[1], CORALIE at the 1.2-m Euler telescope on La Silla[2] , SARG at the 3.6-m TNG in La Palma[3] and UCLES at the 3.9-m AAT in Australia[4], clear detections of oscillations in solar-like stars were finally possible in the beginning of the 21st century, opening, just as solar oscillations did for the study of the Sun, a new era in the research field of stellar structure and evolution. In fact, the search for solar-like oscillations in stars other than the Sun began in the early 1980s through ground-based observations, but the first detection of such oscillations only occurred in 1995 for the G0IV star η Boo (Kjeldsen et al. 1995). Since then, several other detections of solar-like oscillations have been made from the ground (Bedding & Kjeldsen 2003; Bedding et al. 2007). Nevertheless, the great development of asteroseismology occurred as a result of observations of stellar oscillations from the space, with the advantage of having long and almost uninterrupted seismic data of the same targets. Three space missions with programmes dedicated to asteroseismology have been launched, namely the Canadian-led MOST[5] satellite launched in June 2003 (Walker et al. 2003), the french-led CoRoT[6] satellite launched in December 2006 (Baglin et al. 2006), and the NASA *Kepler*[7] mission launched in March 2009, which is essentially aimed at detecting planetary transits, but includes also

[1] http://www.eso.org/public/.
[2] http://obswww.unige.ch/ naef/CORALIE/coralie.html.
[3] http://www.tng.iac.es/instruments/sarg/.
[4] http://www.aao.gov.au/astro/ucles.html.
[5] http://www.astro.ubc.ca/MOST/index.html.
[6] http://corot.oamp.fr/.
[7] http://www.kepler.arc.nasa.gov/.

an asteroseismic programme (Borucki et al. 2010; Koch et al. 2010). In particular, with the recent launch of the *Kepler* satellite, pulsations were discovered in thousand of stars and hundreds are being continuously monitored with the aim of characterizing their oscillations to a very high degree of precision. An overview of the most important results obtained so far with *Kepler* is provided by Garcia (2011).

In addition to these space missions, studies on the ground are being carried out with the aim of developing the Stellar Oscillations Network Group (SONG)[8] - a network of telescopes positioned on different longitudes in the globe which will acquire, continuously, high-precision radial velocities of solar-like pulsators (Grundahl et al. 2009a,b).

The existence of such tremendous seismic data provides today an unique opportunity to apply asteroseismic diagnostic tools in order to extract some of the information that the oscillations may hold about the interior of the stars. Note that unlike the case of the Sun, for which modes of very high degree l can be observed, only modes of low-degree ($l \leq 3$) are expected to be observed for all solar-like pulsators. This is a consequence of our inability to resolve the stellar disk which results in a geometric cancellation, also known as partial cancellation or spatial filtering, of the amplitudes of the modes of moderate and high degree l. Fortunately, the modes of degree $l \leq 3$ are the ones that penetrate in the inner regions of a star, thus carrying information about these regions.

Since most of the stars are believed to pulsate at some stage of their evolution, asteroseismology can be applied to study different types of oscillations in different types of stars. Figure 1.1 shows the position of the different classes of pulsating stars across the Hertzsprung-Russel (HR) diagram, which shows the luminosity, L, versus the effective temperature, $T_{\rm eff}$, of stars. In this work we will focus on the study of rapidly oscillating A peculiar stars (roAp stars) and solar-like pulsators.

Origin and nature of stellar pulsations

A relevant timescale for the understanding of the properties of oscillations is the dynamical timescale:

$$t_{dyn} \simeq \left(\frac{R^3}{GM}\right)^{1/2} \simeq (G\bar{\rho})^{-1/2}, \tag{1.0.1}$$

where R and M are the surface radius and mass of the star, respectively, G is the gravitational constant, and $\bar{\rho}$ is the mean stellar density. More specifically, t_{dyn} expresses the time the star needs to go back into hydrostatic equilibrium whenever some dynamical process breaks the balance between pressure and gravitational force. The periods of the oscillations generally scale as t_{dyn}. Is it noticeable that a measurement of a period of oscillation immediately

[8] astro.phys.au.dk/SONG.

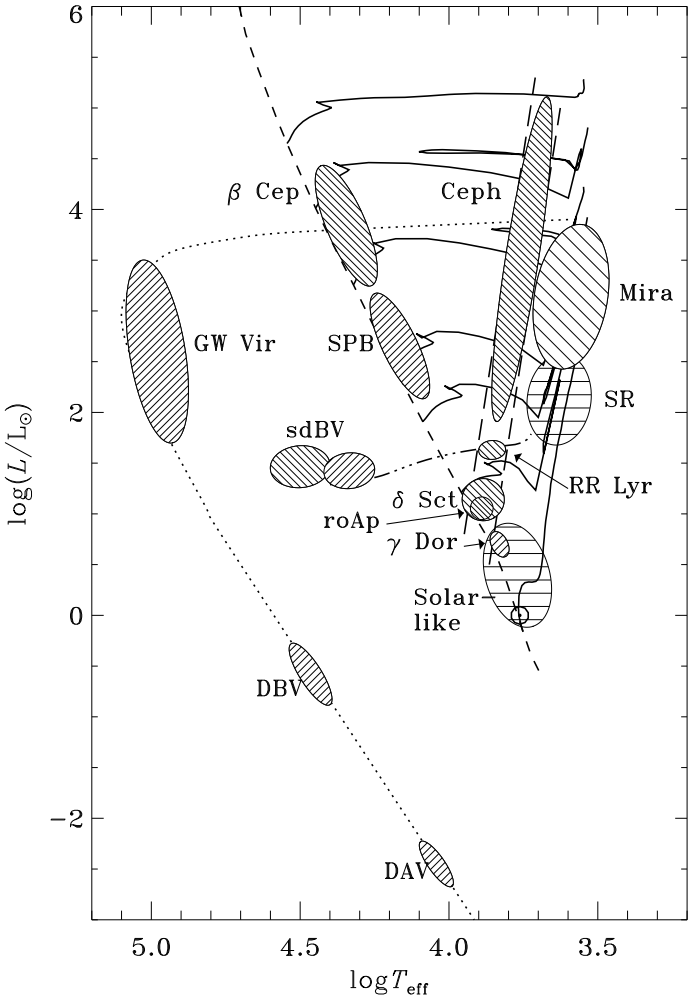

Figure 1.1: Position of several classes of pulsating stars in a HR diagram. $T_{\rm eff}$ and L are the effective temperature and stellar luminosity, respectively. The dashed line indicates the zero-age main sequence (ZAMS), the solid curves represent selected evolutionary tracks (for 1, 2, 3, 4, 7, 12, and 20 $M_\odot$), the triple-dot-dashed line indicates the horizontal branch and the dotted curve follows the white-dwarf cooling track. The parallel long-dashed lines enclose the Cepheid instability strip. RoAp stars are located right in the instability strip for classical pulsators, like Cepheids, RR Lyrae and δ Scuti, with effective temperature ranging between 7000 and 8500 K and masses around 2 solar masses. Main-sequence solar-like pulsators are less massive than roAp stars. (image available at www.phys.au.dk/jcd/HELAS/puls_HR/index.html).

provides us with an estimate of an overall property of a star, i.e. its mean density.

The physical nature of stellar pulsations is twofold: standing acoustic waves (p modes) or internal gravity waves (g modes). These depend on the restoring force at play: for the former being the pressure and for the latter buoyancy. There is a clear separation between these two classes of modes in unevolved stars. This, however, may not be the case in evolved stars, as it will be explained later. In the case of p modes most of the energy is contained in a region close to the surface, whereas for the g modes the energy is confined to the inner regions of the star. In addition, there is an intermediate fundamental mode, the f mode, which is essentially a surface gravity mode.

The origin of stellar oscillations is determined by their driving mechanism. Oscillations can be either intrinsically unstable, or intrinsically stable. In the former case, oscillations result from the amplification of small disturbances by means of a heat-engine mechanism converting thermal into mechanical energy in a specific region of the star, usually a radial layer. This region is heated up during the compressional phase of the pulsation cycle while being cooled off during expansion. An amplitude-limiting mechanism then sets in at some point, determining the final amplitude of the growing disturbance. The heat that is stored in the radial layer during the compression phase drives the pulsations. Such a region inside the star is typically associated with opacity (κ) rapid variations and the resulting driving mechanism is thus known as the κ-mechanism. Rapid variations of the opacity usually occur at ionization regions. For instance, the driving of pulsations in the classical Cepheids and other stars in the Cepheid instability strip is associated to the regions of the second ionization of helium, while for roAp stars it is associated with the region of hydrogen ionization (e.g., Cunha 2002). In order to cause overall excitation of the oscillations, the region associated with the driving has to be placed at an appropriate depth inside the star, thus providing an explanation for the specific location of the resulting instability belt in the HR diagram (see Figure 1.1). This type of oscillations are generally known as classical oscillations.

Intrinsically stable oscillations, such as those of the Sun, are stochastically excited and intrinsically damped by the vigorous near-surface convection (Houdek 2006). These oscillations, known as solar-like oscillations, are predicted for all stars cool enough ($T_{\rm eff} \lesssim 6500\,{\rm K}$) to harbor an outer convective envelope. Solar-like oscillations may be present in main-sequence stars with masses up to $\sim$1.6 $M_\odot$[9] (e.g., Christensen-Dalsgaard 1982; Christensen-Dalsgaard & Frandsen 1983; Houdek et al. 1999), and also in stars at the end of the main sequence up to the giant and asymptotic giant branches (Dziembowski et al. 2001). They show extremely low amplitudes when compared to those of classical oscillations.

[9]Recently, it was observed what is believed to be solar-like oscillations in a δ Scuti star, which may have a mass of $\sim 1.9\,M_\odot$, sligthly higher than $1.6\,M_\odot$ (Antoci et al. 2011)

Rapidly oscillating Ap stars vs Solar-like pulsators

Rapidly oscillating A peculiar stars (roAp stars) are main-sequence chemically peculiar stars of spectral type A (and sometimes F). Their peculiarity results from the inhomogeneous atmospheric abundance of the chemical elements, particularly of rare earth elements. They show strong global magnetic fields with polar field strengths typically of several kG, but up to 24.5 kG (Hubrig et al. 2005; Kurtz et al. 2006). They are classical pulsators, which exhibit oscillations with amplitudes of a few mmag (varying typically from 0.3 to 8 mmag, about two orders of magnitude greater than the amplitudes of the oscillations found in the Sun) and frequencies typically ranging from 1 to 3 mHz. Among about 40 roAp stars already discovered, many are known to pulsate in only one single mode. There are, however, some that show multiperiodic variations. In either case, the oscillations correspond to high order, n, low degree, l, acoustic pressure, p modes.

The oscillation spectrum of these stars looks somewhat similar to that of the 5 minutes solar oscillations (cf. Figure 1.2), except in that the oscillation amplitudes are much larger, and many modes are missing. The multiperiodic roAp stars are of special interest in asteroseismology since through the analysis of their oscillation spectrum it is, in principle, possible to infer about their internal properties.

In solar-like pulsators the frequency spectrum shows a comb-like structure as that observed in the Sun, with many modes excited modulated by an envelope typical of stochastically excited oscillations (Figure 1.2). The frequency at which the envelope has a maximum value is frequently denominated as the frequency of maximum power, $\nu_{\max}$. This frequency is supposed to scale with the acoustic cut-off frequency, ν_c (see below).

Stellar pulsations' properties

There are different natural oscillation modes that stars can pulsate in. The frequencies of these normal modes are the star's natural frequencies and are also known as eigenfrequencies. The simplest natural oscillation modes are the radial modes. The star periodically expands and contracts, heats and cools, while preserving its spherical symmetry. On the other hand, non-radial pulsations cause a deviation from the spherical symmetry of a star, thus generating distortions of the stellar surface. Again, these distortions represent expanding and receding areas in the stellar surface, and they can be described by spherical harmonics, $Y_l^m(\theta,\phi)$, or a combination of them. Between the expanding and receding surface areas, no motion takes place. These regions are known as nodes. The spherical harmonic functions provide the nodes of the standing wave patterns.

Since stars are 3-dimensional (3-D) objects their natural oscillation modes have nodes in

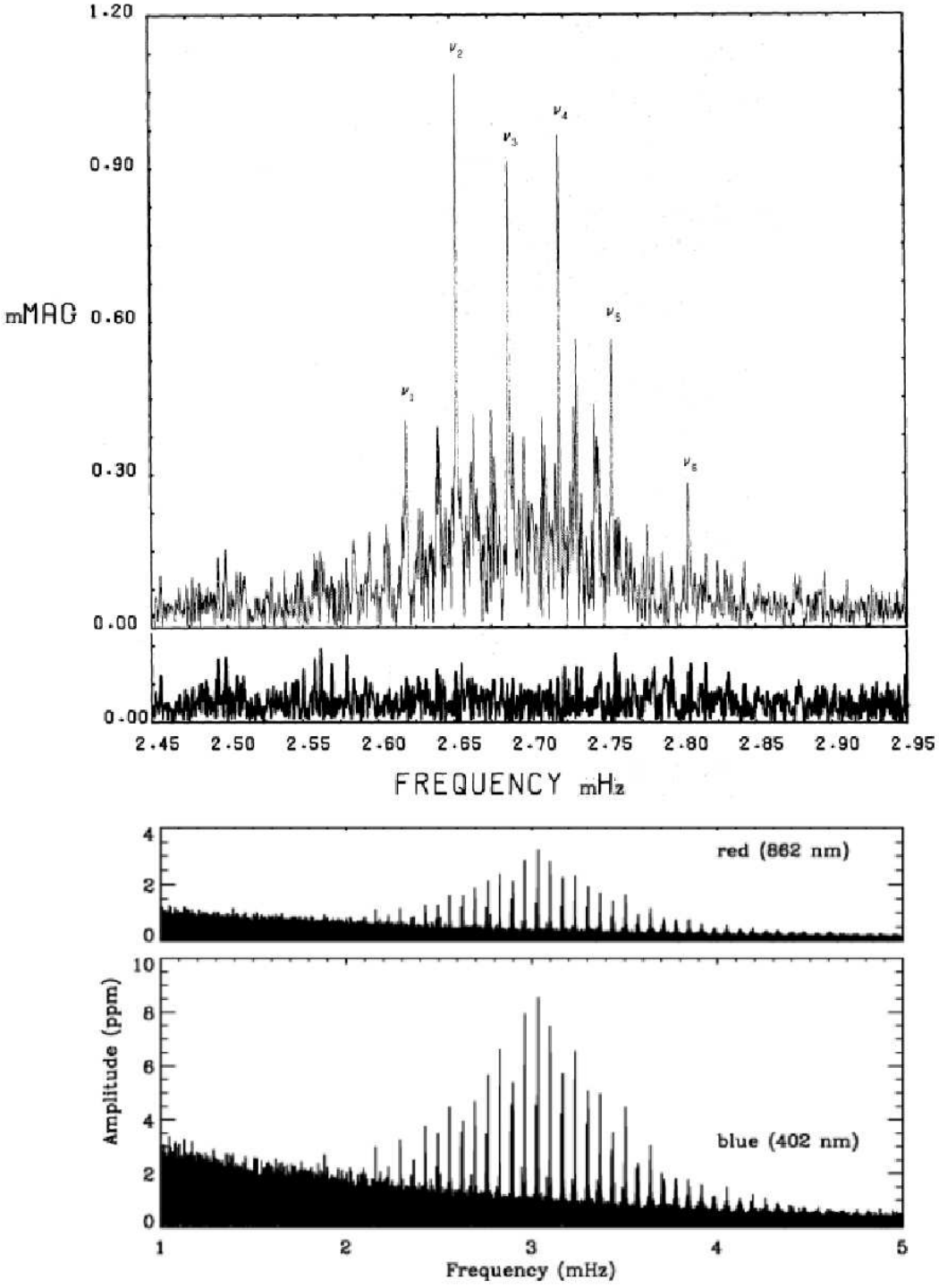

Figure 1.2: The oscillation frequency of the JD 2246738 - 2446753 *B* multi site data of the roAp star HR 1217 (upper Figure). The principal frequencies ν_1 to ν_6 are labelled. The noise level is shown in the bottom panel of the same figure (from Kurtz et al. 1989). For comparison, the oscillation spectra of the Sun in two different filters is presented in the lower two panels. The VIRGO instrument aboard the SOHO spacecraft observed the Sun as a star through full-disk intensity measurements. A Fourier Transform of these data over a 30 day time baseline reveals many individual oscillation modes (from Frohlich et al. 1997; Bedding & Kjeldsen 2003). Note that 1 mMAG $\sim$ 1000 ppm.

three orthogonal directions. Use is made of spherical polar coordinates, (r, θ, ϕ), where r is the distance to the centre of the star, θ is the co-latitude (i.e. measured from the pulsation pole, the axis of symmetry) and ϕ is the longitude. The nodes are concentric shells at constant r, cones of constant θ and planes of constant ϕ. For a spherically symmetric star the solutions to the equations of motion have displacements in the (r, θ, ϕ) directions. As an example, the radial component of the displacement may be expressed as

$$\xi_r(r, \theta, \phi) = \Re\{a(r)Y_l^m(\theta, \phi)e^{-i2\pi\nu t}\}, \tag{1.0.2}$$

where $a(r)$ in an amplitude function, and ν is the cyclic frequency of oscillation. In a spherical symmetric star the frequency of oscillation depends only on n and l, i.e., $\nu = \nu_{nl}$. The spherical harmonic, $Y_l^m(\theta, \phi)$, is given by

$$Y_l^m(\theta, \phi) = (-1)^m c_{lm} P_l^m(\cos\,\theta)e^{im\phi}, \tag{1.0.3}$$

where P_l^m is an associated Legendre function and c_{lm} is a normalization constant. I refer the reader to the book by Aerts et al. (2010) for a detailed description. The oscillation modes are, thus, characterized by three quantum numbers: the angular degree l, the azimuthal degree m and the radial order n. Here, l represents the number of lines dividing the stellar surface and $l \geqslant 0$, $|m|$ is the number of those that are longitudinal lines with m lying in the interval $[-l, l]$, and n is related to the number of nodes from the centre to the surface of each mode, and is called the overtone of the mode.

The propagation of the pulsation modes in the stellar interior depends on how their frequencies compares to two characteristic (angular) frequencies varying throughout the star, namely the acoustic (Lamb) frequency, S_l, and the buoyancy (Brunt-Väisälä) frequency, N. These two quantities are defined as:

$$S_l^2 = \frac{l(l+1)c^2}{r^2} \tag{1.0.4}$$

and

$$N^2 = g\left(\frac{1}{\Gamma_1}\frac{\mathrm{d}\ln p}{\mathrm{d}r} - \frac{\mathrm{d}\ln\rho}{\mathrm{d}r}\right), \tag{1.0.5}$$

where g is the local gravitational acceleration, c is the local sound speed, p is the pressure, ρ the density, r is the distance from the stellar centre and Γ_1 is the first adiabatic exponent given by,

$$\Gamma_1 = \left(\frac{\partial \ln p}{\partial \ln \rho}\right)_{\mathrm{ad}}. \tag{1.0.6}$$

The adiabatic sound speed is given by,

$$c^2 = \frac{\Gamma_1 p}{\rho} = \frac{\Gamma_1 K_{\mathrm{B}} T}{\mu m_u}, \tag{1.0.7}$$

where $K_{\rm B}$ is the Boltzmann constant, T the temperature, μ the mean molecular weight and m_u is the atomic mass unit. The second equality in c^2 is obtained under the approximation of an ideal gas. Also, under this approximation and for a fully-ionized gas, Eq. (1.0.5) can be written as,

$$N^2 \simeq \frac{g^2\rho}{p}(\nabla_{ad} - \nabla + \nabla_\mu), \tag{1.0.8}$$

where

$$\nabla = \frac{\mathrm{d}\ln T}{\mathrm{d}\ln p}, \nabla_{\rm ad} = \left(\frac{\mathrm{d}\ln T}{\mathrm{d}\ln p}\right)_{\rm ad}, \nabla_\mu = \frac{\mathrm{d}\ln\mu}{\mathrm{d}\ln p}, \tag{1.0.9}$$

are the temperature gradient, the adiabatic temperature gradient, and the μ gradient, respectively.

The Lamb and Brunt-Väisälä frequencies have the following implications regarding the mode propagation: for the motion to be oscillatory, its angular frequency, ω[10], must satisfy $|\omega| > |N|, S_l$ or $|\omega| < |N|, S_l$. The former condition corresponds to p-mode oscillations while the later corresponds to g-mode oscillations. On the other hand, for a vibration with $S_l < |\omega| < |N|$ or $|N| < |\omega| < S_l$, the energy of the wave decreases exponentially with distance from the p- and g-mode propagation regions. These regions are called evanescent regions. For a given mode of oscillation there may be several regions where the solution oscillates, with intermediate regions where it is exponential. But the dominant nature of the mode is determined by the region where most of the energy is contained, which is referred to as the trapping region. For $N^2 > 0$, N can be interpreted as the frequency of a gas element of reduced horizontal extent which oscillates due to buoyancy. Conversely, regions for which $N^2 < 0$ satisfy the Ledoux criterion of convective instability, i.e.,

$$\nabla > \nabla_{\rm ad} + \nabla_\mu. \tag{1.0.10}$$

Gravity waves cannot, therefore, propagate in convective regions.

In the superficial layers of a star, typically $\omega \gg S_l$, since S_l decreases monotonically towards the surface (due to an increase in r and a decrease in c), and the behaviour of the eigenfunction is thus controlled by the so-called acoustic cut-off frequency, ω_c,

$$\omega_c^2 = \frac{c^2}{4H_\rho^2}\left(1 - 2\frac{\mathrm{d}H_\rho}{\mathrm{d}r}\right), \tag{1.0.11}$$

where $H_\rho = -(\mathrm{d}\ln\rho/\mathrm{d}r)^{-1}$ is the density scale height. In an isothermal atmosphere, H_ρ is constant, hence Eq. (1.0.11) becomes

$$\omega_c = \frac{c}{2H_\rho} = \frac{\Gamma_1 g}{c}. \tag{1.0.12}$$

[10]Note that the angular frequency, ω, is related to the cyclic frequency, ν, through $\omega = 2\pi\nu$.

A useful relation, describing the behaviour of the acoustic cut-off frequency as a function of stellar parameters, is given by

$$\frac{\omega_c}{\omega_{c,\odot}} \simeq \frac{M/\mathrm{M}_\odot \left(\mathrm{T_{eff}}/\mathrm{T_{eff,\odot}}\right)^{3.5}}{L/\mathrm{L}_\odot}, \tag{1.0.13}$$

where $\omega_{c,\odot}$ is the acoustic cut-off frequency of the Sun. Moreover, the frequency of maximum amplitude, ν_{max}, is supposed to scale with the acoustic cut-off frequency (Brown et al. 1991; Kjeldsen & Bedding 1995; Bedding & Kjeldsen 2003; Chaplin & Basu 2008; Belkacem et al. 2011). Hence,

$$\frac{\nu_{\mathrm{max}}}{\nu_{\mathrm{max},\odot}} \simeq \frac{\nu_c}{\nu_{c,\odot}}, \tag{1.0.14}$$

with $\nu_c = \omega_c/2\pi$. It is observed for the Sun that $\nu_{c,\odot} \simeq 1.7\nu_{\mathrm{max},\odot}$ (Balmforth & Gough 1990; Fossat et al. 1992). The role of ω_c is important in the superficial layers, nonetheless, minor in the remaining of the star, where the properties of the eigenfunction are effectively controlled by S_l and N. The energy of modes with frequency below the atmospheric value of ω_c, decay exponentially in the atmosphere, the wave is reflected back to oscillate in the stellar envelope, hence being trapped inside the star.

In unevolved stars (e.g., like the Sun) the buoyancy frequency N remains with relatively low values throughout the star, thus the behaviour of a high frequency mode is mostly controlled by S_l. The eigenfrequency of such a mode will be trapped between the near-surface reflection determined by $\omega = \omega_c$ and an inner turning point located where $S_l(r_t) = \omega$, or

$$\frac{c^2(r_t)}{r_t^2} = \frac{\omega^2}{l(l+1)}, \tag{1.0.15}$$

with r_t being determined by l and ω. These are p modes. Low-frequency modes satisfy $\omega \ll S_l$ throughout most of the stellar radius. Under these circumstances the eigenfunction of a mode oscillates in a region approximately determined by $\omega < N$, hence to great extent independent of l. These are g-modes, having a turning point very near the centre of the star and a second one just below the base of the convection zone.

As the star evolves, the μ gradient, ∇_μ, increases due to an increase of the mean molecular weight, μ, with increasing pressure, p. Moreover, with evolution, the core of a star contracts when the hydrogen is exhausted in the core, leading to an increase of g. These two factors contribute to an increase in N. On the other hand, the p-mode frequencies decrease with evolution mainly due to the increasing stellar radius. As a consequence, the separation between the p-mode and g-mode cavities gets smaller, and the two modes undergo an avoided crossing (or, mode bumping), i.e., closely approaching without actually crossing (Osaki 1975; Aizenman et al. 1977). The modes that are affected by the avoided croosings are referred to as mixed modes due to having both p- and g-mode character. The

frequencies of these mixed modes are extremely sensitive to the evolutionary state of the star. Observational evidence for mixed modes, in the form of frequencies departing from the asymptotic relation (as it will be explained below), has been seen in evolved stars such as β Hyi and KIC 10273246, that will be described in Chapter 3.

The changing nature of the modes can be traced by means of the behaviour of their normalized inertia, E,

$$E = \frac{M_{\rm mode}}{M} \equiv \frac{\int_V \rho |\delta\mathbf{r}|^2 {\rm d}V}{M|\delta\mathbf{r}|^2_{\rm ph}}, \tag{1.0.16}$$

where the integration is over the volume V of the star, $M_{\rm mode}$ is defined as the modal mass, and $|\delta\mathbf{r}|^2_{\rm ph}$ is the squared norm of the displacement vector at the photosphere. The displacement, $\delta\mathbf{r}$, in terms of radial and horizontal components is given as $\delta\mathbf{r} = \xi_r \mathbf{a}_r + \boldsymbol{\xi}_h$, where ξ_r is defined in Eq. (1.0.2), $\mathbf{a}_r$ is the unit vector in the radial direction, and $\boldsymbol{\xi}_h$, the horizontal displacement, given by:

$$\boldsymbol{\xi}_h = \Re\left\{ b(r) \left(\frac{\partial Y_l^m}{\partial\theta}\mathbf{a}_\theta + \frac{1}{\sin\theta}\frac{\partial Y_l^m}{\partial\phi}\mathbf{a}_\phi \right) e^{-i2\pi\nu t} \right\}, \tag{1.0.17}$$

where $b(r)$ is an amplitude function, $\mathbf{a}_\theta$, $\mathbf{a}_\phi$ are the unit vectors in the θ and ϕ directions, respectively. Based on the definition of mode inertia one expects modes trapped in the deep stellar interior, as the g-modes, to have large values of E. On the other hand, modes trapped near the surface, such as the p modes, would have small normalized inertia. As for the mixed modes, their normalized inertia is larger than that of the p modes due to the fact that they have a g-mode character in the core of the star.

Asymptotic signatures

Both the solar-like oscillations and the oscillations observed in roAp stars are typically low degree high-order acoustic modes. If interaction with a g-mode region can be neglected, these satisfy an asymptotic relation for the frequencies (e.g., Vandakurov 1967; Tassoul 1980; Gough 1993) usually written in terms of the cyclic frequency $\nu = \omega/2\pi$,

$$\nu_{nl} \simeq \left(n + \frac{l}{2} + \frac{1}{4} + \alpha \right) \Delta\nu_0 - [Al(l+1) - \delta]\frac{\Delta\nu_0^2}{\nu_{nl}}, \tag{1.0.18}$$

where

$$\Delta\nu_0 = \left(2\int_0^R \frac{{\rm d}r}{c} \right)^{-1} \tag{1.0.19}$$

is the inverse sound travel time across a stellar diameter, and

$$A = \frac{1}{4\pi^2\Delta\nu_0}\left[\frac{c(R)}{R} - \int_0^R \frac{{\rm d}c}{{\rm d}r}\frac{{\rm d}r}{r} \right]; \tag{1.0.20}$$

also, α (which in general is a function of frequency) is determined by the reflection properties near the surface and δ is a small correction term predominantly related to the near-surface region. To leading order, neglecting the last term, Eq. (1.0.18) predicts a uniform spacing of modes of the same degree. This difference in frequency of modes of the same degree and consecutive order $\Delta\nu_{nl} = \nu_{n+1l} - \nu_{nl}$ is known as the *large frequency separation* and is, to leading order, approximately equal to $\Delta\nu_0$. Also, modes of the same $n + l/2$ are degenerate to this approximation. The departure from this degeneracy, is reflected in the *small frequency separation*

$$\delta\nu_{nl} = \nu_{nl} - \nu_{n-1l+2} \simeq -(4l+6)\frac{\Delta\nu_0}{4\pi^2\nu_{nl}}\int_0^R \frac{\mathrm{d}c}{\mathrm{d}r}\frac{\mathrm{d}r}{r}, \tag{1.0.21}$$

where the term in the surface sound speed $c(R)$ in Eq. (1.0.20) has been neglected.

Owing to the factor r^{-1} in the integral in Eq. (1.0.21) the small separation is very sensitive to the sound-speed structure of the stellar core. The dependence of the sound speed on the chemical composition makes the small frequency separations sensitive to the age of the star. Also, the average $\Delta\nu_0$ of the large frequency spacing is a measure of the mean density of the star.

Moreover, it may be also convenient to consider small separations that take into account modes with adjacent degree:

$$\delta^{(1)}\nu_{nl} = \nu_{nl} - \frac{1}{2}\left(\nu_{n-1l+1} + \nu_{nl+1}\right) \approx -(2l+2)\frac{\Delta\nu_0}{4\pi^2\nu_{nl}}\int_0^R \frac{\mathrm{d}c}{\mathrm{d}r}\frac{\mathrm{d}r}{r}, \tag{1.0.22}$$

i.e., the amount by which modes with degree l are offset from the midpoint between the $l+1$ modes on either side. As for the small frequency separation, $\delta\nu_{nl}$, $\delta^{(1)}\nu_{nl}$ is very sensitive to the stellar age. Thus, $\delta\nu_{nl}$ and $\delta^{(1)}\nu_{nl}$ can be seen as diagnostic tools of the evolutionary stage of a main-sequence star.

A common way of visualizing the asymptotic properties of the acoustic spectrum is to build an *échelle* diagram. This diagram shows the frequency spectrum divided into segments equally spaced by the large frequency separation, after these segments are stacked in the vertical direction (Grec et al. 1983). That is, starting by expressing the frequencies as

$$\nu_{nl} = \nu_0 + k\langle\Delta\nu\rangle + \tilde{\nu}_{nl}, \tag{1.0.23}$$

where ν_0 is a reference frequency, $\langle\Delta\nu\rangle$ is a suitable average of the large frequency separation $\Delta\nu_{nl}$, and k is an integer such that the reduced frequency, $\tilde{\nu}_{nl}$, takes the value between 0 and $\langle\Delta\nu\rangle$. The échelle diagram represents $\nu_0 + k\langle\Delta\nu\rangle$ as a function of $\tilde{\nu}_{nl}$. An example of such a diagram is illustrated in Figure 1.3 where the observed solar p-mode frequencies of $l \leq 3$

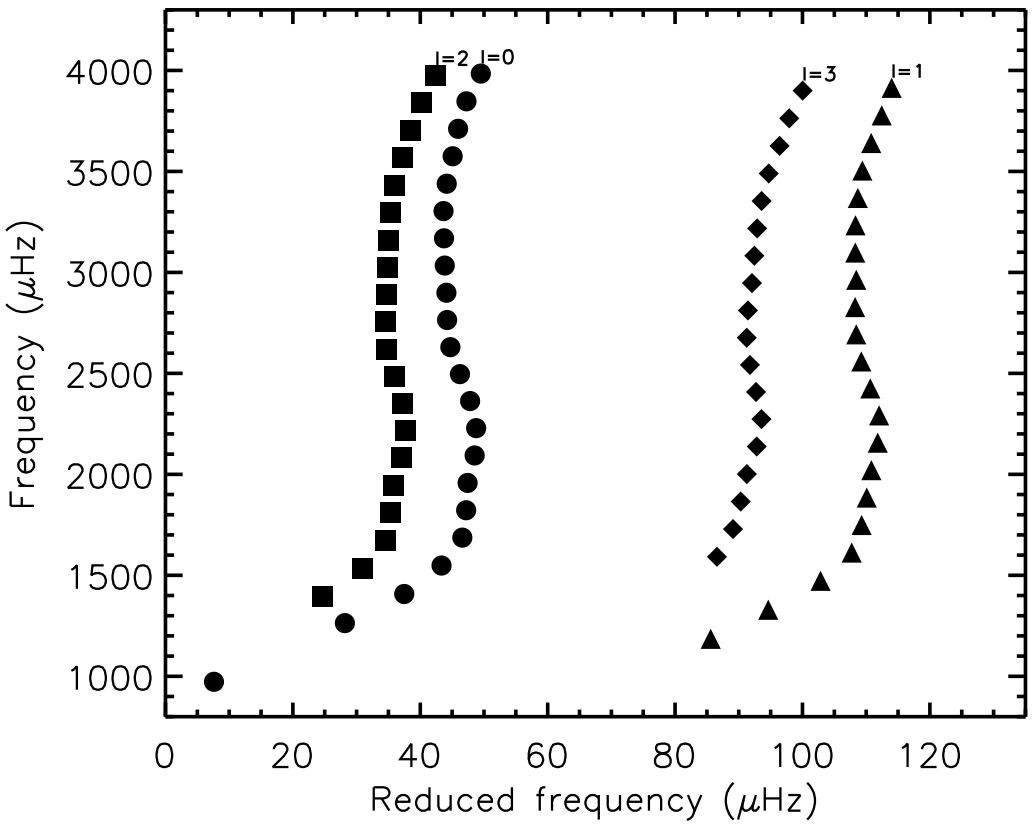

Figure 1.3: Échelle diagram for the observed solar p-mode frequencies obtained with the BiSON network (Broomhall et al. 2009), plotted with $\nu_0 = 830\,\mu$Hz and $\langle\Delta\nu\rangle = 130\,\mu$Hz (cf. Eq. 1.0.23). Different symbols indicate different mode degrees, namely, $l = 0$ (circles), $l = 1$ (triangles), $l = 2$ (squares) and $l = 3$ (diamonds).

are plotted. If the frequencies of a star were to strictly obey the asymptotic relation in Eq. (1.0.18), then they would appear very close to vertical ridges in the échelle diagram. However, when looking at échelle diagrams constructed from the observed frequencies of real stars departures from the regularity are clearly present. Variations in the large separation with frequency are seen to introduce a curvature in the ridges, while variations in the small separation with frequency appear as a convergence or divergence of the relevant ridges. The situation is even more dramatic, when an échelle diagram is constructed from frequencies of evolved stars. Significant departures from the asymptotic relation are expected for these stars due to the presence of frequencies with mixed character.

Asteroseismic inference

Stellar oscillations can provide valuable information about the properties of a pulsating star. The most basic seismic diagnostic tools, i.e. combination of frequencies that provide information of the interior of a star, are the above mentioned large and small frequency separations. They provide an estimation of the stellar mean density and age, respectively. There are, however, several methods for asteroseismic inference, i.e. for obtaining information about a star from its pulsations. I will mention three of them, namely the forward modelling, inference of regions of sharp structural variations, and inversion. For a detailed review see, e.g., Cunha et al. (2007).

Forward modelling, or *direct fitting*, consists in computing a set of evolutionary models using a stellar structure and evolution code. The code outputs at each step along the evolution a set of models' observables, which can be compared with the measured ones. The code also gives detailed numerical information on the internal structure of the (model) star. The model that has the model observable parameters closest to the observed ones, gives, in principle, valuable information on the global, as well as the internal properties of the star to which it is being compared. Usually, the observed parameters used as constraints are the 'classical', or often called the non-seismic constraints, such as the effective temperature, luminosity, metallicity, and radius, and the seismic ones, such as the large and small frequency separations. Brown et al. (1994) found that the inclusion of the individual frequencies as constraints for the modelling can provide lower uncertainties in the derived parameters. However, the individual frequencies are not always possible to detect, and the model frequencies are often affected by the near-surface layers of the stars that we still fail in correctly modelling, as we will mention in Chapter 3. So, the main problem associated to this approach relates to the physics included in the model, which are often too simplistic in relation to the physics that occurs in real stars. However, such comparison is potentially very valuable in order to improve the physics included in the models.

Once having a stellar model and the proper frequencies of its oscillation modes computed, one can determine the set of model observables, $y_i^{\rm mod}(\mathbf{a}), i = 1, N$, that correspond to the observed values of the observations, $y_i^{\rm obs}$. Here, the vector $\mathbf{a}$ corresponds to the model parameters that one has computed, namely the mass, age, chemical composition, overshooting parameter and the mixing length para meter. Thus, the direct fitting approach consists in firstly assess the agreement between $y_i^{\rm obs}$ and $y_i^{\rm mod}(\mathbf{a})$, and secondly change the set of model parameters, $\mathbf{a}$, in order to improve the fit. The common procedure to approach this problem is to apply a least-squares minimization method, where one searches the model parameters, $\mathbf{a}$, that minimize the χ^2 function, defined as

$$\chi^2 = \sum_{i=1}^{N} \left[\frac{y_i^{\rm obs} - y_i^{\rm mod}(\mathbf{a})}{\sigma_i} \right]^2 , \tag{1.0.24}$$

with σ_i being the standard deviation of the measured observable, $y_i^{\rm obs}$.

As for the possible optimization methods to obtain a model that best reproduces the observables one has the 'Grid of models' and the 'Levenberg-Marquardt' methods. The most commonly used is the grid modelling method and it consists in the computation of a grid of models with different input parameters and physics. For each set of model parameters the χ^2 function is evaluated. The set of parameters that minimize this function represents the 'best model'. There is a major problem associated to this method. As the number of models to be computed and/or the number of free parameters increase (for one to explore a refined grid within a large parameter space), the calculation time of the grid of models becomes too large for today's computers. On the other hand, the computation of a grid of models allows one to identify possible secondary minima. In the 'Levenberg-Marquardt' method (e.g., Bevington & Robinson 2003), the problem associated to the time of computation of the models becomes reduced. This method consists in an iterative procedure that rapidly converges to a χ^2 minimum by combining a gradient search when far from a minimum with an expansion of the χ^2 surface near the minimum. The main problem is to assess if the minimum is, in fact, a global minimum. For that, several searches with different starting values of the input parameters should be carried out as it is done by the genetic algorithms (e.g., Metcalfe et al. 2009) or Markov Chain Monte Carlo (MCMC) techiques (e.g. Bazot et al. 2012).

This forward approach with the 'Grid of models' optimization method will be applied in Chapter 3.

Sharp structural variations within a star, such as those that occur at the base of convective envelopes or at the edge of convective cores give rise to detectable oscillatory variations in the frequencies which are superimposed on the asymptotic formulation given in Eq. (1.0.18).

Several studies are focused in providing seismic tools aimed at inferring information from those regions. For instance, a discontinuity or a sharp variation in the chemical profile of a star generates a discontinuity or a sharp variation in the adiabatic sound speed, which, in turn, introduces an oscillatory signal in the oscillation frequencies (Vorontsov 1988; Gough 1990; Provost et al. 1993). Several authors have analysed this type of signal in order to estimate the location of sharp variations such as the boundaries of convective envelopes (Monteiro et al. 2000) or the regions of ionization (Monteiro & Thompson 1998; Houdek & Gough 2007). In the same manner, studies of the signal produced by sharp variations at the edge of stellar or planet cores have been carried out by several authors (e.g., Provost et al. 1993; Roxburgh & Vorontsov 1999, 2001, 2007; Cunha & Metcalfe 2007; Miglio et al. 2008). Of the latter, only the work of Roxburgh & Vorontsov (2007) and of Cunha & Metcalfe (2007) were directed towards the study of main-sequence solar-like pulsators. Based on a theoretical analysis of the signal produced by the edge of the core in the oscillation frequencies, and on simulated data, Cunha & Metcalfe (2007) have shown that such signal should be detected when the data for solar-like pulsators reaches the level of precision expected from space-based dedicated instruments, such as *Kepler*, and that the detection of the expected signal in real data of solar-like pulsators may provide unprecedented information about the cores of these stars. We will discuss this further when presenting our study on the convective cores, in Chapter 4.

Finally, the *inverse* methodology aims at determining localized information about the stellar structure or dynamics from the combination of different seismic data. Since this methodology will not be the focus of any Chapter of this thesis, we refrain from discussing it here and we point to the reader for the review by Cunha et al. (2007) to an overview of this methodology.

Chapter 2

Global stellar parameters of pulsating stars

2.1 Introduction

Stellar models are based on a set of fundamental parameters that describe the (model) star, such as the mass M, the luminosity L, the radius R and the chemical composition. One may also consider another three important stellar quantities, the effective temperature $T_{\rm eff}^4 = L/4\pi R^2\sigma$, where σ is the Stefan-Boltzmann constant, the surface gravity $g = GM/R^2$, where G is the gravitational constant, and the mean density $< \rho >= 3M/4\pi R^3$. These are, however, dependent on the set $\{M, L, R\}$, and are sometimes used, when comparing data with models, in substitution of one or more of the latter, in order to have a parameter set that may be closer to the directly observed quantities. All of these parameters evolve with time t, and together they describe stellar evolution.

High-precision and accurate measurements of fundamental parameters for stars in all evolutionary stages across the HR diagram are needed in order to test the theory of stellar evolution, as well as the theory of stellar atmospheres and, consequently, improve our knowledge about stellar physics. One problem often faced is that not all of the fundamental stellar quantities can be obtained directly from observations. Instead, some must be inferred from measurements of other observational quantities. In addition, for some of the parameters, such as the radius and chemical composition, what is observed may not correspond to the desired quantity. Concerning the radius, since stars are gaseous spheres, they do not have a well-defined "edge". So, in practice, what is observed is the center-to-limb intensity variation across the stellar disk (and its circumstellar environment), which depends on the

star's atmospheric structure (see, e.g., Scholz 2003). Concerning the chemical composition it may vary both across the surface of the star and with depth.

There are several techniques used to obtain the fundamental properties of a star. In this chapter we will mainly focus on three of these techniques, namely on photometry, spectroscopy and interferometry.

2.1.1 Photometry

2.1.1.1 Brightness and magnitudes

Stellar photometry is a technique that consists in the study of the light emitted by a star or other astronomical object. In the particular case of stars, it deals with the accurate measurement of their brightness and with the changes in their brightness over time.

Several ways to determine the brightness of a star have been used over time. The earliest photometric studies were done by eye. The Greek astronomer Hipparchus of Nicaea, working in Rhodes (129 B.C), organized the first catalog of about ~1000 stars, with positions and brightnesses, using only his naked eyes. He classified the stars from first to sixth magnitude, the first magnitude being the brightest stars, while the sixth magnitude, the faintest ones. His work was further studied by other astronomers, in particular by Ptolemy of Alexandria who seems to have copied this magnitude system in his Almagest (170 A.C.). In 1856, Pogson proposed a magnitude scale that was not very different from the traditional one, but could be quantified more rigorously. This magnitude scale is based on two criterias, namely, that the ratio between the brightness of two stars differing by one magnitude is constant and that a first magnitude star is 100 times as bright as a typical sixth magnitude star. Based on these criteria, one can write the following relation

$$m_1 - m_2 = -2.5 \log_{10} \left(\frac{b_1}{b_2} \right), \tag{2.1.1}$$

where m_1, m_2 are the apparent magnitudes of two stars, and b_1, b_2 their respective brightnesses. An absolute scale can be defined as,

$$m = -2.5 \log_{10} b + C_1, \tag{2.1.2}$$

where C_1 is a constant computed from standard stars, to which apparent magnitudes were given by convention. This constant is known as the zero-point of the magnitude scale, and once established one can determine the magnitude of other stars. Note that the star's apparent magnitude refers to the amount of energy that reaches the detector being used during the star's observations.

This magnitude scale is still used today having been extended to objects fainter than sixth magnitude and brighter than first magnitude. Only stars up to the sixth magnitude can be observed with the bare eye, while objects with a much smaller intensity, that is a bigger magnitude, up to over 23, can be observed with a telescope. Accurate measurement of magnitudes was only made possible in the 20th century through the advent of photoelectric devices. Photoelectric devices, such as photomultiplier tubes, photodiodes and charge-coupled devices (CCDs), have replaced the photographic plate.

The apparent magnitude is related to the amount of energy coming from a star and the measure of that energy will depend on the system used to make the observations, i.e the telescope, the photometer or spectrograph, and the detector. Moreover, one may have to take into account the absorption of the light from a star due to the Earth's atmosphere and/or the interstellar medium. The brightness, b, of a star is then given by

$$b = \int_0^\infty f(\lambda)\tilde{R}(\lambda)\mathrm{d}\lambda \tag{2.1.3}$$

where $f(\lambda)$ is the star's energy flux per unit of wavelength (measured, e.g., in $\mathrm{Wm^{-2}\AA^{-1}}$), $\tilde{R}(\lambda)$ is the total system response function as a function of wavelength, which includes the instrument response and atmospheric extinction, the latter being applicable for ground-based observations. We note that the constant C_1 from Eq. (2.1.2) depends on $\tilde{R}(\lambda)$, which consequently, depends on the particular instrument that is being used to make the observations.

The apparent magnitude of a star depends on its intrinsic properties, such as its energy flux and radius, on the interstellar extinction, on the equipment used to make the observations, and on our distance to it. In order to compare the brightness between different stars, it is important to set a magnitude scale, independent of their distances d. The absolute magnitude, M, is defined as the apparent magnitude that the star would have if it was at a distance of 10 parsec. From Eq. (2.1.1), one gets

$$M = m + 5 - 5log_{10}d. \tag{2.1.4}$$

with d expressed in parsec.

The flux radiated by the star, F, and the flux that would be measured at Earth, if no absorption between the star and us existed, and all the energy reaching the detector were measured, f, are related by,

$$f_{\mathrm{bol}} = F\left(\frac{R}{d}\right)^2. \tag{2.1.5}$$

In the above, the total apparent flux, $f_{\rm bol}$, also called the bolometric flux, is given by

$$f_{\rm bol} = \int_0^\infty f(\lambda)\mathrm{d}\lambda. \tag{2.1.6}$$

Moreover, the absolute luminosity of a star, i.e. the total amount of energy radiated by it per unit time, is given by,

$$L = 4\pi R^2 F. \tag{2.1.7}$$

Assuming that stars radiate as black bodies, with temperature $T_{\rm eff}$, Eq. (2.1.7) becomes

$$L = 4\pi R^2 \sigma T_{\rm eff}^4. \tag{2.1.8}$$

The apparent bolometric magnitude, $m_{\rm bol}$, is defined as

$$m_{\rm bol} = -2.5 \log_{10} f_{\rm bol} + C_2 \tag{2.1.9}$$

where C_2 is determined taking into account a given value for the bolometric magnitude of the Sun, $m_{bol,\odot}$ (e.g., Torres 2010). The apparent bolometric magnitude is related to the absolute bolometric magnitude, M_{bol}, through

$$M_{\rm bol} = m_{\rm bol} + 5 - 5log_{10}d. \tag{2.1.10}$$

The latter being determined by the total luminosity L of the star.

Due to the atmospheric and instrumental absorption, we are not able to measure the total apparent flux of a star. The bolometric correction, BC, is a quantity to be added to the apparent magnitude in a specific passband (in the absence of interstellar extinction) in order to account for the flux outside that band:

$$m_{\rm bol} = m_V + BC_V, \tag{2.1.11}$$

where BC_V and m_V is the visual bolometric correction and the visual apparent magnitude, respectively. The visual band magnitude is often considered in this equation for historical reasons, however, the definition of bolometric correction can be generalized to any passband. The bolometric correction depends on the filter response function $\tilde{R}(\lambda)$ and on the distribution of the star's flux with wavelength, i.e. on the stellar spectral type.

2.1.1.2 Photometric systems

A photometric system is a set of system responses at specific passbands (filters), with a definition of the zero-point for each passband. They can be categorized according to the

widths of their passbands: broad-band systems with bands, $\Delta\lambda$ at least 300 Å wide and up to about 1000 Å wide, intermediate-band systems with bands 70 Å $\lesssim \Delta\lambda \lesssim$ 300 Å, and narrow-band systems with bands no wider than a few tens of Å ($\Delta\lambda \lesssim 70$ Å).

Photometric colours, also known as colour indices, are defined as the differences between magnitudes of a given star in two different passbands. Photometric systems that provide multi-band photometry often give a single magnitude and several colour indices for a given star. By observing a star through different-coloured filters one may have some indication of its flux distribution, and hence, its spectral type.

The photometric systems can be classified according to the choice of the standard stars that define the zero-points, as derived from Eq. (2.1.2). For instance, the Vega systems (also known as "vegamag" systems) are the ones for which the zero-points are set by using the magnitude and colours of the Northern A0V star Vega or of a set of A0 stars. In this system, the colours of Vega are set to zero, and its V magnitude in the Johnson system is 0.03 (Johnson & Morgan 1953). Some systems, however, define the V magnitude of Vega to be 0 rather than 0.03 (e.g. Gray 2007).

In the Gunn griz systems, the metal poor main-sequence F-type subdwarfs are used as a reference, instead of Vega. In particular, the star BD +17 4708, for which all colours are defined to be zero is considered, with all magnitudes equal to 9.50. The AB (Oke 1965) and STMAG (Koornneef et al. 1986) systems define the colours of a source of constant frequency flux density, or wavelength flux density, respectively, to be zero. Zero magnitude in these systems correspond to the flux of Vega at $\lambda \sim 5500$ Å (Johnson's V band).

In what follows I will briefly mention some common photometric systems in the optical and infrared (IR). A detailed description of the most common photometric systems and their respective references can be obtained in the review on standard photometric systems of Bessell (2005). Some examples of these systems are the Johnson & Morgan UBV (Johnson & Morgan 1953) system and its extensions to longer wavelengths, in the near-infrared bands ($R, I, Z, J, H, K, L, M, N, Q$). The Johnson system is a Vega system. Also the Hipparcos/Tycho photometric system is a Vega system. It provides visible photometry in three bands, namely in H_P, B_T and V_T, that was obtained with the use of the Hipparcos satellite. The Geneva system (Rufener & Nicolet 1988) is a seven colour-photometric system (with $U, B, V, B1, B2, V1, G$ bands) and is also a Vega system. The strömgren *uvby* (Strömgren 1966) is a widely used intermediate-band photometric system and is intended for determining temperatures and gravities of B, A, F and early-G stars and metallicities of F and G stars. It is a Vega system. The 2MASS JHK_s system (Cohen et al. 2003) provides data in the J, H, and K_s bands. These bands are similar to the Johnson's J, H, K bands, with

the major difference being the K_s band. The 2MASS magnitudes are normalized to a Vega system, but with the magnitude of Vega being zero rather than 0.03 (see, e.g., Cohen et al. 2003). In addition to these, there is the Sloan Digital Sky Survey $u'g'r'i'z'$ system (Smith et al. 2002) which is a Gunn system. The bands span a full range of wavelengths from 3000 to 10000 Å. The Kepler Spectral Classification Program team used a set of Sloan-like filters to observe stars within the Kepler input catalogue and provide sloan magnitudes for them.

Around 1900 the photometers started to appear in association with the spectrographs, making the spectrophotometers. The term spectrophotometry is used when not only the amount of radiation but also its spectral distribution are measured.

2.1.2 Spectroscopy

Stellar spectroscopy is a technique that consists in the study of the spectrum of a star. A stellar spectrum is obtained when the light of a star is dispersed according to its wavelength in a spectrograph. While photometric measurements of the luminosity of a star are given through coloured filters (and provide rough estimations of the energy distribution per wavelength), a stellar spectrum provides a more detailed information about that distribution. One can thus think of photometry as a form of a low resolution spectroscopy.

The spectral resolution, $\mathcal{R}$, of a spectrograph defines the ability that it has to resolve features in the electromagnetic spectrum and is given by,

$$\mathcal{R} = \frac{\lambda}{\Delta\lambda}, \tag{2.1.12}$$

where $\Delta\lambda$ is the smallest difference in wavelengths that can be distinguished at a wavelength of λ. The exact resolution ranges of a low, medium or high resolution spectrograph are not well established. However, one may vaguely consider that $\mathcal{R} < 20000$, $20000 < \mathcal{R} < 50000$, and $\mathcal{R} > 50000$ as being a low, medium, and high resolution spectrograph, respectively.

In 1666, Sir Isaac Newton observed the spectrum of the Sun. He found that when the white light of the Sun passed through a glass prism, the light was split into a rainbow. In the 19th century, several scientists studied the spectrum of light, namely the sunlight. In 1814, the German optician Joseph Fraunhofer rediscovered the dark lines of the Sun's spectrum. He catalogued 576 thin black lines that he observed in the Sun's spectrum and, in 1821, he was able to associate one of the dark lines with an "earth element". At this time it was already verified that the same dark line appears when salt is sprinkled in a flame. He was then able to measure the wavelengths of the two sodium lines, obtaining values very close to the modern ones. However, he could not explain why the dark lines where there. In 1859, Gustav

Kirchhoff and Robert Bunsen working with laboratory chemical spectra found that each chemical element has its own unique spectral signature - called spectral lines. Moreover, in that year Kirchhoff summarized the observed relationships among the three types of spectra (continuous, emission line, and absorption line), known as Kirchhoff's Laws.

With spectroscopy we are able not only to detect the presence of chemical elements in stellar atmospheres, but also to quantify their abundance. However, for the latter we depend on the use of theoretical models of stellar atmospheres, as these are needed to compute synthetic spectra to compare to the observed one. Through such comparison we are generally able to derive important stellar parameters, such as the effective temperature, surface gravity and, as discussed, the star's chemical composition (see, e.g., Gray 2005).

Additional information that may be obtained through the analysis of the spectrum of a star are stellar rotation, oscillations, activity, binarity, magnetic fields' properties (in particular if spectropolarimetry is considered), etc.

In the work described in this Chapter, the stellar spectra that we used was aimed at determining the total observed flux of a pulsating star. This was done in combination with other sources of flux information, such as spectrophotometry, as well as atmospheric models for the same star. We considered, for the stars under study, observed low resolution spectra calibrated in flux available in the literature.

When the light of a star enters the telescope and passes through a spectrograph, a detector captures the resulting spectrum on, for instance, a CCD. Then the 2-D raw spectrum, as intensity vs wavelength, which might be in counts per second (or similar) must be calibrated in flux so that the spectral energy distribution above the atmosphere (the physical flux) of the observed star can be obtained. The standard procedure of flux calibration (e.g., Bessell 1999) consists in the determination of the instrumental response (i.e. the effect of the whole telescope's optics in combination with the CCD spectral sensitivity) and in the correction for the atmospheric absorption (i.e. the absorption by a clear atmosphere plus the extinction due to atmospheric haze) by comparing the observed stellar spectra to templates of stars with known spectral energy distribution, denominated as standard stars. These standards must be observed with the same setup and during the observations of the target stars. The flux calibration procedure may be problematic due to several reasons: (1) there are few suitable accurate spectrophotometric standards (they should be hot stars, with few absorption lines, and for which one may approximate its spectral distribution by a black body), (2) there is some difficulty of removing the telluric lines from the observed spectra (i.e. absorption lines that originate in the Earth's atmosphere and are prevalent in the visible and in the IR regions of the spectrum), (3) standard stars should be observed by the telescope in use.

For the work presented in this Chapter we found in the literature only few, and sometimes old, low resolution spectra calibrated in flux for the stars under study. The precision of the available spectra is no better than 1.5 - 2%.

2.1.3 Interferometry

Interferometry consists in using several techniques to analyse the result of interference of waves. The interference patterns of waves are created by optical systems, the interferometers.

Interferometers were idealized and constructed in the 19th century, having an important role in the scientific and technological development during the end of the 19th century and during the entire 20th century. A historical review of stellar interferometry is given by Lawson (2000).

In this thesis, we will focus on the importance of stellar interferometry for the determination of accurate stellar angular diameters. It was in 1920, that the first determination of an angular diameter of a star other than the Sun was made using one of the first interferometers built for astronomical proposes, on the Mount Wilson Observatory's reflector telescope. The star in question named Betelgeuse, also known as alpha Orionis, is a red giant star, (Michelson & Pease 1921). At that time, the error induced by atmospheric fluctuations on the measured angular diameter was estimated in the order of 10% to 20%. The first angular diameter determination of a main-sequence star was done by Hanbury Brown & Twiss (1956), on α CMa (Sirius), using the Narrabari Stellar Intensity Interferometer at the Narrabari Observatory (Hanbury Brown et al. 1967). Further advances in interferometry would require the interferometric combination of light from separate telescopes spaced by many tens of meters. This would provide more precise measurements of the angular size than previously obtained. Measurements using separated telescopes were made by Johnson et al. (1974) in the infrared and by Labeyrie (1975) in the optical. The major difficulty for the optical interferometry from the ground is caused by the atmospheric turbulence. In the late 1970's, thanks to the improvements in computer processing, the first fringe-tracking interferometer could operate fast enough to follow the blurring effects of astronomical seeing. The Massachusets Institute of technology and the Naval Research Laboratory built and operated a series of prototype interferometers named Mark I, Mark II, and Mark III. Shao & Staelin (1980) reported the first successful active fringe-tracking results. In the last few years, interferometry in the near infrared and in the visible is undergoing a fast evolution, thanks to the development of precision opto-mechanical engineering, real-time control, and detectors.

That can be seen from a new generation of fully operable interferometers, such as CHARA[11] (at Mount Wilson), VLTI[12] (at ESO-Paranal), and Keck[13] (at Mauna Kea). Recent reviews of the topics of interferometric techniques, including their application to fundamental stellar parameters are Quirrenbach (2001), Bergeron & Monnet (2002), Monnier (2003), Haniff (2007a,b), Cunha et al. (2007).

The basic principle of stellar interferometry consists on observing a stellar source using two or more separate telescopes, then a complex system of mirrors guides the beams from the different telescopes to a delay line system, to compensate the path differences, and subsequently to the beam combiner where light-waves are superimposed to produce bright and dark fringes. The contrast or 'visibility' of these fringes is a measure of the coherence of the light beams received from the different telescopes. If the separation between the telescopes (baseline) is made very small then the coherence has the value unity, i.e. the light beams are identical and the visibility of the fringes is high. As the separation between telescopes increase, the coherence and hence the visibility of fringes decrease until they disappear. The exact relationship between fringe visibility and telescope separation depends on the wavelength of the light received from the source, the size of the source, and the distribution of light across the diameter of the source.

In practice, by measuring the visibility with a range of baselines of different lengths, one is able to determine the angular diameter of a star, by fitting the measured visibilities to the visibility curves of an uniform disk models of angular diameter $\theta_{\rm UD}$ by χ^2 minimization. This comparison assumes a star to be an uniform disk and thus neglects the effect of limb-darkening. A correction factor can be computed from a grid of stellar atmospheres, and applied to $\theta_{\rm UD}$ to calculate the limb-darkened diameter $\theta_{\rm LD}$.

The angular resolution, R of an interferometer is equivalent to that of a telescope of diameter equal to the largest separation between its individual elements, i. e. $\mathsf{R} = \lambda/\mathsf{B}$, with B being the baseline.

With the interferometers available nowadays (see, e.g., Cunha et al. 2007, and references therein), stellar angular diameter estimates (and hence stellar radius estimates, if the parallax is known) with a relative precision better than a few per cent can be obtained. For instance, Boyajian et al. (2012) recently measured the angular diameter of 44 main-sequence A, F, and G type stars with an average precision of 1.5%.

This direct method of obtaining stellar radius with high precision is of great importance.

[11] http://www.chara.gsu.edu/CHARA/

[12] http://www.eso.org/sci/facilities/paranal/telescopes/vlti/

[13] http://keck.jpl.nasa.gov/keck_index.cfm

The radius is one of the fundamental parameters of a star. Once having a precise determination of the stellar radius, one can use it to restrict the space of parameters in stellar models and have a very good estimation for the stellar mass. Moreover, when combining the interferometric stellar radius with asteroseismic data, one may be able to increase the precision of the determination of stellar mass and age (Creevey et al. 2007). As an example, in a study performed on the solar twin 18 Sco by Bazot et al. (2011), the author employed asteroseismology (12 nights with HARPS) and long-baseline interferometry (with the PAVO beam-combiner at the CHARA array) in order to derive the star's radius and mass. They were able to obtain these two parameters with precisions of $\sim 1\%$ and $\sim 3\%$, respectively.

Additionally, combining the interferometric derived stellar radius with an estimate for the bolometric flux, one can obtain a direct measurement of a star's effective temperature (e.g., Boyajian et al. 2012).

2.2 Fundamental parameters of rapidly oscillating Ap stars

In order to place a star in the HR diagram and hence find the model that best represents it, the star's luminosity and effective temperature need to be determined as accurately as possible. The former can be computed if the distance, d, ($d = 1/\Pi$ in parsec (pc) units, Π the parallax in arcseconds (as)) and the apparent bolometric flux, $f_{\rm bol}$, are known; while the latter can be derived if the angular diameter θ and $f_{\rm bol}$ are known, i. e.,

$$L = \frac{4\pi f_{\rm bol} C^2}{\Pi^2} \tag{2.2.1}$$

and

$$\sigma T_{\rm eff}^4 = \frac{4 f_{\rm bol}}{\theta^2}, \tag{2.2.2}$$

where C is the conversion factor from parsecs to metres. The bolometric magnitude (or flux) can be determined from the visual magnitude (or flux) if the visual bolometric correction is available (cf. Eq. (2.1.11)). Numerous tabulations can be found in the literature for the empirical visual bolometric corrections. However, they are determined from the analysis of normal stars and they should not be used for roAp stars. RoAp stars show abnormal flux distributions, with strong flux deficiencies in the ultraviolet relative to normal stars with the same Paschen slope (Leckrone 1973; Leckrone et al. 1974; Jamar 1978). This makes the visual bolometric corrections available for normal stars rather unreliable for roAp stars. In what follows, we will describe the method that we used to determine the bolometric flux for this type of stars. We will also present our results, i.e the bolometric flux values that we obtained using the described method applied to two roAp stars, namely β CrB (Bruntt

et al. 2010) and γ Equulei (Perraut et al. 2011). The computed bolometric flux values were combined with the stars' distance and angular diameter obtained from interferometry, which together made possible a relatively accurate determination of their effective temperature and luminosity.

2.2.1 Bolometric flux of rapidly oscillating Ap stars

The bolometric flux is given by the area under the curve that represents the spectral energy distribution (SED) of a star, in all wavelengths from zero to infinity. As an example of a synthetic SED of a star with effective temperature of 5770 K, $\log g = 4.4$ and solar metallicity, i.e. [Fe/H] = 0, is shown in Figure 2.1. The task of determining the bolometric

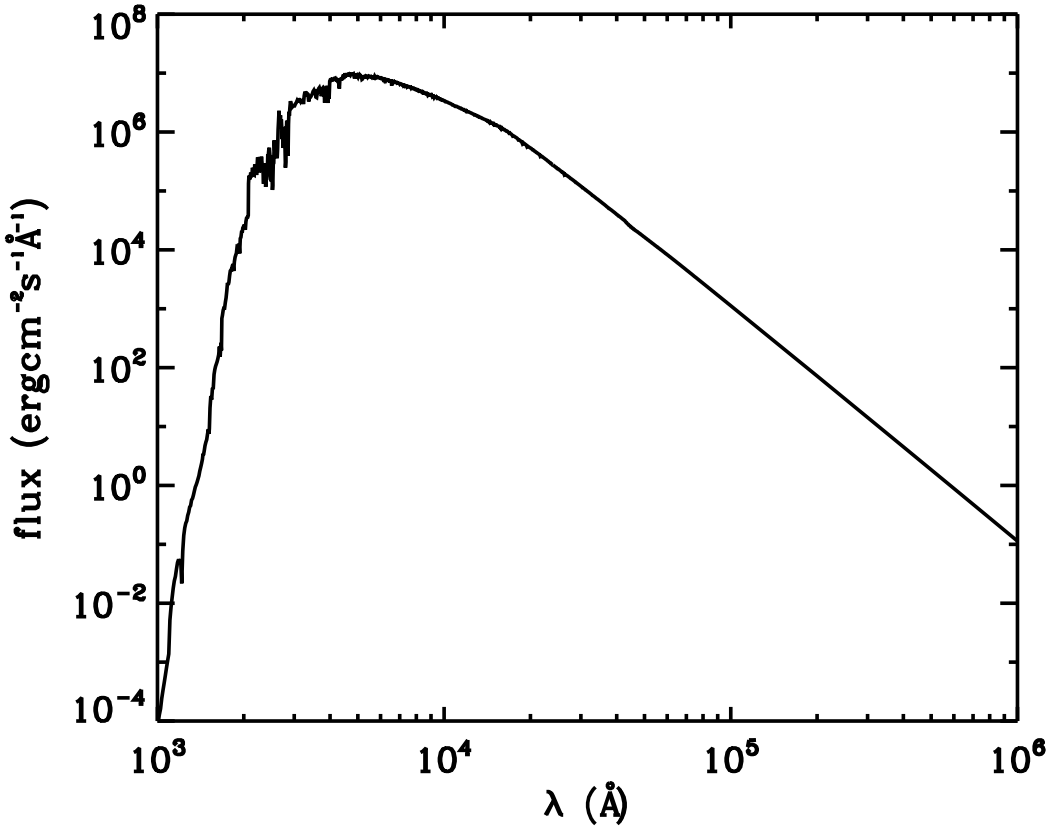

Figure 2.1: A synthetic spectral energy distribution (SED) of a star with effective temperature of 5770 K, $\log g = 4.4$ and solar metallicity, from the Kurucz Atlas9 database. The flux is given in FLAM surface flux units, i.e. erg cm^{-2} s^{-1} Å^{-1}.

flux would be easy to perform if that energy distribution was available. However, the

spectral energy distributions available in the literature are given in bands of wavelengths which, in most cases, all together do not cover the entire wavelength range. Hence, regions of wavelength for which no SED is available have to be filled either through recourse to synthetic spectrum or by interpolation and/or extrapolation from the wavelengths for which the SED is available.

To compute the bolometric flux of roAp stars, we started by searching in the literature for low resolution flux calibrated spectra of the targets under study. In addition, we looked for photometric data to complement the spectral coverage. In the wavelength range for which only photometric data or no data at all were available, we either used model atmospheres (in our case Kurucz models) or performed linear interpolations. Regarding the Kurucz models, they were obtained using the IDL routine Kurget1 (Atlas9 models) and the corresponding database of models available in the IUE reduction and data analysis package IUEDAC[14]. We looked for the Kurucz model (in terms of $T_{\rm eff}$, log g and [Fe/H]) that best represented the photometric data and/or the low resolution spectra available for the star. The whole energy distribution of the star was finally obtained by combining the star's low resolution spectra in a certain wavelength range with the synthetic spectrum of the best fitted Kurucz model, and/or linear interpolations performed in the wavelength range for which no observed spectra was available.

2.2.2 β CrB

The northern bright star β Coronae Borealis (β CrB, HD 137909, HR 5747, HIP 75695), which belongs to the Corona Borealis constellation has been extensively studied in the past. It is a multiple system with two confirmed components (Tokovinin 1984). We refer to the primary star, β CrB A and to the secondary β CrB B.

β CrB first *Hipparcos* parallax determination was $\Pi = 28.6 \pm 0.69$ mas. The new reduction by van Leeuwen (2007) gives $\Pi = 29.17 \pm 0.76$ mas. However, the latter is not corrected for binarity effects, so, here, we adopted the original *Hipparcos* parallax.

β CrB, in particular β CrB A, is part of the coolest subgroup of the classical Ap stars, the SrCrEu, having been classified as a type A9 SrEuCr by Renson & Manfroid (2009). β CrB A was found to pulsate in a single oscillation frequency at 1.031 mHz (a period of 16.2 min) (Kurtz et al. 2007), becoming a member of the roAp class of pulsators.

Several values for the effective temperature of β CrB can be found in the literature, of

[14] http://archive.stsci.edu/iue/iuedac.html

Table 2.1: Limb-darkened angular diameters, $\theta_{\rm LD}$, and NACO J and K magnitudes for β CrB from Bruntt et al. (2010).

Star	$\theta_{\rm LD}$ (mas)	NACO magnitudes	
		J	K
β CrB A	0.699 ± 0.017	3.54 ± 0.07	3.50 ± 0.08
β CrB B	0.415 ± 0.017	5.00 ± 0.07	4.86 ± 0.08

which we mention here a few. Kochukhov & Bagnulo (2006) used photometric indices to determine the effective temperature and found 7430 ± 200 K. Netopil et al. (2008) have determined the effective temperature of β CrB from three photometric systems (Strömgren, Geneva and Johnson) and compared these with values in the literature. The mean value derived from the photometric indices is 7710 ± 260 K and the mean of the literature values is 8340 ± 360 K. This is a typical example of the large scatter found in effective temperature determinations of chemically peculiar A stars.

Interferometric observations of β CrB in the near infrared were obtained by Bruntt et al. (2010) using the CHARA array and the FLUOR[15] instrument. Limb-darkened angular diameters derived by the authors for β CrB A and β CrB B are shown in Table 2.1. Bruntt et al. (2010) also observed β CrB using the VLT/NACO[16] adaptative optics instrument and obtained images for the two components of the binary system in the J and K bands, which led them to the determination of the NACO J and K magnitudes for each of the components separately. These values are given in Table 2.1. Moreover, the authors found a maximum angular separation of 0.3″ between the two components.

In order to accurately determine the effective temperature of β CrB we made use of the interferometric and the imaging data mentioned above. In what follows we will describe our method to compute the bolometric flux which, together with the angular diameter, made possible a weakly model dependent determination of the effective temperature of β CrB (cf. Eq. (2.2.2)). The luminosity was also determined by combining the computed bolometric flux and the *Hipparcos* parallax extracted from the literature (cf. Eq. (2.2.1)).

2.2.2.1 Data

For the ultraviolet (UV) range we downloaded ten spectra of β CrB (Table 2.2) from the Sky Survey Telescope (Jamar et al. 1976) obtained at the *IUE* " Newly Extracted Spectra" data

[15] http://www.lesia.obspm.fr/astro/interfero/pages/fluor_english.html
[16] http://www.eso.org/sci/facilities/paranal/instruments/naco/

Table 2.2: UV spectra from IUE for β CrB. LWR and SWP stands for Long Short Redundant and Short Wavelength Prime, respectively. High@low stands for high dispersion rebinned to low dispersion.

Image Number	Camera	Dispersio	Aperture	Observation Start Time (UT)	Exposure Time (s)
02369	LWR	High@low	small	16/09/78 06:13:00	899.765
02382	LWR	High@low	small	17/09/78 04:36:13	419.714
03999	LWR	High@low	small	12/03/79 17:05:00	383.669
04000	LWR	High@low	small	12/03/79 18:51:00	359.503
07000	LWR	High@low	large	24/02/80 13:38:47	269.800
02661	SWP	High@low	large	16/09/78 06:47:00	2999.781
02667	SWP	High@low	small	17/09/78 04:47:24	1799.652
04606	SWP	High@low	small	12/03/79 16:27:00	1209.828
04607	SWP	High@low	small	12/03/79 17:33:00	4199.499
08038	SWP	High@low	large	24/02/80 13:08:31	1079.576

archive[17]. We used only rebbined high resolution ($\mathcal{R} = 18000$ at $\lambda = 1400$ Å, $\mathcal{R} = 13000$ at $\lambda = 2600$ Å) spectra (Solano 1998) from the long (1850 - 3350 Å) and short wavelength (1150 - 1980 Å) ranges obtained with small (3″ circle) and large aperture (20″×10″). Based on the quality flag listed in the IUE spectra (Garhart et al. 1997) we removed all the bad pixels from the data, i.e. we considered only the points with quality = 0. The mean of the spectra for each wavelength range (long vs short) was then computed to obtain one single spectrum of β CrB between 1150 and 3350 Å.

For the visible part of the spectrum, we considered a low resolution spectrum calibrated in flux in the interval $3200\,\text{Å} < \lambda < 10800\,\text{Å}$ obtained by Alekseeva et al. (1996). We also considered the V band magnitudes for each component. They were computed from the total magnitude of the system, $m_V(A+B) = 3.67$ (Rufener & Nicolet 1988) and the magnitude difference $\Delta m = 1.99$ measured by Horch et al. (2004) by speckle interferometry at 503 nm. This combination gives $m_V = 3.83$ and $m_V = 5.82$, for the components A and B, respectively. To convert these visual magnitudes into flux we used an equation equivalent to Eq. (2.1.2) in terms of the stellar flux where the value for the constant C_1 is shown in Table 2.3 given by Rufener & Nicolet (1988). These values were then used to calibrate the Kurucz models, as explained below. This calibration is needed since Kurucz models give the flux at the surface of the star, not the value observed on Earth.

For the near IR we considered the NACO J and K magnitudes mentioned in Section 2.2.2.

[17] http://sdc.laeff.inta.es/cgi-ines/IUEdbsMY

Table 2.3: Calibrated photometric m_V, and NACO J and K fluxes for β CrB.

Band	$\lambda_{\rm eff}$ (Å)	Flux ($\times 10^{-12}$ erg cm^{-2} s^{-1} Å^{-1})		C_1
		β CrB A	β CrB B	
V	5504	109.749	17.550	3.5690
J	12650	11.347	1.795	23.8228
K	21800	2.957	0.513	25.8647

Again, to convert these magnitudes into fluxes we used Eq. (2.1.2) in terms of the stellar flux. The constant C_1 was computed by integrating the flux of Vega through each of the J and K filters of the NACO instrument and assuming that Vega has zero magnitude in all bands. These results are shown in Table 2.3.

2.2.2.2 Bolometric flux and Effective temperature

The bolometric flux of β CrB was determined by combining the data collected from the ultraviolet (UV) to the near infrared (near IR), as described in Section 2.2.2.1, with the synthetic spectrum based on the Kurucz models, in the wavelength ranges where the data is not available or not sufficient to compute the bolometric flux.

Since β CrB is a binary system with an angular separation of ~0.3", the data from the INES data archive and the data from the catalog of Alekseeva et al. (1996) contain the flux of both components. Since our interest was primarily β CrB A, we had to subtract the spectral contribution of β CrB B to the spectrum of the binary. As no observed spectrum of β CrB B is available in the literature to compute the SED of β CrB B, we used the Kurucz models that best fitted the only photometric data available for this star, which are its m_V, and the NACO J and K magnitudes. We constructed a grid of Kurucz models for β CrB B based on its effective temperature, derived from the combination of the interferometric measurement of the angular diameter and a published bolometric correction for the star (Bessell et al. 1998). Note that β CrB B is a 'normal' star, thus the bolometric correction used should be reliable. The synthetic spectra for the Kurucz models were calibrated using the m_V magnitude of β CrB B. In order to take into account the errors in the J and K magnitudes, we generated 100 random J and K magnitudes within the uncertainties and found the 100 Kurucz models spectra that best fitted the generated set of magnitudes. We subtracted each of the 100 spectra of the component B from the UV and visible spectrum of the binary, thus obtaining 100 spectra in the UV and visible for the component A. We then performed a mean over these 100 spectra to obtain one single spectrum of β CrB A in the UV and visible. To determine the spectrum of β CrB A in the infrared we considered two cases. (1) We used

the synthetic spectrum for the Kurucz model that best fitted the spectrum of the star in the visible and the NACO J and K photometry. To calibrate the models we considered the flux of the spectrum of β CrB A at $\lambda = 5504$ Å to be the same as that of the Kurucz model spectrum at this wavelength. (2) we used the synthetic spectrum for the Kurucz model that best fitted the m_V, and the NACO J and K photometry. In this case, m_V of β CrB A at $\lambda = 5504$ Å was used to calibrate the models. In both cases (1) and (2) we generated 100 J and K magnitudes of β CrB A within the uncertainties, and in case (2) we also generated 100 m_V values. We got 100 Kurucz models that best fitted each set of generated magnitudes. We then performed a mean over the 100 best Kurucz models found for each case. Note that when searching for the best Kurucz model we intentionally disregarded the data in the UV, because Kurucz models are particularly unsuitable for modelling that region of the spectra of roAp stars.

The final spectrum of β CrB A, shown in Figure 2.2, was obtained from an extrapolation to the interval 912 Å $< \lambda <$ 1150 Å assuming zero flux at 912 Å, the averaged IUE spectrum in the wavelength interval 1150 Å $< \lambda <$ 3350 Å, and the Alekseeva et al. (1996) spectrum from 3200 to 10800 Å, both without the contribution of β CrB B, and for wavelengths longer than 10800 Å we considered the two averaged best Kurucz models found, as previously described.

In short, the bolometric flux for component A, $f_{\rm bol,A}$, can be written as,

$$f_{\rm bol,A} = \frac{\sum_{k=1}^{N}\left[\left(f_{\rm IUE,bin.} + f_{\rm spectrumV,bin.}\right) - f^{k}_{\rm IUE+spectrumV,B}\right]}{N} + \begin{cases} \frac{\sum_{k=1}^{N} f^{k}_{\rm IR1,A}}{N} \\ \frac{\sum_{k=1}^{N} f^{k}_{\rm IR2,A}}{N} \end{cases} , \qquad (2.2.3)$$

where $N = 100$. $f_{\rm IUE,bin.}$ is the combined flux of the binary in the UV obtained from the IUE spectrum from 1150 Å to 3350 Å, $f_{\rm spectrumV,bin}$ is the flux of the binary in the visible from 3200 Å to 10800 Å (Alekseeva et al. 1996), $f^{k}_{\rm IUE+spectrumV,B}$ is the flux of the component B from 1150 Å to 10800 Å for each k Kurucz best model, and $f^{k}_{\rm IR1,A}$, $f^{k}_{\rm IR2,A}$ are the fluxes of each k Kurucz best model found for the component A in the wavelength region $\lambda >$ 10800 Å in cases (1) and (2), respectively. The error on the bolometric flux for component A, $\Delta f_{\rm bol,A}$, can be written as,

$$\Delta f_{\rm bol,A} = \sqrt{(\Delta f_{\rm IUE,bin.})^2 + (\Delta f_{\rm spectrumV,bin.})^2 + (\Delta f_{\rm IUE+spectrumV,B})^2 + \begin{cases} (\Delta f_{\rm IR1,A})^2 \\ (\Delta f_{\rm IR2,A})^2 \end{cases}} , \qquad (2.2.4)$$

where $\Delta(...)$ stands for the uncertainties on the fluxes. We considered relative flux uncertainties of 10% for $f_{\rm IUE,bin.}$ (González-Riestra et al. 2001), and 3% for $f_{\rm spectrumV,bin.}$ (Alekseeva et al. 1996). The uncertainties on $f_{\rm IUE+spectrumV,B}$, on $f_{\rm IR1,A}$, and on $f_{\rm IR2,A}$ are taken to be

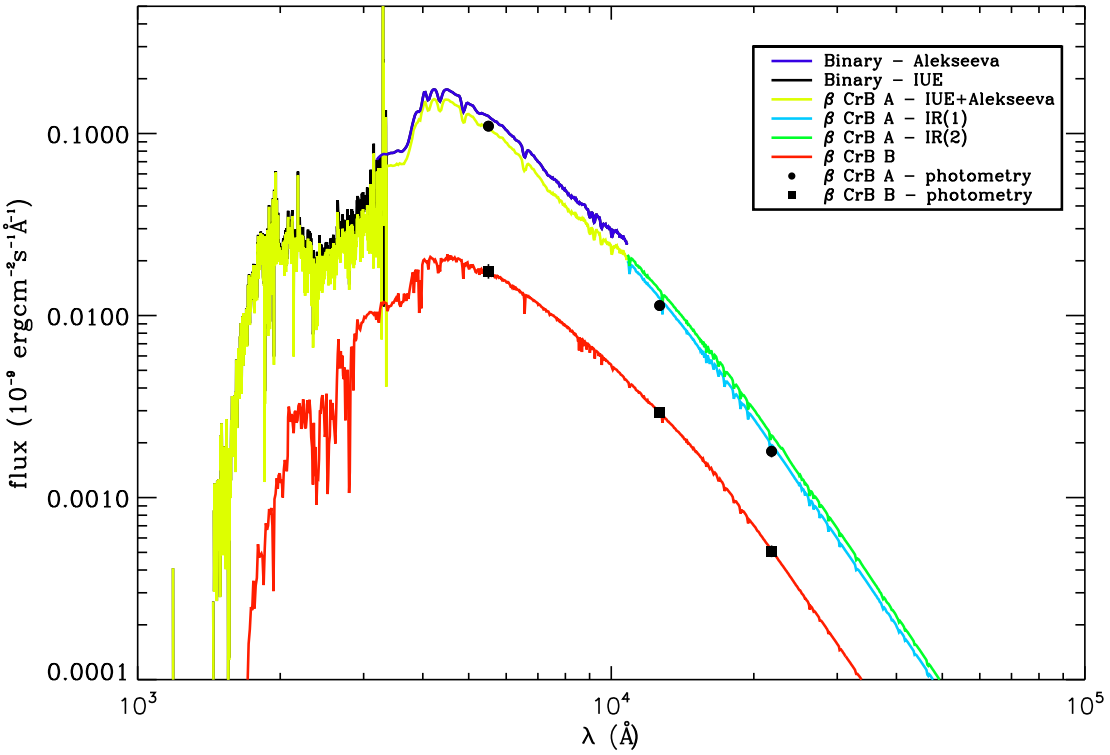

Figure 2.2: The black line shows the combined IUE spectrum from 1150 Å to 3350 Å and the dark blue line shows the low resolution spectrum calibrated in flux, in the visible, from 3200 Å to 10800 Å (Alekseeva et al. 1996), for the β CrB binary. The yellow line shows the spectrum of β CrB A from 1150 Å to 10800 Å obtained after removing the contribution of β CrB B (red line) to the spectrum of the binary in that wavelength range. The green and light blue lines for $\lambda > 10800$ Å correspond to the averaged Kurucz model spectra that best fits the spectrum of β CrB A from 3200 Å to 10800 Å and its NACO J and K magnitudes (green line) and the averaged Kurucz model spectra calibrated to m_V that best fits β CrB NACO's J and K magnitudes (light blue line). The m_V, J, and K magnitudes are shown for β CrB A and β CrB B as circles and squares, respectively. Their errors are of the size of the symbols (see text for details).

the dispersion of the 100 best Kurucz models. Note that in case (1) no uncertainty was associated with the visible spectrum, when the simulations were made.

The bolometric flux of β CrB A, $f_{\rm bol,A}$, was then computed from the integral of the final spectrum. Moreover, the luminosity L and the effective temperature $T_{\rm eff}$ were computed through Eq. (2.2.1) and Eq. (2.2.2), respectively.

2.2.2.3 Results

Our results for the bolometric flux, effective temperature and luminosity for β CrB A and for β CrB B are shown in Table 2.4. The bolometric flux for component B, $f_{\rm bol,B}$, was determined

Table 2.4: Bolometric flux, $f_{\rm bol}$ (col. 2), effective temperature, $T_{\rm eff}$ (col. 3) and luminosity, L (col. 3) in solar units, obtained for β CrB A and for β CrB B (see text for details).

	$f_{\rm bol}$ (erg cm^{-2} s^{-1})	$T_{\rm eff}$ (K)	$L/{\rm L}_\odot$
β CrB A case (1)	$(6.4 \pm 0.2)\times10^{-7}$	7923 ± 114	24.4 ± 1.4
β CrB A case (2)	$(6.3 \pm 0.2)\times10^{-7}$	7890 ± 114	24.0 ± 1.4
β CrB B	$(1.23 \pm 0.02)\times10^{-7}$	6804 ± 142	4.7 ± 0.2

from the average of the bolometric flux values obtained from the 100 Kurucz models that best fitted its m_V, J and K magnitudes. We found $f_{\rm bol,B} = 1.23 \times 10^{-7}$ erg cm^{-2} s^{-1}. The dispersion on $f_{\rm bol,B}$ was found to be 0.02×10^{-7} erg cm^{-2} s^{-1}, corresponding to an uncertainty of 2%.

The bolometric flux for component A, $f_{\rm bol,A}$ was found to be $(6.4\pm0.2)\times10^{-7}$ erg cm^{-2} s^{-1} for case (1) and $(6.3 \pm 0.2) \times 10^{-7}$ erg cm^{-2} s^{-1} for case (2). The errors on $f_{\rm bol,A}$ were computed using Eq. (2.2.4) from which we obtain,

$$\begin{aligned}\Delta f_{\rm bol,A} &= \sqrt{(0.05\times10^{-7})^2 + (0.18\times10^{-7})^2 + (0.02\times10^{-7})^2 + \begin{cases}(0.01\times10^{-7})^2\\(0.06\times10^{-7})^2\end{cases}} \\ &= \begin{cases}0.2\times10^{-7}\\0.2\times10^{-7}\end{cases}\quad .\end{aligned} \tag{2.2.5}$$

As a final result for the flux, for the effective temperature and luminosity for β CrB A, we took the mean of each of the two values shown in Table 2.4 and considered the uncertainty to be the largest of each of the two uncertainties. The equation of propagation of errors was used to estimate the errors on $T_{\rm eff}$ and $L/{\rm L}_\odot$. The values derived for these quantities are

Table 2.5: Final results for β CrB A.

	$f_{\rm bol}$ (erg cm^{-2} s^{-1})	$T_{\rm eff}$ (K)	$L/{\rm L}_\odot$	$R/{\rm R}_\odot$
β CrB A	$(6.4 \pm 0.2) \times 10^{-7}$	7906 ± 114	24.2 ± 1.4	2.63 ± 0.09

given in Table 2.5. If, instead, we took for $T_{\rm eff}$ and L an uncertainty such as to enclose the two uncertainties, the result would be $T_{\rm eff,A} = 7906 \pm 130$K and $L/{\rm L}_{\odot,{\rm A}} = 24.2 \pm 1.6$.

The radius, R, was derived from the relation,

$$R = \frac{\theta}{2} \times d, \tag{2.2.6}$$

and its uncertainty, ΔR, from the equation of propagation of errors. We found $R_{\rm A} = 2.63 \pm 0.09\,{\rm R}_\odot$ for β CrB A, and $R_{\rm B} = 1.56 \pm 0.07\,{\rm R}_\odot$ for β CrB B.

Figure 2.3 shows the position of β CrB A in the HR diagram using the results shown in Table 2.5.

2.2.3 γ Equulei

γ Equulei (γ Equ, HD 201601, HR 8097, HIP 104858) belongs to the Equuleus constellation situated in the northern hemisphere. It has an apparent V band magnitude, m_V, of 4.7 being the third brightest star in its constellation and the second brightest roAp star known. Its classification as an roAp star results from it being a magnetic pulsating A9p SrEuCr star (Abt 1985). Detailed analysis of its light variation from multi-site observations performed by Martinez et al. (1996) shows that the star pulsates with four p-mode pulsation frequencies, corresponding to periods in the range from 11.68 to 12.45 min. Gruberbauer et al. (2008), using MOST photometry, discovered three additional pulsation frequencies in γ Equ, and confirmed the four previously known. Using a grid of magnetic models the authors were able to perform mode identifications for the seven observed frequencies. Their best model gives $M = 1.8\,{\rm M}_\odot$, $T_{\rm eff} = 7617\,{\rm K}$, $L/{\rm L}_\odot = 12.22$ and a polar magnetic field strength of about 8.1 kG. Ryabchikova et al. (2002) using a synthetic spectra with parameters $T_{\rm eff} = 7700\,{\rm K}$, $\log g = 4.2$, and the metals to hydrogen abundance ratio, [M/H] = +0.5, found an evidence for abundance stratification in the atmosphere of γ Equ, typical of roAp stars.

γ Equ is a multiple system (Mason et al. 2001). The primary component, hereafter, γ Equ A, is the peculiar one. Its closest component lies at $1.25'' \pm 0.04''$ and has a Tycho V magnitude difference, with respect to the primary star, of $\Delta m_{\rm VT} = 4$ (Fabricius et al. 2002). We will refer to the secondary star in the system as γ Equ B. The *Hipparcos* parallax of γ Equ is 27.55 ± 0.62 mas (van Leeuwen 2007).

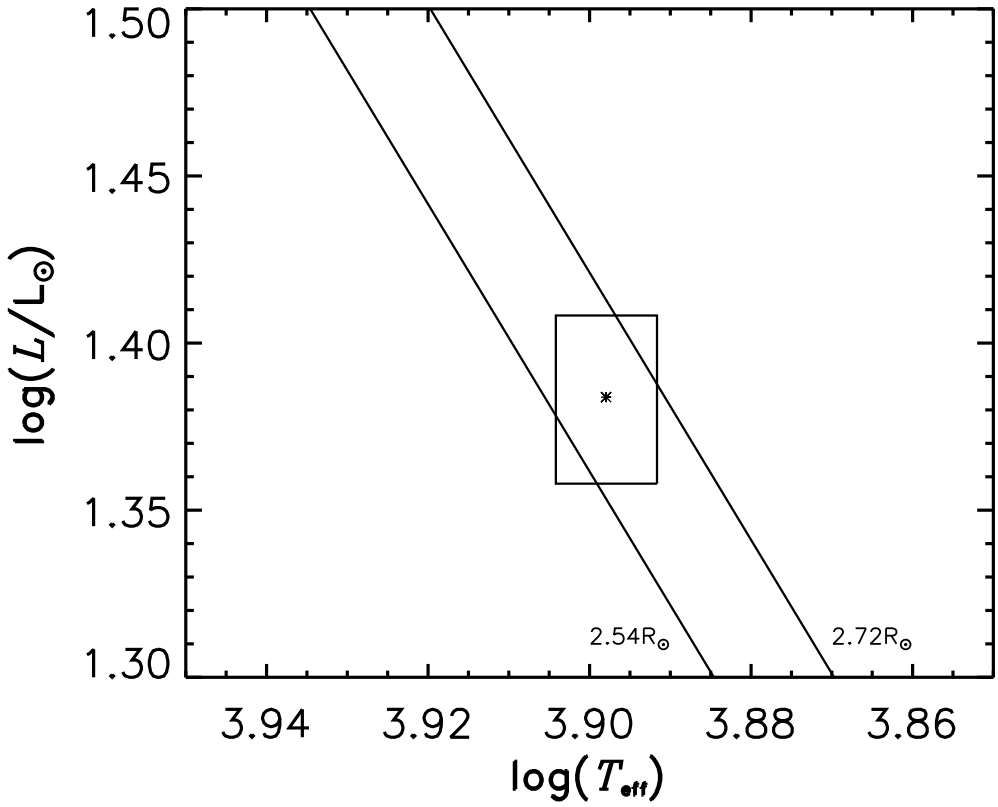

Figure 2.3: The position of β CrB A in the Hertzsprung-Russell diagram. The rectangle marks the estimated 1-σ uncertainty on $T_{\rm eff}$ and $L/\mathrm{L}_{\odot}$ (cf. Table 2.5) and the two diagonal lines correspond to constant radii consistent with the 1-σ uncertainty on the interferometric measurements.

Perraut et al. (2011) using the visible spectro-interferometer VEGA[18] installed on the optical CHARA array determined a limb-darkened angular diameter, $\theta_{\rm LD}$, of 0.564 ± 0.017 mas for γ Equ.

Due to its chemical inhomogeneities and flux redistributions, γ Equ shows a complex atmospheric structure. Consequently, the photometric and spectroscopic determinations of its effective temperature based on models that do not take these inhomogeneities into account are most likely biased. With this in mind, we made use of the measured angular diameter to determine an almost model independent effective temperature and luminosity for γ Equ, similarly to what we did for β CrB. To that aim, we computed the bolometric flux of γ Equ following the procedure described below.

[18]https://www.oca.eu/vega/en/present/

Table 2.6: UV spectra from IUE for γ Equ. LWP stands for Long Wavelength Prime and High@low stands for high dispersion rebinned to low dispersion.

Image Number	Camera	Dispersion	Aperture	Observation Start Time (UT)	Exposure Time (s)
06874	LWP	high@low	large	8/10/1985 18:55:04	599.531
09159	LWP	high@low	large	23/09/1986 20:41:13	539.730

2.2.3.1 Data

For the UV range, we collected two rebinned high resolution spectra of γ Equ from the Sky Survey Telescope, obtained at the IUE Newly Extracted Spectra (INES) data archive, covering the wavelength range [1850 Å; 3350 Å]. See Table 2.6 for the details of the spectra. There were no spectra available for the short wavelength range, between 1150 and 1980 Å. Based on the quality flag listed in the IUE spectra (Garhart et al. 1997) we removed all the bad pixels from the data, as well as all points with negative flux. The mean of the two spectra was then computed to obtain one single spectrum of γ Equ in the range $1850\,\text{Å} < \lambda < 3350\,\text{Å}$.

For the visible, we collected two spectra for γ Equ, one from Burnashev (1985), which is a spectrum from Kharitonov et al. (1978) reduced to the uniform spectrophotometric system of the "Chilean Catalogue", and one from Kharitonov et al. (1988). We verified that the latter was in better agreement with the Johnson (Morel & Magnenat 1978) and the Geneva (Rufener & Nicolet 1988) photometry than the former. To convert from Johnson and Geneva magnitudes to fluxes we used the calibrations given by Johnson (1966) and Rufener & Nicolet (1988), respectively.

We also collected photometric data of γ Equ B, in the visible. These data was used to estimate the contribution of γ Equ B to the total flux determined for the binary, as it will be explained below. The data available in the literature for γ Equ B is very limited. There are two Tycho magnitudes for γ Equ B from Fabricius et al. (2002), namely $m_{BT} = 9.85 \pm 0.03$ and $m_{VT} = 8.69 \pm 0.03$, and one *Hipparcos* magnitude from Perryman & ESA (1997), $m_{HP} = 9.054 \pm 0127$. To convert from Hipparcos/Tycho magnitudes into fluxes we used the zero points from Bessel & Castelli (private communication). See Table 2.7.

For the infrared, we collected the photometric data available in the literature for γ Equ. The calibrated observational photometric fluxes that we considered in this study are given in Table 2.8.

Table 2.7: Calibrated photometric m_{HP}, m_{BT} and m_{VT} fluxes for γ Equ B.

Band	$\lambda_{\rm eff}$ (Å)	Flux ($\times 10^{-12}$ erg cm^{-2} s^{-1} Å^{-1})	C_1
m_{HP}	5170	0.925	21.031
m_{BT}	4280	0.766	20.439
m_{VT}	5272	1.32	21.012

Table 2.8: Calibrated photometric infrared fluxes for γ Equ binary.

Band	$\lambda_{\rm eff}$ (Å)	Flux ($\times 10^{-12}$ erg cm^{-2} s^{-1} Å^{-1})	Source	Calibration
I	9000	15.53	1	a
J	12500	5.949	2	b
H	16500	2.420	2	b
K	22000	0.912	2	b
L	36000	0.140	2	b
M	48000	0.0512	2	b
J	12350	6.090	3	c
H	16620	2.584	3	c
K	21590	1.067	3	c

Source references: (1) Morel & Magnenat (1978); (2) Groote & Kaufmann (1983); (3) Cutri et al. (2003). Calibration references: (a) Johnson (1966); (b) Wamsteker (1981); (c) Cohen et al. (2003).

2.2.3.2 Bolometric flux and Effective temperature

To obtain de full SED for γ Equ and thus compute its bolometric flux we took the spectrum of the star that was obtained by combining the averaged IUE spectrum between 1854 Å and 3220 Å, the Kharitonov et al. (1988)'s spectrum from 3225 Å to 7375 Å, and, for wavelengths $\lambda < 1854$ Å and $\lambda > 7390$ Å we considered two cases: (1) we used the synthetic spectrum for the Kurucz model that best fitted simultaneously the star's spectrum in the visible and the star's photometry in the infrared and, (2) we performed a linear extrapolation between 506 Å and 1854 Å, considering zero flux at 506 Å and a linear interpolation to the infrared fluxes between 7390 Å and 1.6 $\times 10^6$ Å considering zero flux at 1.6 $\times 10^6$ Å. In case (1), in order to find the Kurucz model that best fits the visible and the IR data of the star, we ran a grid of Kurucz models with different effective temperatures, log g and metallicities. We considered two methods to calibrate the models, namely: (i) the star's flux at 5504 Å, f_{5504}, given by the Kharitonov et al. (1988)'s spectrum (ii) the relation $(R/d)^2$. For $R/d = \theta/2$ we used the limb-darkened angular diameter, $\theta_{\rm LD}$, given by Perraut et al.

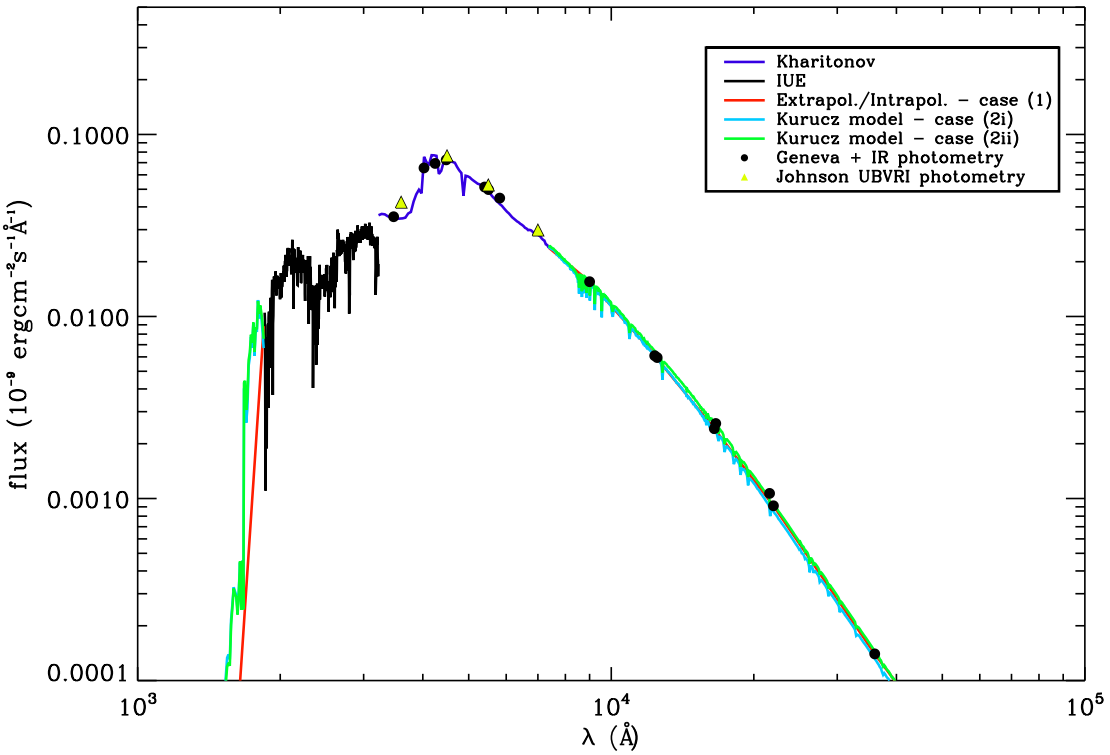

Figure 2.4: The whole spectrum obtained for γ Equ. Black line corresponds to the average of the IUE spectra and the dark blue line corresponds to the Kharitonov et al. (1988)'s spectrum. For wavelengths $\lambda < 1854$ Å and $\lambda > 7390$ Å, the figure shows the curve obtained using the interpolation method (red line), the Kurucz model that best fits the spectroscopy in the visible and the photometry in the infrared when models are calibrated with the star's magnitude m_V (light blue line) and when models are calibrated with the relation $(R/d)^2$ (green line). The Geneva and infrared photometry (circles) and Johnson UBVRI photometry (triangles) are overplotted to the spectrum.

(2011). The bolometric flux, $f_{\rm bol}$, was then computed by integrating the spectrum of the star, the effective temperature, $T_{\rm eff}$, was computed using Eq. (2.2.2), and the luminosity, L, was determined using Eq. (2.2.1). Figure 2.4 shows the final spectra obtained for γ Equ with the two different calibration methods and with the interpolation method.

The final spectra that we obtained for γ Equ contains the flux of both γ Equ A and γ Equ B. We then estimated the contribution of γ Equ B to the bolometric flux and, hence, to the effective temperature and luminosity that we determined for the binary. Knowing this contribution, we were able to determine the effective temperature of γ Equ A. To estimate γ Equ B's effective temperature we used its Tycho/Hipparcos magnitudes and color-$T_{\rm eff}$ calibration from Ramírez & Meléndez (2005). This was done assuming three different arbitrary

Table 2.9: Bolometric flux, $f_{\rm bol}$, and effective temperature, $T_{\rm eff}$, obtained for γ Equ, using three different methods (see text for details).

Calibration method	$f_{\rm bol}$ (erg cm^{-2} s^{-1})	$T_{\rm eff}$ (K)	$L/{\rm L}_\odot$
m_V	$(3.09 \pm 0.20)\times10^{-7}$	7348 ± 162	12.7±1.0
$(R/d)^2$	$(3.15 \pm 0.21)\times 10^{-7}$	7383 ± 166	12.9±1.0
Interpolation	$(3.11 \pm 0.21)\times 10^{-7}$	7360 ± 167	12.7±1.0

values and uncertainties for the metallicity, -0.4 ± 0.5, 0 ± 0.5 and 0.4 ± 0.5 dex. The values found for the effective temperature were $T_{\rm eff}$ = 4570, 4686 and 4833 K, respectively, with an uncertainty of ±40 K (Ramírez & Meléndez 2005). The metallicity, effective temperature, and m_V were used to estimate $\log g$, using theoretical isochrones from Girardi et al. (2000)[19]. For the three values of metallicities and $T_{\rm eff}$ mentioned above, we found $\log g$ = 4.58, 4.53, and 4.51, respectively. With these parameters we computed three Kurucz models and calibrated each of them in three different ways: (i) using the m_{HP} magnitude, (ii) using the m_{BT} magnitude, and (iii) using the m_{VT} magnitude.

2.2.3.3 Results

Our results for the bolometric flux, $f_{\rm bol}$, effective temperature, $T_{\rm eff}$, and luminosity, L, for γ Equ are shown in Table 2.9. The uncertainties in the three values of the bolometric flux given in Table 2.9 were estimated by considering an uncertainty of 10% on the total flux from the combined IUE spectrum (González-Riestra et al. 2001), an uncertainty of 4% on the total flux of the low resolution spectrum from Kharitonov et al. (1988), an uncertainty of 20% on the total flux derived from the Kurucz model, and an uncertainty of 20% on the total flux derived from the interpolation. The latter two are somewhat arbitrary. Given the abnormal flux distributions in roAp stars and the consequent deficient of Kurucz models in reproducing it, our attitude was one of being conservative enough to guarantee that the uncertainty in the total flux was not underestimated due to the difficulty in establishing these two values. The corresponding absolute errors were then combined to derive the errors in the flux which are shown in Table 2.9. Combining these with the uncertainty in the angular diameter and in the parallax, we derived the uncertainty in the individual values of the effective temperature and luminosity. To compute these errors we used the equation of propagation of errors. As a final result we take the mean of the three values and consider the uncertainty to be largest of the three uncertainties. Thus, the flux, the effective temperature, and luminosity adopted for γ Equ are given in Table 2.10. If, instead,

[19] http://stev.oapd.inaf.it/cgi-bin/param

Table 2.10: Final results for γ Equ.

	$f_{\rm bol}$ (erg cm^{-2} s^{-1})	$T_{\rm eff}$ (K)	$L/{\rm L}_\odot$	$R/{\rm R}_\odot$
γ Equ	$(3.12 \pm 0.21) \times 10^{-7}$	7364 ± 167	12.8 ± 1.0	2.20 ± 0.08

we took for the effective temperature and luminosity an uncertainty such as to enclose the three uncertainties, the result would be $T_{\rm eff} = 7364 \pm 182\,{\rm K}$, $L = 12.8 \pm 1.1\,{\rm L}_\odot$. The radius, R, was calculated using Eq. (2.2.6) and its uncertainty was calculated from the equation of propagation of errors. We obtained $R = 2.20 \pm 0.08\,{\rm R}_\odot$, for γ Equ.

The maximum flux found for γ Equ B through the procedure described in Section 2.2.3.2 was $0.19{\times}10^{-7}$ erg cm^{-2} s^{-1}, which corresponds to 6% of the total flux. This implies that the effective temperature of γ Equ A determined above may be in excess by up to 113 K due to the contamination introduced by this companion star. Also, the luminosity of γ Equ A is increased by up to $0.8\,{\rm L}_\odot$ when the companion is considered.

We used the values of the effective temperature and luminosity determined above, together with the radius to place γ Equ in the HR diagram as shown in Fig 2.5.

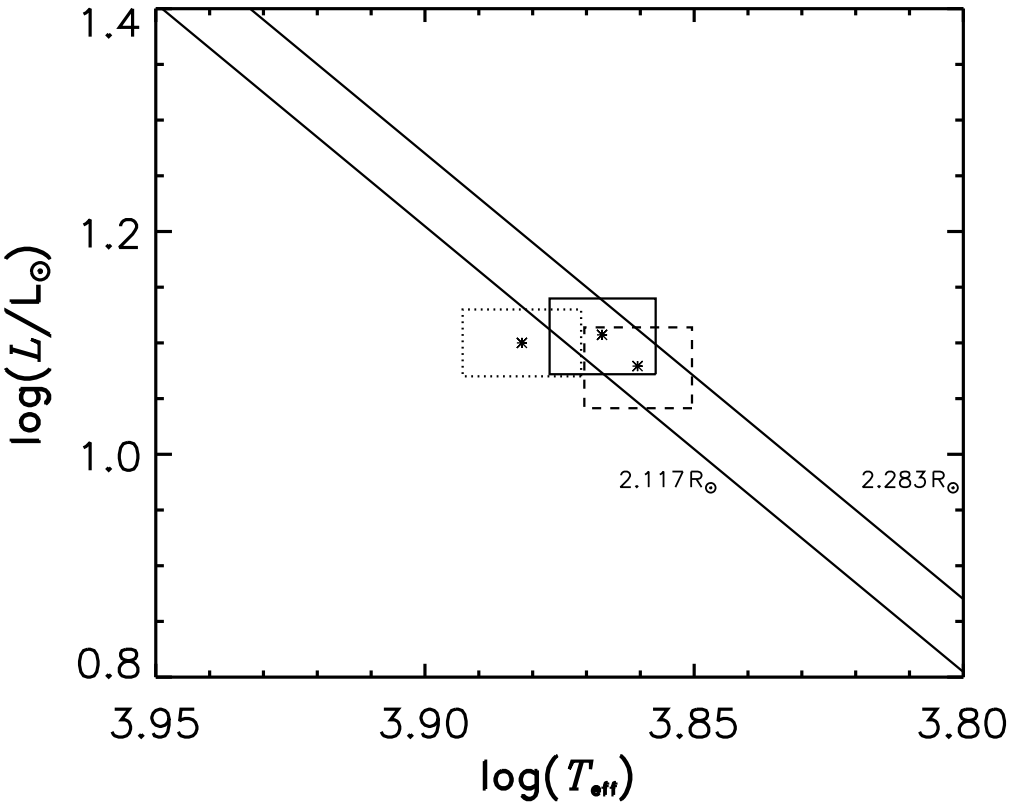

Figure 2.5: The position of γ Equ in the Hertzsprung-Russell diagram. The constraints on the fundamental parameters are indicated by the 1-σ error box (log $T_{\rm eff}$, log (L/L$_\odot$)) and the diagonal lines (radius). The box in solid lines corresponds to the results derived when ignoring the presence of the companion star, as shown in Table 2.10. The box in dashed lines corresponds to the results derived after subtracting from the total bolometric flux the maximum contribution expected from the companion (see text for details). The box in dotted lines corresponds to the fundamental parameters derived by Kochukhov & Bagnulo (2006).

2.3 Discussion and Conclusions

We have determined the bolometric flux and effective temperature of two roAp stars, namely β CrB and γ Equ using an only weakly model-dependent technique. The bolometric flux was computed from the combination of photometric and spectroscopic data available in the literature for the star, and Kurucz models atmospheres. The angular diameter of the stars derived from interferometric data was used, together with the bolometric flux and parallax, making it possible the determination of their effective temperatures and luminosities. Since both β CrB and γ Equ are binaries, we also determined the contribution of the secondary star to the derived parameters.

We recall that roAp stars show abnormal flux distributions. The bolometric corrections available in the literature are computed for normal stars, thus the bolometric flux (and hence the effective temperature) estimations of roAp stars from bolometric corrections are rather unreliable. When dealing with peculiar stars, like Ap stars, it is thus more adequate to properly compute the bolometric flux as we did here. However, it is precisely the difficulty in obtaining the full spectrum of the star that increases the uncertainty in the computed bolometric flux and, hence, in the luminosity and effective temperature. Moreover, the fact that the data available in the literature for the secondary star in these binary systems is almost inexistent results in an increase of the uncertainty in the derived parameters for the primary stars.

A wide range of values of the effective temperature is found in the literature for the roAp stars studied in this work. Table 2.11 shows a comparison between the values derived here and those found in the literature. For β CrB values from 7230 to 8700 K (considering 1-σ uncertainties) can be found in the literature. For γ Equ, the literature values range from 6811 K (Soubiran et al. 2010b,a) to 8982 K (Prugniel et al. 2011). Also, from a similar analysis of flux and interferometric data for the roAp star α Cir, we had previously found $T_{\rm eff} = 7420 \pm 170$ K (Bruntt et al. 2008). For this star the literature values for the effective temperature also span a large range, varying from 7470 K to 8730 K. These are typical examples of the large scatter found in the effective temperatures for chemically peculiar A stars. Kochukhov & Bagnulo (2006) found 7430 ± 200 K for β CrB, 7621 ± 195 K for γ Equ, and 7670 ± 200 K for α Cir. Our results don't agree with those from Kochukhov & Bagnulo (2006) only for β CrB A. We must remember, however, that the photometric indices of β CrB include both components of the binary, so their work will result in a temperature that is too low. Taking this into account we conclude that the photometric derivation of the effective temperature by Kochukhov & Bagnulo (2006) provides results for β CrB that are in agreement with ours within about 300 K.

Table 2.11: Effective temperature for β CrB, γ Equ and α Cir obtained in our work (2nd column), the range of effective temperatures found in the literature for the three stars (3rd column), and their effective temperature given by Kochukhov & Bagnulo (2006) (4th column).

Star	$T_{\rm eff}$ (K) (our work)	$T_{\rm eff}$ (K) (range in literature)	$T_{\rm eff}$ (K) (Kochukhov & Bagnulo 2006)
β CrB	7906 ± 114	7230 – 8700	7430 ± 200
γ Equ	7251 ± 167	6811 – 8982	7621 ± 195
α Cir	7420 ± 170[a]	7470 – 8730	7670 ± 200

[a] $T_{\rm eff}$ values derived in our previous work and presented in Bruntt et al. (2008)

Our results are expected to be less model dependent than those estimated from photometric indices, such as the ones derived by Kochukhov & Bagnulo (2006). In our method, we only use the models to estimate the bolometric flux in the regions where the flux is almost negligible, and for the adopted limb darkening. For instance, our result on $T_{\rm eff}$ for β CrB A, 7906 ± 114 K, is in excellent agreement with that obtained by Bruntt et al. (2010) of 7980 ± 180 K, the only difference between their derivations being the fact we considered the Kurucz models and they considered interpolations in the wavelength range where data was not available for the star.

We hope that combining accurate determinations of the effective temperature and luminosity with asteroseismic data may have an important impact on the modelling of these pulsating roAp stars in future work.

Chapter 3

Stellar Modelling

In this Chapter I will present the work we performed on the forward modelling of particular pulsating stars. By forward stellar modelling I mean the procedure leading to the comparison between the observed non-seismic and seismic observables of a pulsating star and the corresponding quantities computed for models (model observables), with the objective of identifying the model that best reproduces the data, and hence determine stellar properties such as the mass and age. This comparison between the model observables and the data is also important in order to improve the physics incorporated in the former.

As will be discussed below, in Section 3.4, the outer convective layers of stars are not properly modelled. This results on computed frequencies that are shifted from the observed ones. An empirical correction was proposed in the literature to correct the model frequencies for this shift. In this Chapter we aim at applying and test this empirical correction to the model frequencies computed for three stars. One is more evolved than the Sun (β Hyi), the second one is hotter than the Sun (KIC 10273246), and the last is a binary whose components are similar to the Sun (16 Cyg). This provides us means of testing the empirical correction in a relatively wide range of stellar properties.

3.1 Introduction

Stellar models consist on a set of physical variables - such as the temperature, luminosity, chemical composition, etc - usually expressed as a function of the distance r from the stellar centre. These describe the interior of a star at a given evolutionary state. Stellar evolutionary codes are computational programs used to construct these static models and to evolve them over time. This should be done by numerically solving the magnetohydrodynamic equations

of the stellar structure and evolution. A detailed description of the stellar structure and evolution equations can be found in a number of books, such as, Kippenhahn & Weigert (1990), Hansen et al. (2004) and Maeder (2009). However, the hydrodynamical problem is too complicated to be treated in a complete way. To make the calculations possible, simplifications are commonly applied, such as the assumption of spherical symmetry, which implies, in particular, neglecting rotation. Also often neglected are the large scale magnetic fields and mass-loss. Thus, in general, one assumes that the forces that act on the stellar matter are the thermal pressure and the gravity, and, hence, that the star is in hydrostatic equilibrium. In addition, there are physical mechanisms acting inside a star, such as convection, that are poorly understood and, consequently, treated in a very simplistic manner.

To solve the equations of stellar structure and evolution, within the simplifications mentioned above, it is also necessary to choose physical formalisms that depend on the microscopic properties of the stellar matter, such as the equation of state, opacity, the transport of radiation and the nuclear reactions (see, e.g., Kippenhahn & Weigert 1990).

To model the stars presented in this Chapter we used the 'Aarhus STellar Evolution Code' (ASTEC, Christensen-Dalsgaard 2008a). This code is described in detail in the reference given above and, hence, we refrain from repeating such detailed descriptions here. However, for the sake of clarity, in the next section we describe some of the input physics considered in the modelling of the targets.

Finally, since the aim of the work was to model stellar pulsations we had, in addition, to compute stellar pulsation frequencies. For that we used the Aarhus adiabatic oscillation code (ADIPLS, Christensen-Dalsgaard 2008b). When computing the frequencies, two alternative boundary conditions can be applied in the outer boundary of the stellar atmosphere. The first corresponds to a full reflection of the waves, while in the second only waves which frequencies are below the acoustic cut-off frequency are considered, and these are matched to an exponential decaying solution in an isothermal atmosphere. For the work presented in this Chapter we use always the latter boundary condition. The former boundary condition, expressed by $\delta p = 0$, where δp is the Lagrangian perturbation to the pressure, will be used in Chapter 4.

3.2 Model input physics

Equation of state

The equation of state (EOS) relates thermodynamical quantities, such as the density, pres-

sure, temperature, and chemical composition (**X**), in the form of $\rho(p, T, \mathbf{X})$, $p(\rho, T, \mathbf{X})$, or $T(\rho, p, \mathbf{X})$. It is one of the *physical ingredients* required to obtain the solutions to the equations of the stellar structure. An EOS must take into account a variety of effects, such as radiation pressure, ionization, degeneracy, among others. These are described in detail in, e.g., Kippenhahn & Weigert (1990) and Hansen & Kawaler (1994). Accurate equations of state have been calculated by specialized groups that make them available on tables ready to be interpolated, as needed. The two most used tables are known as OPAL (by the Livermore group, Rogers et al. 1996) and MHD[20] (Hummer & Mihalas 1988; Daeppen et al. 1988; Mihalas et al. 1988, 1990; Gong et al. 2001) associated with the Opacity project.

In our work, in the ASTEC code, we considered the most up-to-date OPAL 2005 equation of state tables[21] (Rogers & Nayfonov 2002).

Opacity

Opacity, also know as the absorption coefficient $\kappa = \kappa(\rho, T, \mathbf{X})$, is a quantity that determines the transport of radiation through matter. It represents the ability of stellar material to absorb heat, primarily by the interaction of photons with the particles of the gas as they pass through. In general, the opacity depends on the energy of the photon, i.e. on its frequency, ν. Nevertheless, in stellar structure calculations, we need only to know, in average, how the radiation interacts with the gas and is absorbed. Thus, a frequency average of the opacity, called the Rosseland mean opacity, κ_R, is considered.

Nowadays, numerical opacity tables are available for different chemical mixtures and give κ_R for a large range of ρ and T. Since the calculation of opacity requires accurate knowledge about the detailed thermodynamical state of the gas, such as the ionization degree of the various species, it is not surprising that the groups involved in the calculation of the EOS are the same as those involved in the calculation of opacities.

In our work, in the ASTEC code we used the OPAL95 opacities (Iglesias & Rogers 1996) complemented by low-temperature opacities from Ferguson et al. (2005). The opacities were calculated with the solar mixture of Grevesse & Noels (1993).

Convection

Energy transport by convection in a star occurs when radiation can no longer transport the total flux of energy. This happens when opacity or the amount of energy to be transported gets too high. The “standard” treatment of turbulent convection is the standard mixing-length theory (MLT) from Böhm-Vitense (1958), where the characteristic length of tur-

[20] MHD tables are available at anonymous FTP at $ftp://ftp.usc.edu/pub/astro-physics/mhd\_tables/$

[21] OPAL tables available at $http://opalopacity.llnl.gov/EOS\_2005/$

bulence, called the mixing-length $l_{\rm ML}$, scales directly with the local pressure scale height, H_p, as $l_{\rm ML} = \alpha_{\rm ML} H_p$, with $\alpha_{\rm ML} > 1$. The precise value of the mixing-length parameter $\alpha_{\rm ML}$ is not in general fixed by fundamental physics but it is chosen to fit the star being modelled. An exception to this is the case of 3-D numerical simulations of convection, as those proposed by Kim et al. (1996), Trampedach et al. (1999), Trampedach (2007), where $\alpha_{\rm ML}$ is calibrated, as a function of stellar parameters by matching 1-D models to the results of the 3-D simulations. Alternatively, sometimes, the value of $\alpha_{\rm ML}$ found when modelling the Sun imposing its present radius is used to model other stars.

The standard MLT is a local formulation of convection. Non-local extensions of MLT have been developed by Unno (1967), who also considered the time-dependent case relevant for the study of oscillations, and by Gough (1977a,b). Also, Dupret et al. (2006) constructed a non-local MLT formulation based on the 3-D convection simulations.

Canuto & Mazzitelli (1991, CM) have presented an alternative to MLT. While MLT considers only one turbulent eddy, representing an "average" of the turbulent eddies, the models by Canuto & Mazzitelli (1991) considered the full spectrum of turbulent eddies (FST). In their paper, they proposed two expressions for the mixing-length: (1) the standard $l_{\rm ML} = \alpha_{\rm CM} H_p$, with $\alpha_{\rm CM}$ a free parameter depending on the microphysics, in general $\alpha_{\rm CM} < 1$, (2) a new parameter-free expression $l_{\rm ML} = z$, with z being the distance of the convective layer to the top of the convection zone determined by the Schwarzschild criterion. Canuto, Goldman, and Mazzitelli (Canuto et al. 1996, CGM) mentioned that $l_{\rm ML}$ should also allow for overshooting, so they considered in expression (2) an extra term $z_{\rm OV}$ parametrised by H_p at the top of the convective layer: $l_{\rm ML} = z + \beta H_p^{top}$. When including this term they claim that they obtain an improved fit to the solar model. Ventura et al. (1998) mentioned that close to the convective boundaries the more physically correct choice is expression (2), but far from the boundaries, $l_{\rm ML}$ should approach the hydrostatic scale length H_p. They therefore adopted z as the harmonic mean between the distance of the convective layer to the top of the convective zone and the distance to the bottom, i.e. $l_{\rm ML} = z^{up} z_{low}/(z^{up} + z_{low})$, where z^{up} is the distance from the top of convection increased by βH_p^{top}, and analogously for z_{low}.

Trampedach (2010) has provided a comparison between the three above mentioned 1-D formalisms (MLT, non-local MLT and CGM) and the 3-D formalisms for convection. The author found local MLT to be the most realistic of the three 1-D prescriptions, despite its shortcomings. It must be noted that the treatment of convection is more important for the outermost parts of the convective envelopes where the temperature gradient of the star is substantially different from the adiabatic temperature gradient.

Convective overshoot

Overshooting (OV) exists when the convective movements of the gas in the convectively unstable regions cause extra mixing beyond the border of such regions. Different treatments for the overshooting regions have been presented in the literature, however, these are largely simplified and have inadequacies (Renzini 1987; Canuto 1997).

There are two main aspects to take into account when a given prescription in the treatment of convective overshoot is considered, namely the temperature stratification and the mixing within the overshoot layer.

In the ASTEC code, regarding the temperature stratification, we assumed that the temperature gradient of the star in that region is not modified by the overshooting, i.e. the temperature gradient is assumed to be the radiative temperature gradient ($\nabla_{\rm OV} = \nabla_{\rm rad}$). Regarding the mixing of the stellar material within the overshooting layer we considered it to be highly efficient, taking place on the same time scales as in the convectively unstable region. Therefore, the overshooting region is fully mixed.

The value for the extent of overshooting, $d_{\rm OV}$, was determined by adopting the standard prescription (e.g. Maeder 1975) in which it is parametrized as a fraction of the pressure scale height, $d_{\rm OV} = \alpha_{\rm OV} H_p$, with the scaling factor $\alpha_{\rm OV}$ as a free parameter.

In our work, we only considered convective core overshoot. Core overshoot has more effect on the stellar evolution than the envelope overshooting. It increases and changes the chemical composition of the convective core by bringing more hydrogen into it, thus prolonging the life of the star in the main-sequence phase (see Figure 3.1). In practice, since the core can be very small, ASTEC assumes $d_{\rm OV} = \alpha_{\rm OV} min(r_{core}, H_p)$, where r_{core} is the radius of the convective core.

Nuclear reaction rates

Most stars live on thermonuclear fusion, where several lighter nuclei fuse to form a heavier one. The rates of this nuclear reactions are determined by the relative velocity between the various nuclei, as well as by the cross-sections of the reactions. The values for the nuclear reaction rates are obtained experimentally, however with large uncertainties, since the energies associated to stellar interiors are always too low to overcome the Coulomb potential barrier so that the nucleons can fuse. Therefore, theoretical models that extrapolate, in a reliable way, the experimental data to the astrophysical relevant energies are still needed.

Nevertheless, there are tabulations of nuclear reaction rates and energy production, and the most used today are those from Caughlan & Fowler (1988), and, more recently, those of Adelberger et al. (1998) and the *NACRE* collaboration (Angulo et al. 1999).

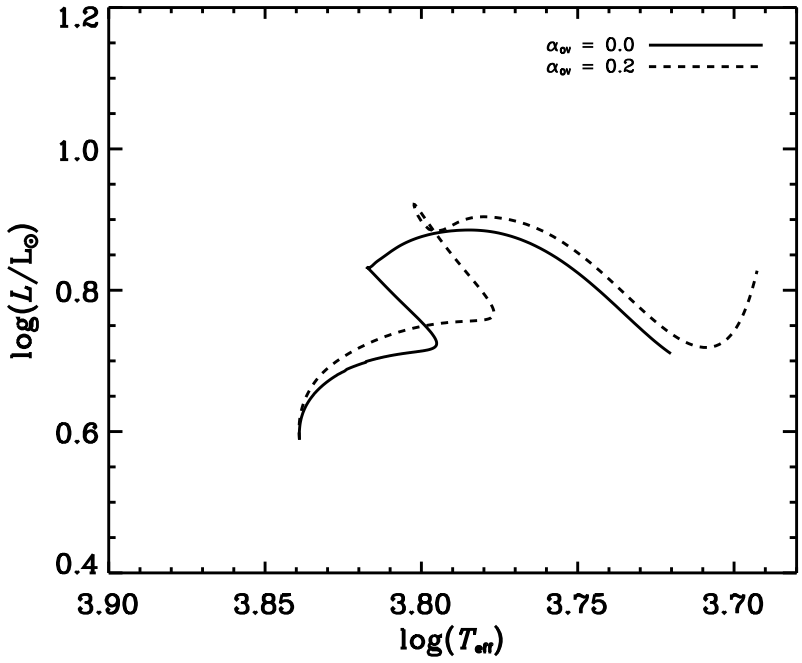

Figure 3.1: Two evolutionary tracks from ZAMS to post-main sequence (last models with $X_c = 10^{-10}$ and ages of 2.88 (no overshoot) and 3.15 Gyrs (with overshoot)) with $M = 1.4\,\mathrm{M}_\odot$, $Z/X = 0.0245$, $\alpha_{\mathrm{ML}} = 1.8$, and $\alpha_{\mathrm{OV}} = 0.0$ (filled line) and $\alpha_{\mathrm{OV}} = 0.2$ (dashed line). The hook shape in the evolutionary track is due to the fact that the star has grown a convective core during the main-sequence phase.

The nuclear parameters in ASTEC have been largely based on Parker (1986). In ASTEC it is possible to use one of the nuclear reaction rates previously mentioned. In our work we considered the ones by Angulo et al. (1999).

Diffusion and gravitational settling

Diffusion and settling are mostly important outside the convective regions. Gravitational settling refers to the settling of the heavier elements towards the centre of the star and rising of light elements, such as hydrogen, to the surface. Diffusion acts roughly in the opposite direction resulting in smoother gradients in the chemical composition. The two mechanisms are often neglected in standard modelling. When considered in the ASTEC code, diffusion and settling were treated in the approximations proposed by Michaud & Proffitt (1993). We refer to Christensen-Dalsgaard (2008a) for a detailed description.

3.3 Observational constraints

The fundamental parameters of a pulsating star that are obtained directly from observations through techniques such as spectroscopy, photometry, astrometry and interferometry are used as observational constraints to the models. These are often called non-seismic constraints. As a starting point for stellar modelling, the non-seismic data such as the luminosity or the logarithm of gravity and the effective temperature are used to place the star in the HR diagram. Unfortunately, these data alone provide very weak constraints for the modelling. For instance, models with different input parameters and/or physics can have the same position in the HR diagram. A classical example is the mass-helium degeneracy (Fernandes & Monteiro 2003). This degeneracy can be partially lifted if we also consider as observational constraints the seismic data. These can be either particular combinations of frequencies, such as the the large and small frequency separations, or the individual frequencies, for a more detailed modelling.

In the work presented in this Chapter, when modelling the individual stars we considered both the non-seismic and seismic data.

3.4 Near-surface corrections

It is well known from helioseismology that there is a systematic offset between the observed and the computed oscillation frequencies of the Sun. This offset, which is nearly

independent of the angular degree, l, of the mode and affects the highest frequencies the most (Christensen-Dalsgaard & Thompson 1997), arises from the improper modelling of the surface layers. Therefore, the offset is also expected to be present when comparing the observed and computed frequencies for other stars. This offset is a matter of worry specially when using individual frequencies as constraints for the modelling of solar-like pulsators, such as those described in this Chapter. Kjeldsen et al. (2008) used the solar data to derive an empirical correction for the near-surface offset, which can, in principle, be applied to other stars. Nevertheless, this approach is purely empirical and is based on strong assumptions that need to be further tested. One main motivation for the work presented here is to verify if such empirical correction works also for other stars.

For the Sun, the difference between the observed, $\nu_{\rm obs}$, and computed frequencies of the best model, $\nu_{\rm best}$, was shown by Kjeldsen et al. (2008) to be well approximated by a power law fit given as

$$\nu_{\rm obs}(n) - \nu_{\rm best}(n) = a \left[\frac{\nu_{\rm obs}(n)}{\nu_0} \right]^b , \tag{3.4.1}$$

where n is the radial order, and ν_0 is a reference frequency. In our work this reference frequency was chosen to be the frequency at maximum power. Since the offset is independent of l, the authors considered only radial ($l = 0$) modes. Note that the 'best model' is the one that best represents the solar interior but still fails to model its near-surface layers. They also argued that the frequencies of a reference model, $\nu_{\rm ref}$, which is close to the best one, can be scaled from $\nu_{\rm best}$ by a factor r, i.e.,

$$\nu_{\rm best}(n) = r\nu_{\rm ref}(n). \tag{3.4.2}$$

Then Eq. (3.4.1) becomes

$$\nu_{\rm obs}(n) - r\nu_{\rm ref}(n) = a \left[\frac{\nu_{\rm obs}(n)}{\nu_0} \right]^b . \tag{3.4.3}$$

Kjeldsen et al. (2008), using the GOLF data (Lazrek et al. 1997) and the solar model S of Christensen-Dalsgaard et al. (1996), found $b = 4.90$. They suggest that this value, although varying slightly (between 4.40 and 5.25), depending on the range of radial orders included in the calibration, may be used in the modelling of solar-like stars. This variation in b only leads to a variation in a of less than 0.1 μHz, in all cases. Using their value for b it is possible to determine r and a from Eqs (6) and (10) of Kjeldsen et al. (2008). Assuming that a similar offset occurs for other solar-like stars, they showed how to use the solar b value to determine r and a from the observed frequencies of $l = 0$ modes, and, consequently, use Eq. (3.4.3) to calculate the correction that must be applied to the frequencies computed for all l for a given stellar model. They noted that the correction applied to the mixed modes should be

less than that for the pure p modes. We should also note that due to the nature of the power law, the low frequencies are not significantly affected, which is expected since they are less sensitive to the outer structure of the star.

3.5 Modelling methodology

The modelling of the individual stars presented in this Chapter was based on a grid forward approach. In this approach we consider grids of models with different input parameters and physics. For each grid, we take the models whose parameters are within the 3-σ uncertainties derived from the non-seismic observations of the star under study, and compute the corresponding oscillation frequencies. The theoretical frequencies are then compared with the observed ones in order to find the best-matching model.

In our work, we started by considering two methods to find the model that, to the closest extent possible, reproduces the observed non-seismic and seismic data of a star. In what follows I will describe each method separately.

Method 1

In this case we followed closely the work of Kjeldsen et al. (2008) and considered the best representative model to be the one having the value of r closest to 1, which means, from Eq. (3.4.2),

$$\nu_{\rm ref}(n) \approx \nu_{\rm best}(n). \tag{3.5.1}$$

Using the values of r and a found for this model, we then computed the correction factor to be applied to the model frequencies and compared the latter with those observed. Note, however, that in this method r is calculated using only the observed radial modes together with the corresponding model radial modes. If we assume that the best model is the one which has r closest to 1 then we are assuming the model that has the radial frequencies matching most closely the observed $l = 0$ modes also has the non-radial frequencies matching best the observed $l = 1$ and 2 modes. However, this may not be true.

Method 2

In this case we applied a least-square methodology, where we searched for the model which frequencies minimize the χ^2 function defined by,

$$\chi^2 = \frac{1}{N}\sum_{n,l}\left(\frac{\nu_{\rm ref,corr}(n,l) - \nu_{\rm obs}(n,l)}{\sigma(\nu_{\rm obs}(n,l))}\right)^2, \tag{3.5.2}$$

where N is the total number of modes considered, $\nu_{\rm ref,corr}(n,l)$ are the frequencies of modes with radial order n and degree l of a reference model, corrected for the surface effects, and σ represents the uncertainty in the observed frequencies. Note that the n value, when given associated with the observed frequencies, should not be used as a constraint since it is model dependent. On the other hand, the l value can be objectively obtained from observations, with some problematic exceptions such as in the case of Procyon (Bedding et al. 2010) and HD 49933 (Appourchaux et al. 2008).

The correction term, as shown in the right-hand side of Eq. (3.4.1) can only be applied to the frequencies of the best model. In order to compute the correction term, since we have a set of reference models and we do not know which of these is the best model, we assume that the corrected best, $\nu_{\rm best,corr}$, and reference model $\nu_{\rm ref,corr}$ frequencies also scale as

$$\nu_{\rm best,corr}(n,0) = r\nu_{\rm ref,corr}(n,0). \tag{3.5.3}$$

We note that this is a good approximation because the surface corrections to the frequencies are much smaller than the frequencies themselves. Moreover, since $\nu_{\rm best,corr} \simeq \nu_{\rm obs}$

$$\nu_{\rm ref,corr}(n,0) = \nu_{\rm ref}(n,0) + \left(\frac{a}{r}\right)\left[\frac{\nu_{\rm obs}(n,0)}{\nu_0}\right]^b. \tag{3.5.4}$$

Since the effect of the surface layers is essentially independent of l, we thus have from Eq. (3.5.2),

$$\chi^2 = \frac{1}{N}\sum_{n,l}\left(\frac{\nu_{\rm ref}(n,l) + \tilde{CT}(n,0) - \nu_{\rm obs}(n,l)}{\sigma(\nu_{\rm obs}(n,l))}\right)^2, \tag{3.5.5}$$

where $\tilde{CT}(n,0)$ is the correction term for the $l = 0$ modes, $CT(n,0) = \left(\frac{a}{r}\right)\left[\frac{\nu_{\rm ref}(n,0)}{\nu_0}\right]^b$, interpolated to the frequencies of the modes of a given degree l. Note that, in practice, the term $(a/r)[\nu_{\rm obs}(n,0)/\nu_0]^b$ on the right-hand side of Eq. (3.5.4) was replaced by $(a/r)[\nu_{\rm ref}(n,0)/\nu_0]^b$. The reason is twofold: first because we do not know a priori the n value of the observed frequencies, in order to compare them to the model ones, and second to enable us to correct all the reference model frequencies, instead of only the frequencies with the same radial order as those observed. As the difference between these terms is small for the best-fitting model, it is safe to perform this replacement.

The final equation for the χ^2 should be set after considering also the mixed modes. They should not be affected by the surface layers as much as the p modes (Kjeldsen et al. 2008), so the correction term should be small for them. Specifically, at a given frequency we expect the near-surface effects to scale inversely with the mode inertia, which is much higher for the mixed modes than for the p modes. Thus we scaled the correction term by the inverse of the ratio Q_{nl} between the inertia of the mode and the inertia of a radial mode of the same

frequency (Aerts et al. 2010). Taking that into account, Eq. (3.5.5) becomes

$$\chi^2 = \frac{1}{N}\sum_{n,l}\left(\frac{\nu_{\rm ref}(n,l) + \left(\frac{1}{Q_{nl}}\right)\tilde{CT}(n,0) - \nu_{\rm obs}(n,l)}{\sigma(\nu_{\rm obs}(n,l))}\right)^2 . \quad (3.5.6)$$

The best model is the one that minimises Eq. (3.5.6). Note that in this equation only the seismic data is considered in the computation of the χ^2. We opted not to include the non-seismic data in the calculation of the χ^2 since: (1) we have already constrained the models from non-seismic data by computing the frequencies only for those that lay inside 3-σ uncertainties and (2) Metcalfe et al. (2010) showed that once we have models in a region very close to the observed atmospheric parameters, the determination of the best model depends much more on the individual frequencies. Nevertheless, we could compute a χ^2 that would include both the seismic and non-seimic constraints or compute them separately (Metcalfe et al. 2010).

Method 1 was only applied in the modelling of β Hyi (see Subsection 3.6.1), for which we also applied *Method 2*. The reason is that we concluded that *method 2* is more adequate to find the best model, since it takes into account all the individual frequencies, the mixed modes, and also the uncertainties on the observed frequencies.

3.6 Application to individual stars

In this section I will present the results we obtained through forward modelling of three solar-like pulsators, namely β Hyi, KIC 10273246, and 16 Cyg. Observations of β Hyi were performed from the ground, while KIC 10273246 and 16 Cyg were observed by the *Kepler* satellite. In what concerns the two *Kepler* stars, I was assigned to lead the work on the modelling of KIC 10273246, while the modelling of 16 Cyg, was lead by Travis Metcalfe, with contributions by several researchers/teams, including myself, who performed independent modelling of the star.

3.6.1 β Hyi

β Hydri (β Hyi, HD 2151, HR 98, HIP 2021) is a single, bright subgiant star (m_V = 2.80). It is the closest subgiant star, with a spectral and luminosity type between G2 IV (Hoffleit & Warren 1995; Evans et al. 1957) and G0 V (Gray et al. 2006), and it is one of the oldest stars in the solar Galactic neighbourhood. It is frequently regarded as representing the future of the Sun (Dravins et al. 1993a,b,c), making it a particularly interesting object of study.

Improvements to the fundamental parameters of β Hyi have been presented in a number of recent works. Recent interferometric measurements of β Hyi have yielded an accurate (0.8%) angular diameter for this star (North et al. 2007). Also, the *Hipparcos* parallax of β Hyi has been improved from an uncertainty of 0.4% (Perryman & ESA 1997) to 0.08% (van Leeuwen 2007). The combination of these two values gives a direct measure of β Hyi's radius with high accuracy. Moreover, since the bolometric flux of this star is known (Blackwell & Lynas-Gray 1998), its position in the HR diagram is, in principle, well-constrained.

Bedding et al. (2007) observed β Hyi during more than a week with the high-precision spectrographs HARPS and UCLES. They were able to identify 28 oscillation modes that included some mixed modes of spherical degree $l = 1$. As mentioned before this modes provide useful information about the stellar core and hence about the age of the star.

Theoretical models of β Hyi based on its seismic and non-seismic data have been published by Fernandes & Monteiro (2003), Di Mauro et al. (2003), and Doğan et al. (2010). Fernandes & Monteiro (2003) examined the position of β Hyi in the HR diagram by first considering the non-seismic data of the star. In order to estimate the mass of β Hyi, they used available seismic data, namely the large frequency separation, to remove partially the helium-content vs mass degeneracy that exists when only non-seismic observational constraints are used. They also emphasized the usefulness of individual frequencies to constrain the age of β Hyi due to the presence of mixed modes in its observed oscillation spectrum. Di Mauro et al. (2003) computed models of β Hyi, also based on its global parameters. They used the oscillation frequencies of β Hyi to compare with the model frequencies. Their theoretical models reproduced the observed oscillation spectrum of β Hyi well, as well as the observed large and small frequency separations, after they applied an ad-hoc shift to the computed frequencies.

In order to model this star we used up-to-date non-seismic and seismic constraints. This was the first star for which we applied the modelling methodology described in Section 3.5.

In what follows I will present the constraints that we considered to model the star, the input parameters used to construct the grid of models, and the results with discussion and conclusions.

3.6.1.1 Non-seismic constraints

The most recent determination of the radius of β Hyi is given by Kjeldsen et al. (2008). The radius was obtained by combining the interferometric angular diameter of the star,

Table 3.1: Stellar properties of β Hyi. The luminosity, L, and radius, R, are expressed in solar units. θ stands for the angular diameter, Π for the *Hipparcos* parallax, $T_{\rm eff}$ for the effective temperature, [Fe/H] is the metallicity, and Z/X is the mass ratio of heavy elements to hydrogen.

	Value	Reference
θ (mas)	2.257 ± 0.019	North et al. (2007)
Π (mas)	134.07 ± 0.11	van Leeuwen (2007)
$R/\mathrm{R}_\odot$	1.809 ± 0.015	Kjeldsen et al. (2008)
$L/\mathrm{L}_\odot$	3.494 ± 0.087	Current work
$T_{\rm eff}$ (K)	5872 ± 44	North et al. (2007)
[Fe/H]	-0.10 ± 0.07	Bruntt et al. (2010)
Z/X	0.019 ± 0.003	Current work

$\theta = 2.257 \pm 0.019$ mas (North et al. 2007), with the revised *Hipparcos* parallax, $\Pi = 134.07 \pm 0.11$ mas (van Leeuwen 2007) (see Eq. (2.2.6)).

To compute the luminosity of β Hyi we used Eq. (2.2.1). We considered the value for the bolometric flux from North et al. (2007), $f_{\rm bol} = (2.019 \pm 0.05) \times 10^9\,\mathrm{W\,m^{-2}}$ (Blackwell & Lynas-Gray 1998, the uncertainty on $f_{\rm bol}$ is from di Benedetto 1998) and the revised *Hipparcos* parallax (van Leeuwen 2007). Adopting $\mathrm{L}_\odot = 3.842 \times 10^{26}$ W with an uncertainty of 0.4% (Bahcall et al. 2001), we found $L = 3.494 \pm 0.087\,\mathrm{L}_\odot$ for β Hyi. For the $T_{\rm eff}$ we adopted the value of North et al. (2007), which is derived from the direct measurement of the angular diameter.

We adopted in our analysis the most recent value for the metallicity of β Hyi, given by Bruntt et al. (2010), namely $[\mathrm{Fe/H}] = -0.10 \pm 0.07$. We calculated the mass fraction of metals, Z, from the metallicity, using the following approximation, valid for Population I stars which do not present the α-elements enrichment seen in metal deficient stars (Wheeler et al. 1989):

$$\begin{aligned}[\mathrm{Fe/H}]_{\rm s} &\equiv \log\left(\frac{Z_{\rm Fe}}{Z}\right)_{\rm s} + \log\left(\frac{Z}{X}\right)_{\rm s} - \log\left(\frac{Z_{\rm Fe}}{Z}\right)_\odot - \log\left(\frac{Z}{X}\right)_\odot \\ &= \log\left(\frac{Z}{X}\right)_{\rm s} - \log\left(\frac{Z}{X}\right)_\odot ,\end{aligned} \tag{3.6.1}$$

where $[\mathrm{Fe/H}]_{\rm s}$ is the star's metallicity; $Z_{\rm Fe}$ and X are the iron and hydrogen mass fractions, respectively; and $(Z/X)_\odot$ is the ratio for the solar mixture. We used $(Z/X)_\odot = 0.0245$ (Grevesse & Noels 1993). This gives $(Z/X) = 0.019 \pm 0.003$ for β Hyi.

From spectral analysis, Dravins & Nordlund (1990) found $v \sin i = 2 \pm 1\,\mathrm{km\,s^{-1}}$ for β Hyi. More recently, Bruntt et al. (2010) found $v \sin i = 2.7 \pm 0.6\,\mathrm{km\,s^{-1}}$, and Hekker & Aerts

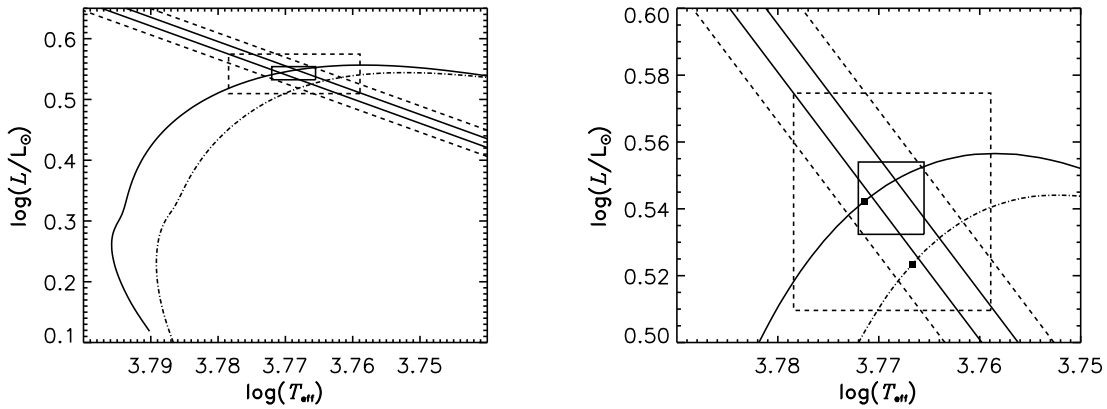

Figure 3.2: Left panel: The position of β Hyi in the HR diagram. The constraints on the fundamental parameters ($T_{\rm eff}$, $L/{\rm L}_\odot$) are indicated by the 1-σ error box (solid) and on the radius by diagonal solid lines. We also show the corresponding 3-σ uncertainties by dashed lines. Two evolutionary tracks for the best models found using *method 2* (cf. Table 3.5) are plotted with dash-dotted and solid curves, representing the models with and without gravitational settling and diffusion, respectively. Right panel: the same as in the left panel but zoomed in. The selected models are marked by filled squares.

(2010) from spectroscopic line-profile analysis, found $v \sin i = 4.3\,{\rm km\,s^{-1}}$. From their analysis, Hekker & Aerts (2010) attempted to determine the inclination angle, i, of β Hyi, suggesting a value of $55 \pm 17^\circ$ for this star. Thus, the effect of rotation on the modelling of the structure of the star can be neglected. Similarly, since the resulting rotational splitting is comparable with the error in the observed frequencies (see Section 3.6.1.2), in the present analysis we neglect the effects of rotation on the frequencies.

The position of β Hyi in the HR diagram is shown in Figure 3.2 and the fundamental parameters adopted in this work are given in Table 3.1.

3.6.1.2 Seismic constraints

Asteroseismic observations of β Hyi have been reported by Bedding et al. (2007). They found an excess power centred around 1 mHz with a peak amplitude of $\sim$50 cm s^{-1}, and oscillation frequencies showing a comb-like structure typical of solar-like oscillations with a large frequency separation for the $l = 0$ modes, $\Delta\nu_{n0}$, of $57.24 \pm 0.16\,\mu$Hz. They also identified 28 mode frequencies in the range $0.7 < \nu < 1.4$ mHz with angular degrees $l = 0$, 1, and 2, three of which were identified as $l = 1$ mixed modes. In this work, we used the updated list of 33 observed frequencies given in Table 3.2 (Bedding et al.,

Table 3.2: Observed oscillation frequencies in β Hyi (in μHz) resulting from the revised analysis, listed in ascending radial order within each column. The rows are in ascending l, and each row includes frequencies within $\Delta\nu$-sized-bits of the frequency spectrum. "..." is used for the modes whose S/N was too low for a clear extraction.

$l = 0$	$l = 1$	$l = 2$	$l = 3$
660.74 ± 2.43	...	...	...
716.68 ± 3.00	...	711.24 ± 2.13	...
774.79 ± 2.20	802.74 ± 1.69	769.97 ± 0.99	791.66 ± 1.35
831.86 ± 2.43	857.32 ± 0.86	825.86 ± 1.18	...
889.15 ± 1.23	912.91 ± 0.86	883.35 ± 0.89	...
946.11 ± 0.91	959.98 ± 0.89	939.97 ± 0.97	...
...	987.08 ± 0.87	...	...
1004.32 ± 0.86	1032.99 ± 0.86	999.40 ± 0.91	...
1061.66 ± 0.95	1089.87 ± 0.88	1057.00 ± 0.86	...
1118.67 ± 0.88	1147.35 ± 0.91	1115.20 ± 1.06	...
1177.76 ± 0.97	1203.54 ± 1.01	1172.98 ± 0.86	1198.16 ± 1.23
1235.31 ± 1.09	...	...	...
...	1320.42 ± 0.94	...	...
...	1378.92 ± 1.39	...	...

private communication). These were estimated through a new analysis of the 2005 dual-site observations (Bedding et al. 2007) using revised weights that were adjusted using a new method that minimises the sidelobes (Kjeldsen, H. et al., in preparation). This method is described by Bedding et al. (2010), who applied it to multi-site observations of Procyon (see also Arentoft et al. 2009). In the same way as done for Procyon, oscillation frequencies from the time series of β Hyi were extracted using the standard procedure of iterative sine-wave fitting. The finite mode lifetime causes many modes to be split into two or more peaks which, coupled with the presence of mode bumping, meant that deciding on a final list of mode frequencies with correct l identifications was somewhat subjective. The same approach as described by Bedding et al. (2010) was followed, which involved using the ridge centroids as a guide and averaging multiple peaks into a single value. The remaining unidentified peaks in the power spectrum are listed in Table 3.3.

3.6.1.3 Modelling β Hyi

To compute the evolutionary models we used the ASTEC code. The following assumptions were made: spherical symmetry, no rotation, no magnetic field and no mass loss. The input

Table 3.3: Unidentified observed peaks with S/N ≥ 3.5.

ν (μHz)		
753.12 ± 1.57	1013.42 ± 1.50	1130.36 ± 1.30
828.70 ± 1.83	1025.80 ± 1.68	1134.32 ± 1.63
845.02 ± 1.61	1037.90 ± 1.63	1167.62 ± 1.10
868.60 ± 1.13	1065.12 ± 1.59	1256.78 ± 1.60
911.88 ± 1.76	1070.00 ± 1.43	1383.20 ± 1.75
1010.20 ± 1.91	1084.20 ± 1.57	1462.62 ± 1.92

physics considered in the ASTEC code is described in Section 3.2. For the atmospheric structure, we assumed an atmospheric temperature versus optical depth relation which is a fit to the quiet-sun relation of Vernazza et al. (1976). Both Di Mauro et al. (2003) and Fernandes & Monteiro (2003) found that models at the position of β Hyi in the HR diagram are not affected by convective overshooting, so we decided, for this work, not to consider it in our models.

We calculated two grids of evolutionary tracks, Grids I and II, with the input parameters shown in Table 3.4. In Grid II we included diffusion and gravitational settling of helium. For each grid, we took those models whose parameters were within the 3-σ uncertainties derived from the observations of β Hyi, and computed the corresponding oscillation frequencies with ADIPLS. Having the frequencies, we calculated, for each model, the r and a values, following Kjeldsen et al. (2008), using $b = 4.90$ and $\nu_0 = 1000\,\mu$Hz.

We followed the two methods mentioned in Section 3.5 to choose the model that best fits β Hyi. In the case of *method 2*, to calculate the χ^2, as defined in Eq. (3.5.6), we used all the observed and computed $l = 0, 1$, and 2 frequencies.

Table 3.4: Parameters used to compute the evolutionary tracks for β Hyi. $M/M_\odot$ is the mass in solar units, Z/X is the initial ratio of heavy elements to hydrogen abundances, and Y the helium abundance.

Parameter	Grid I	Grid II
$M/M_\odot$	1.00 - 1.18 (with steps of 0.02)	1.00 - 1.18 (with steps of 0.02)
Z/X	0.010 - 0.030 (with steps of 0.004)	0.010 - 0.030 (with steps of 0.004)
Y	0.24 - 0.30 (with steps of 0.02)	0.24 - 0.30 (with steps of 0.02)
Mixing length parameter ($\alpha_{\rm ML}$)	1.4 - 2.0 (with steps of 0.2)	1.4 - 2.0 (with steps of 0.2)
Diffusion & gravitational settling	None	He

3.6.1.4 Results, Discussion and Conclusions

The parameters of the best models found for Grids I and II are shown in Table 3.5. Figures 3.3

Table 3.5: The parameters of the best models found for Grid I (no diffusion) and II (He settling and diffusion), for each of the two methods. See text for details on the methods. The mass, M, luminosity, L, and radius, R, are expressed in solar units. $T_{\rm eff}$ is the effective temperature, Y and Z are the initial helium and heavy-element abundances, [Fe/H] is the metallicity at the surface, and $\alpha_{\rm ML}$ is the mixing-length parameter. Also r and a are factors used to compute the correction term, $\Delta\nu_{n0b}$ and $\Delta\nu_{n0a}$ are, respectively, the large frequency separation before and after applying the surface correction to the model $l = 0$ modes. The values of χ^2 are those calculated after correcting the frequencies for the near-surface effects.

	Grid I		Grid II	
Parameter	*Method 1*	*Method 2*	*Method 1*	*Method 2*
$M/\mathrm{M}_\odot$	1.16	1.04	1.04	1.04
$R/\mathrm{R}_\odot$	1.832	1.785	1.790	1.786
$L/\mathrm{L}_\odot$	3.433	3.485	3.432	3.338
$T_{\rm eff}$ (K)	5810	5908	5877	5843
Age (Gyr)	4.705	6.114	7.390	7.297
Z	0.0204	0.0124	0.0075	0.0075
Y	0.30	0.30	0.24	0.24
[Fe/H]	0.088	-0.133	-0.416	-0.424
$\alpha_{\rm ML}$	1.4	1.8	2.0	1.8
r	1.0000	0.9995	1.0000	1.0009
a (μHz)	-4.80	-3.14	-2.43	-3.11
$\Delta\nu_{n0b}$ (μHz)	58.977	58.488	58.243	58.400
$\Delta\nu_{n0a}$(μHz)	57.678	57.652	57.600	57.577
χ^2	19.086	1.183	26.226	2.642

and 3.4 show the échelle diagrams for β Hyi. In these figures the observed frequencies of β Hyi are compared with the theoretical frequencies of the best models from Grid I (upper panel) and from Grid II (lower panel), both before (left plot) and after (right plot), applying the near-surface corrections. The model frequencies are represented by open symbols and the observed frequencies (cf. Table 3.2) by solid symbols, while the asterisks represent the unidentified peaks (cf. Table 3.3), which may correspond to genuine modes, sidelobes, or noise peaks. The relative sizes of the open symbols reflect the expected mode amplitudes (Christensen-Dalsgaard et al. 1995). The so-called mixed modes reveal themselves in the échelle diagrams, breaking the regularity of the ridges. The models predict mixed modes with all nonradial degrees, however mostly with too small amplitudes to be observed. On

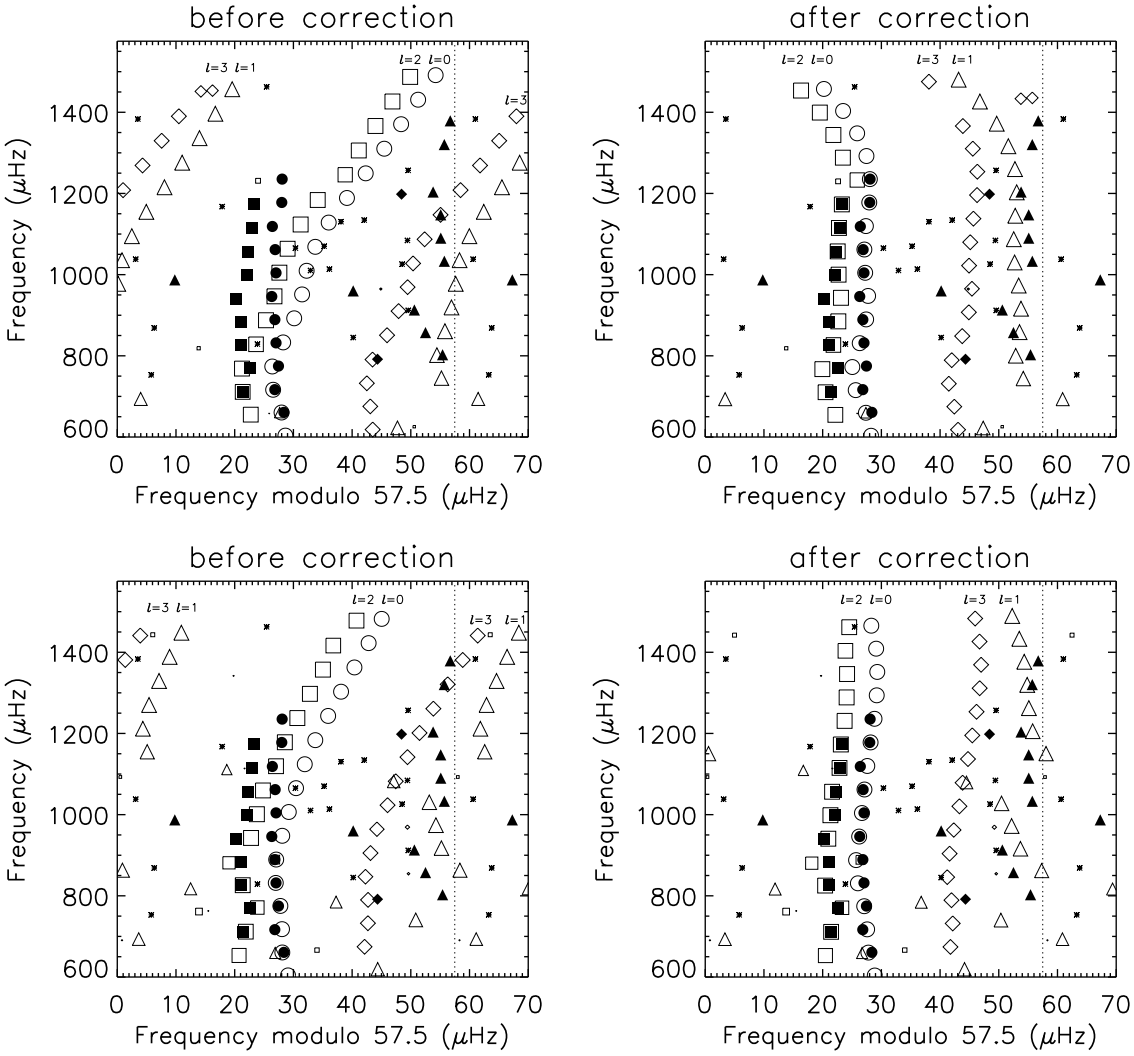

Figure 3.3: Échelle diagrams for β Hyi, with a frequency separation of $\langle\Delta\nu\rangle = 57.5\,\mu$Hz, before (left plot) and after (right plot) application of the near-surface corrections to the model frequencies. Shown are the frequencies of the selected models using *method 1*, when including no diffusion (upper panel) and diffusion (lower panel). In *method 1*, the best model was selected using the radial ($l = 0$) modes alone (see the text for details). The solid symbols show observed frequencies (Table 3.2), asterisks the unidentified peaks (Table 3.3), and the open symbols the model frequencies. Circles are used for $l = 0$ modes, triangles for $l = 1$, squares for $l = 2$ and diamonds for $l = 3$. Open symbols are scaled to represent the relative amplitudes of the modes as predicted by the models.

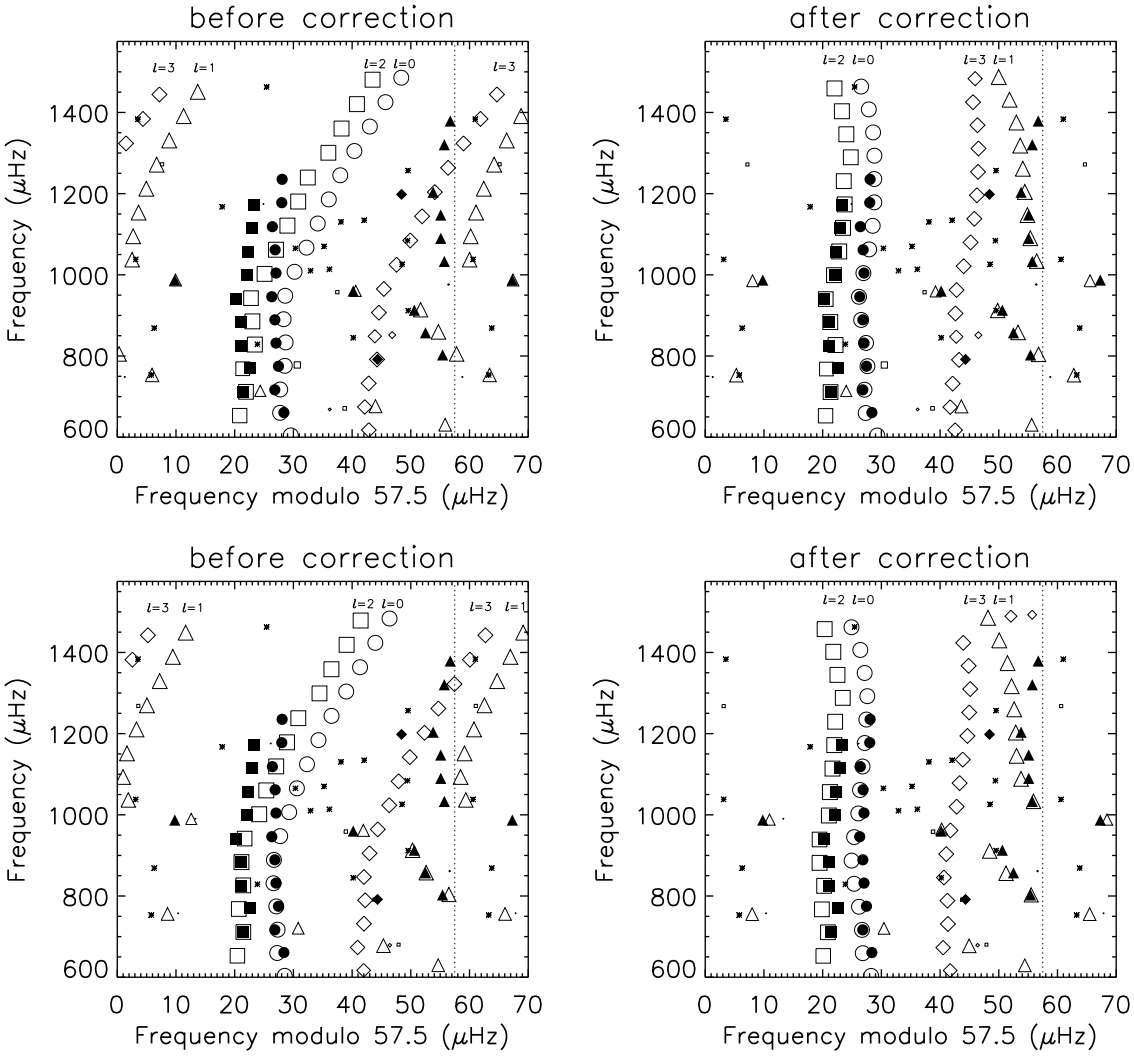

Figure 3.4: The same as Figure 3.3 but for the best models without (upper panel) and with (lower panel) diffusion, selected using *method 2*, which takes into account the observed and identified modes with all degrees available.

the other hand, some of the observed modes match well the mixed modes with $l = 1$ (see, e.g., the right panels of Figure 3.4). If we inspect Figs. 3.3 and 3.4, it is clear that the agreement between the observed and model frequencies is much better when *method 2* is used (Figure 3.4). This is due to the fact that in this method all the available seismic constraints were involved in selecting the best model.

It is seen from Table 3.5 that the model that has the r value closest to unity does not produce the lowest χ^2 value. The model with the lowest χ^2 still has an r satisfactorily close to unity. So, in addition to finding a model that represents the stellar interior reasonably, *method 2* makes sure that all the available seismic constraints are simultaneously reproduced and so the fit, and hence the accuracy of the model, is improved substantially. This shows the importance of using the individual modes when constraining the range of models to represent the observed star. Mixed modes, in particular, put strong constraints to the model properties, especially on the evolutionary stage. For instance, we can see from the right panels of Figure 3.3 that the two models resulting from *method 1* have the two highest χ^2 values due to failing to match particularly the observed $l = 1$ mixed modes. In the upper right panel, the model is too massive and it matches the rest of the seismic constraints before it is sufficiently evolved to have mixed modes, whereas the model in the lower right panel does have mixed modes, although the predicted mixed modes do not match those observed.

In general, we found that the empirical surface corrections proposed by Kjeldsen et al. (2008) work very well for β Hyi as seen from Figs. 3.3 and 3.4, although there is still room for improvement, in particular for high-frequency modes of $l = 1$. The reason for the suboptimal agreement for those modes is that the correction term is determined using only the $l = 0$ observed modes, whose frequencies span a smaller range than those of the $l = 1$ modes. Thus, radial modes with higher frequencies need to be detected in order to improve the agreement for the higher frequency $l = 1$ modes. Note that the change in the large frequency separation of the models after applying the near-surface correction is around 0.8 μHz, which is larger than the given uncertainty of the observed large separation. This should be taken into account when modelling through a pipeline analysis that uses the large separation as input. It is encouraging to see that we can observe $l = 3$ modes, and that some of the unidentified modes are also close to the model frequencies, namely 753.1 μHz ($l = 1$?) and 1462.6 μHz ($l = 0$?).

Even though the best model seems to be the one without diffusion, we do expect that within a star diffusion occurs. The two selected models, the ones with and without diffusion, resulting from the *method 2* are in fact compatible and both could be further fine-tuned.

Our best models give M=1.04 $M_\odot$ and an age of 6.1 – 7.3 Gyr for β Hyi, depending on the

inclusion of gravitational settling and diffusion of helium. In both cases, the radius is found to be $R \sim 1.785\,R_\odot$, which is in good agreement with the one determined by interferometry, $R = 1.809 \pm 0.015\,R_\odot$. However, there are other models fitting the data similarly well. We used the parameters of those models (with $\chi^2 < 10$) to determine the internal error regarding our analysis. We calculated the mean value, and the uncertainties were taken as the standard deviation. We found $M = 1.08 \pm 0.03\,M_\odot$, age $= 6.40 \pm 0.56$ Gyr, and $R = 1.811 \pm 0.020\,R_\odot$. These results are also consistent with the results of Fernandes & Monteiro (2003), who derived, $M = 1.10^{+0.04}_{-0.07}\,M_\odot$ and $M = 1.09 \pm 0.22\,M_\odot$, through the HR diagram analysis and $\Delta\nu_{n0}$, respectively, and a stellar age between 6.4 and 7.1 Gyr.

3.6.2 KIC 10273246

As a member of the *Kepler* Asteroseismic Science Consortium (KASC), I am involved in the Working Group # 1 (WG1) - Solar-like p-mode Oscillations. There are several workpackages within WG1 and each package is dedicated to a particular topic. The members of WG1 can work in one or more workpackages. The workpackage structure ensures coordinated collaboration between the members and, at the same time, speeds up the analysis. Each workpackage has a lead, or leads that work in close collaboration with the liason(s). The lead is responsible for the progress of the work assigned to each workpackage, while the liason is responsible for the coordination between the workpackages if overlap between them exists. Within WG1 besides my work on the convective cores that I will describe in Chapter 4, I am currently co-leading a workpackage on the modelling of 5 *Kepler* targets, namely KIC 11395018, KIC 10920273, KIC 11234888, KIC 10339342, and KIC 10273246. These stars show clear solar-like oscillations and were chosen to be continuously monitored by the *Kepler* satellite, in order to test and validate the time series photometry (Gilliland et al. 2010). They have been observed at short cadence for at least eight months (from Quarter 0 to 4) since the beginning of *Kepler* science operations on May 2, 2009. It is the first time that we have more than eight months of continuous asteroseismic data for five solar-like stars. I was assigned to lead a paper on the detailed modelling of one of these five stars, namely KIC 10273246. A first paper on the group of stars studied in this workpackage was already published by Creevey et al. (2012). The results published in this paper were used as constraints to a more detailed modelling on the five stars, in particular KIC 10273246 which I will describe in what follows.

KIC 10273246, also known as Mulder within KASC, is a star of spectral type F9IV-V (Creevey et al. 2012). It is relatively faint, with a *Kepler* magnitude (K_p) of 10.9[22]. Note that

[22] http://archive.stsci.edu/kepler/kepler_fov/search.php

Table 3.6: The oscillation frequencies of KIC 10273246 published by Campante et al. (2011).

l	Frequency (μ Hz)	Uncertainty (μ Hz)
0	737.90	0.30
0	785.40	0.20
0	833.90	0.20
0	883.50	0.20
0	932.70	0.50
0	981.10	0.30
0	1030.70	0.40
0	1079.30	0.20
1	622.80	0.20
1	661.90	0.503
1	695.75[a]	0.27
1	724.70	0.20
1	764.30	0.30
1	809.80	0.20
1	857.30	0.20
1	905.60	0.30
1	950.00	0.30
1	1008.60	0.40
1	1056.30	0.20
1	1103.30	0.40
2	688.50	0.70
2	734.80	0.60
2	779.50	0.40
2	830.30	0.40
2	880.60	0.50
2	927.50	0.40
2	977.60	0.40
2	1025.30	1.30
2	1073.70	0.20
2	1122.70	0.40

[a] $l = 1$ mixed mode

the apparent magnitude target range for the detection of solar-like oscillations with *Kepler* spans $K_p \approx 6.5$ to $K_p \approx 12.5$ (e.g., Chaplin et al. 2011). Although KIC 10273246 was chosen to be continuously monitored by the *Kepler* satellite, it has not been observed in Quarters 6 and 7. However, it has been put in the KASC target list again from Quarter 8. The first seven month of short-cadence time series photometry were analysed by Campante et al. (2011) who identified a total of 30 p-mode oscillations of degree $l = 0, 1, 2$ for this star, spanning at least eight radial orders (Table 3.6). Moreover, they also identified two avoided crossings in the $l = 1$ ridge, indicating that this star is evolved. Estimations of the large frequency separation, $<\Delta\nu>$, frequency at maximum power, $\nu_{\rm max}$, and small frequency separation, $<\delta\nu_{n0}>$, for KIC 10273246 are shown in Table 3.7 as given by Campante et al. (2011). Using their published frequencies new estimations for $<\Delta\nu>$, $\nu_{\rm max}$, and $<\delta\nu_{n0}>$ were

Table 3.7: Estimates of the observed seismic parameters, the mean large frequency separation, $<\Delta\nu>$, the frequency of maximum amplitude, $\nu_{\rm max}$, and the mean small frequency separation, $<\delta\nu_{n0}>$ for KIC 10273246 given by Campante et al. (2011) (1st row) and given by Creevey et al. (2012) (2nd row). Also shown is the range of frequencies where the mean was performed.

	$<\Delta\nu>$ (μHz)	range (μHz)	$\nu_{\rm max}$ (μHz)	$<\delta\nu_{n0}>$ (μHz)
Campante et al. (2011)	48.2 ± 0.5	[537,1140]	839 ± 51	5.6 ± 1.2
Creevey et al. (2012)	48.89 ± 0.09	[737,1080]	838 ± 50	4.40 ± 0.44

made as described in detail in Creevey et al. (2012). The values derived in that paper are also shown in Table 3.7 and are in agreement with those given in Campante et al. (2011).

The *Kepler* Input Catalog[23] (KIC; e.g., Latham et al. 2005; Batalha et al. 2010; Brown et al. 2011; Pinsonneault et al. 2011) provides physical data for over 15 million stars (down to a magnitude limit of 19) present within and around the *Kepler* field of view. All the KASC targets have been selected from this catalog. Although the catalog provides estimates for the $T_{\rm eff}$, log g and [Fe/H], the stated precisions of these parameters are 200 K in Teff[24], and 0.5 dex in log g and [Fe/H]. These precisions are too low for an asteroseismic modelling (see, e.g., Molenda-Żakowicz et al. 2011), so tighter constraints are needed. Fortunately, for four of the five stars within our workpackage, including KIC 10273246, atmospheric parameters were derived from spectra acquired with the FIES[25] instrument at the Nordic Optical Telescope (NOT). These data were analysed by five groups independently and their results are shown in Table 3.8 for KIC 10273246. The relatively large errors on the derived

[23] https://archive.stsci.edu/kepler/kic.html

[24] Note that Pinsonneault et al. (2011) revised the initial temperatures provided by KIC and new values and uncertainties for $T_{\rm eff}$ are given.

[25] http://www.not.iac.es/instruments/fies/

Table 3.8: The effective temperature, $T_{\rm eff}$, logarithm of the surface gravity, log g, metallicity, [Fe/H], microturbulence, $\xi_{\rm t}$, and the projected rotational velocity, $v \sin i$, derived for KIC 10273246 from the analysis by five different teams of NOT spectra (Creevey et al. 2012).

Group ID	$T_{\rm eff}$ (K)	log g (dex)	[Fe/H] (dex)	$\xi_{\rm t}$ (km s^{-1})	$v \sin i$ (km s^{-1})
SOU	6165 ± 77	4.01 ± 0.11	−0.04 ± 0.06	1.48 ± 0.05	-
ROTFIT	5933 ± 205	4.07 ± 0.10	−0.21 ± 0.08	-	3.2 ± 1.5
VWA	6050 ± 100	3.80 ± 0.11	−0.18 ± 0.04	1.50 ± 0.10	-
BIA	6200 ± 60	4.00 ± 0.20	−0.04 ± 0.07	1.50 ± 0.20	-
NIEM	6200 ± 100	3.90 ± 0.20	−0.18 ± 0.05	0.50 ± 0.40	-

parameters and the discrepancies between the five different groups on each parameter may be due, in part, to the low S/N of the NOT spectra (S/N = 90 in the wavelength region of 6069-6076 Å) with a medium resolution ($\mathcal{R}$ = 46 000). Combining the atmospheric parameters provided by one of the five groups, namely VWA, with the observed seismic quantities $<\Delta\nu>$ and $\nu_{\rm max}$ (2nd row of Table 3.7) a grid-based analysis was used to determine the global stellar properties, such as mass (M), radius (R), and age (τ), of the stars under study. Five different pipelines based on stellar evolution and structure models provided values for these parameters. For the detailed modelling, we adopted the results from one of the pipelines (see Table 3.9 for KIC 10273246) and the results from the other pipelines were considered as a test for systematic errors resulting mostly from different modelling prescriptions of particular aspects of the physics (see Table 3.10 for KIC 10273246).

In Creevey et al. (2012) the impact on the derived stellar parameters, in particular on the derived age, of considering $<\delta\nu_{n0}>$ as an observable constraint together with $<\Delta\nu>$ and $\nu_{\rm max}$ was also investigated. This was found not to be important for KIC 10273246, which can be understood by the fact that this star is evolved (White et al. 2011). However, the constraint $<\delta\nu_{n0}>$ is of great importance for middle main-sequence stars, such as the Sun.

The value of the luminosity of the best model found in Creevey et al. (2012) for KIC 10273246, together with the photometric magnitudes published in the literature, was used to estimate the distance to the star. Moreover, an upper estimation of the rotational period, P_{ROT}, and the inclination angle i for KIC 10273246 based on its observed $v \sin i$ and the model radius were also derived in the paper (Table 3.9).

Starting from the results described above, we then moved to the detailed modelling of the star. One of the goals of this modelling is to test whether the empirical formulation for the surface correction is satisfactory for this relatively hot star.

Table 3.9: The stellar properties for KIC 10273246 obtained with the SEEK pipeline that best fitted the seismic data, $<\Delta\nu>$ and $\nu_{\rm max}$ (2nd row of Table 3.7), and the non-seismic data, $T_{\rm eff}$, log g, and [Fe/H] from VWA (Creevey et al. 2012). ρ stands for the density, R for the radius, M for the mass, τ for the age, L for the luminosity, i for the inclination angle, P_{ROT} for the rotational period and d for the distance of the star.

Parameter	KIC 10273246
$^{a}<\rho>_{\nu}$ (Kg m^{-3})	185 ± 1
$^{b}<\rho>_{\rm MR}$ (Kg m^{-3})	189 ± 2
$^{a}\log g_{\nu}$ (dex)	3.88 ± 0.03
$^{b}\log g_{\rm MR}$ (dex)	3.88 ± 0.02
$R(\rm R_{\odot})$	2.11 ± 0.05
$M(\rm M_{\odot})$	1.26 ± 0.10
τ (Gyr)	3.7 ± 0.7
$^{c}\tau_{<\delta\nu>}$ (Gyr)	3.7 ± 0.6
$L(\rm L_{\odot})$	5.3 ± 1.1
$T_{\rm eff,model}$ (K)	6047
$i(^{\circ})$	44^{+46}_{-23}
P_{ROTmax} (days)	64
$^{d}P_{ROTest}$ (days)	23
d (pc)	366^{+36}_{-40}

^{a,b} Subscripts ν and MR indicate that the value was obtained directly from the data and from the models, respectively. $^{c}\tau_{<\delta\nu>}$ is when $<\delta\nu_{n0}>$ is included as an observational constraint. See text for details. ^{d} P_{ROTest} as reported by Campante et al. (2011).

Table 3.10: Estimates of the systematic errors for log g (CGS units), R and M in solar units, and τ in Gyr for KIC 10273246. The % values are given in parenthesis (Creevey et al. 2012).

	KIC 10273246
$\sigma_{\log g,grid}$	0.05
$\sigma_{R,grid}$	0.22 (11)
$\sigma_{M,grid}$	0.43 (34)
$\sigma_{\tau,grid}$	1.7 (38)
$\sigma_{R,spec}$	0.08 (4)
$\sigma_{M,spec}$	0.16 (13)

In order to proceed with this work, all members of the WG1 were invited to contribute to the modelling of KIC 10273246. They were asked to find the best model for KIC 10273246 using its seismic (large separations, small separations, and the individual frequencies, corrected, or not, for the near-surface effects) and non-seismic data. The results from Creevey et al. (2012) were used as a starting point for the modelling by the different members, i.e. a starting point from which to refine their grids. Those involved were asked to search for the best model within an as large as possible parameter space such as to explore the possible solutions with different combinations of metallicity, mixing length and overshooting parameters. They were also invited to consider different physics such as diffusion and rotation. Six different teams besides myself replied favourably. So a total of seven teams performed the detailed modelling of KIC 10273246. In what follows I will mention the observational constraints used to perform the modelling and then I will describe in detail my part of the modelling. Finally, I will summarize the results from the other teams and conclude.

3.6.2.1 Observational constraints

As *seismic constraints* we considered the individual oscillation frequencies and the values for $<\Delta\nu>$, $<\delta\nu_{n0}>$ and $\nu_{\rm max}$ given by Campante et al. (2011) (see Table 3.6 and Table 3.7). In Figure 3.5 the échelle diagram for KIC 10273246 is shown, based on the observed oscillation frequencies.

In relation to the *non-seismic constraints*, namely the effective temperature, $T_{\rm eff}$, logarithm of the surface gravity, $\log g$, and metallicity [Fe/H], we adopted the values from the group 'NIEM' (see Table 3.8). We chose this group because it is the one that gives the values for the non-seismic parameters closest to the mean. The mean was computed for each parameter $T_{\rm eff}$, $\log g$, and [Fe/H], by considering the values from the five groups in Table 3.8. We asked all modelling teams to consider an uncertainty three times larger than the uncertainty given by 'NIEM', for each parameter, such as to reflect the dispersion of the values found by the observational teams. The reason to adopt one set of atmospheric constraints rather than taking the mean over the values given by all the five groups was because we wanted to make sure that consistency existed between the different observables. Figure 3.6 shows the positions of KIC 10273246 in the HR diagram with some evolutionary tracks computed with ASTEC without considering diffusion, for particular values of the input parameters, namely $Z = 0.01016$, $Y = 0.264$, $Z/X = 0.0140$, $\alpha_{\rm ML} = 2.0$, and $\alpha_{OV} = 0$, and with different masses, for illustration.

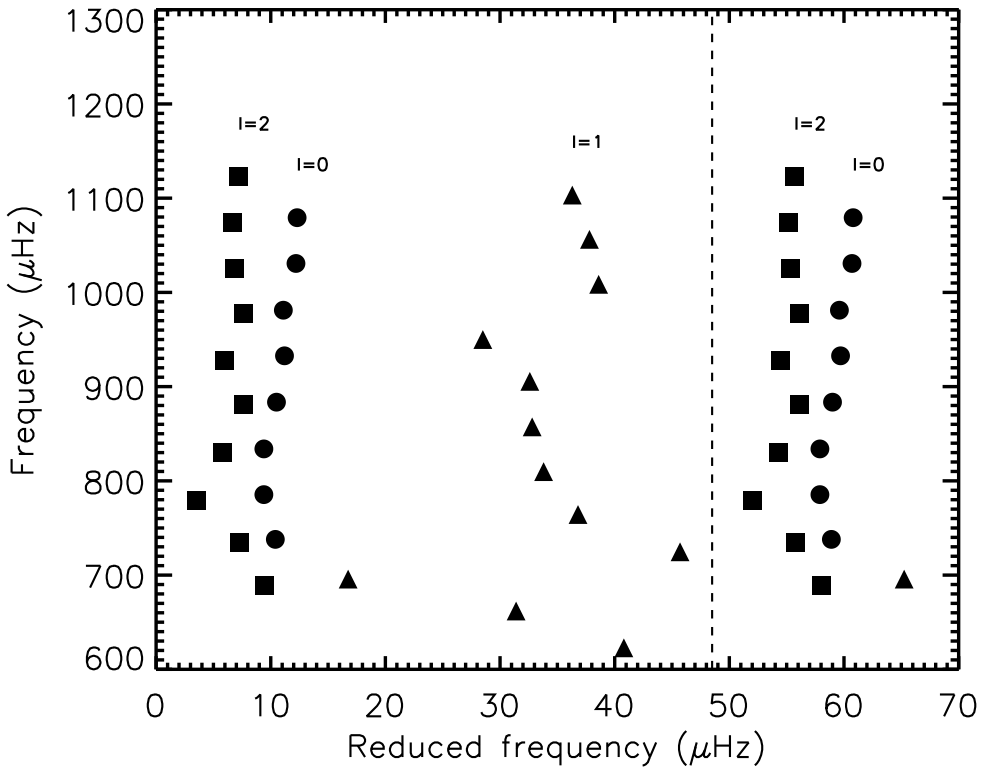

Figure 3.5: The échelle diagram with the observed frequencies of KIC 10273246 obtained by the *Kepler* satellite (Campante et al. 2011), plotted with $\nu_0 = 738\,\mu$Hz and $\langle\Delta\nu\rangle = 48.5\,\mu$Hz. Circles, triangles and squares are used for modes of degree $l = 0$, 1 and 2, respectively.

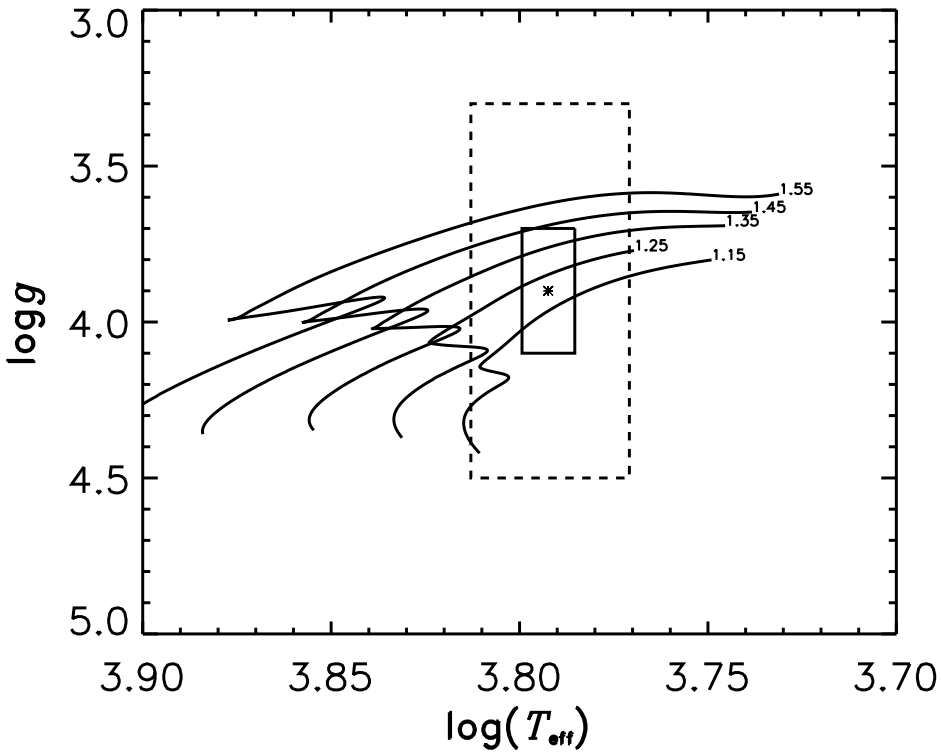

Figure 3.6: The position of KIC 10273246 in the HR diagram. The solid line box represents the 1-σ uncertainty, while the dashed box represents the 3-σ uncertainty on $\log g$ and $\log(T_{\rm eff})$, given by the group 'NIEM' (see Table 3.8). Some evolutionary tracks computed without diffusion and for particular values of the input parameters and with different masses are shown, with the masses at the end of each evolutionary track, in units of solar mass.

3.6.2.2 Results from my modelling

To find the model that best fits the observational constraints of KIC 10273246 mentioned above we used the *method 2* described in Section 3.5. We computed two grids of evolutionary models with the ASTEC code considering the same physics that was described in Section 3.2. The atmospheric structure was the same as in the modelling of β Hyi. The input parameters, and their range, used in the computation of the two grids are shown in Table 3.11. The difference between them resides in the value of Y. In Grid I, Y is computed

Table 3.11: Input parameters that I used to compute the evolutionary tracks of the two grids for KIC 10273246. $M/\mathrm{M}_\odot$ is the mass in solar units, Z/X is the initial ratio of heavy elements to hydrogen abundances, and Y the helium abundance.

Parameter	Grid I	Grid II
$M/\mathrm{M}_\odot$	1.10 - 1.60 (with steps of 0.05)	1.10 - 1.60 (with steps of 0.05)
Z/X	0.010 - 0.022 (with steps of 0.004)	0.010 - 0.022 (with steps of 0.004)
Y	-	0.24
Mixing length parameter (α_{ML})	1.2 - 2.2 (with steps of 0.2)	1.2 - 2.2 (with steps of 0.2)
α_{OV}	0	0
Diffusion & gravitational settling	None	None

from the relation

$$Y = Y_p + Z\,\frac{dY}{dZ}, \tag{3.6.2}$$

where Y_p is the abundance of helium produced during primordial nucleosynthesis and $\frac{dY}{dZ}$ is the helium to metal enrichment ratio. When using this relation we assume that massive stars synthesize both helium and heavy elements and supply them to the interstellar medium, and also assume this equation to hold at all places and times. Considering $\mathrm{d}Y/\mathrm{d}Z = 2$ (see, e.g. Casagrande 2007) and using the the solar values of $(Z/X)_\odot = 0.0245$ (Grevesse & Noels 1993) and $Y_\odot = 0.278$ (Serenelli & Basu 2010) we found $Y_p = 0.2435$. Using $\mathrm{d}Y/\mathrm{d}Z = 2$ and $Y_p = 0.2435$, and fixing Z, we derive Y.

In Grid II, we considered the Y and Z values to change independently. Thus, Grid II was basically constructed as a complement to Grid I.

For the models that lie inside the 3-σ error box of the star's position in the HR diagram we computed their oscillation frequencies with the ADIPLS code, corrected them for the near-surface effects and then compared them to the observed frequencies. The parameters of the best model found, i.e. the model which parameters minimized the χ^2_{seis} (cf. Eq. (3.5.6)), are shown in Table 3.12. In this equation we considered $\nu_0 = 839\,\mu$Hz and $b = 4.90$. The

Table 3.12: The parameters of the best model found for KIC 10273246 from my analysis. The mass, M, luminosity, L, and radius, R, are expressed in solar units. $T_{\rm eff}$ is the effective temperature, Y and Z are the initial helium and heavy-element abundances, [Fe/H] is the metallicity at the surface, and $\alpha_{\rm ML}$ is the mixing-length parameter. Also r and a are factors used to compute the correction term, $\Delta\nu_{0b}$ and $\Delta\nu_{0a}$ are, respectively, the large frequency separation before and after applying the surface correction to the model $l = 0$ modes. The value of $\chi^2_{\rm seis}$ are those calculated after correcting the frequencies for the near-surface effects.

Parameter	KIC 10273246
$M/\mathrm{M}_\odot$	1.25
$R/\mathrm{R}_\odot$	2.13
$L/\mathrm{L}_\odot$	6.34
$T_{\rm eff}$ (K)	6281
Age (Gyr)	3.6
Z	0.01016
Y	0.264
[Fe/H]	-0.243
$\alpha_{\rm ML}$	2.0
r	1.0014
a (μHz)	-1.36
$\Delta\nu_{0b}$ (μHz)	49.47
$\Delta\nu_{0a}$(μHz)	48.90
$\chi^2_{\rm seis}$	37

échelle diagram with the frequencies of the best model (open symbols) overplotted to the observed frequencies (filled symbols) is shown in Figure 3.7, before (left panel) and after (right panel) applying the near-surface corrections to the model frequencies.

3.6.2.3 Results from the other six teams

In what follows I will briefly describe the methods used by the other six teams, as well as their results.

`Team1`

Team1 used the ASTEC code to compute grids of models within the 3-σ uncertainty of the non-seismic constraints and computed their oscillation frequencies with the ADIPLS code. The search for the best model was performed by a 2-step process, refining the first grid in

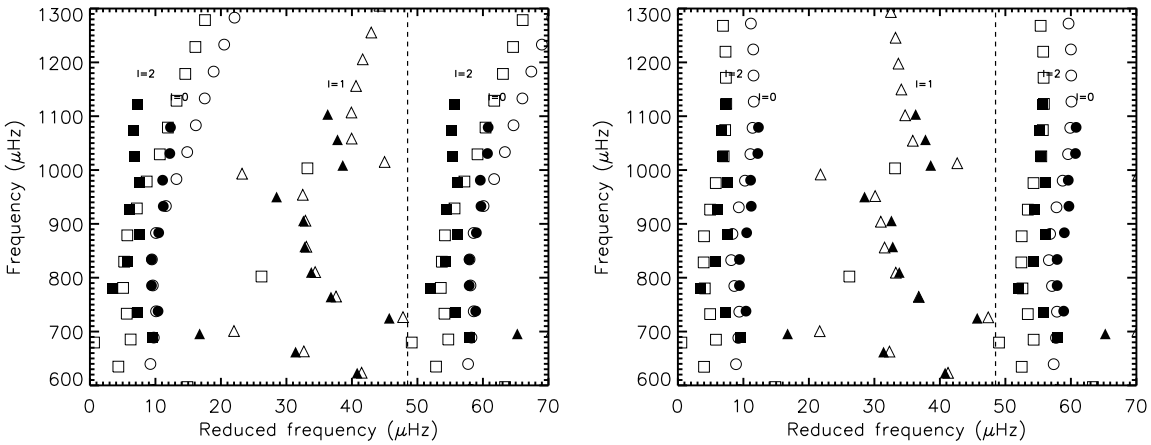

Figure 3.7: Échelle diagrams for KIC 10273246, with a frequency separation of $\Delta\nu = 48.5\,\mu$Hz, before (left plot) and after (right plot) application of the near-surface corrections to the model frequencies. Shown are the frequencies of the best model found in my analysis (open symbols) and the observed frequencies (solid symbols) (c.f. Table 3.6). Circles are used for $l = 0$ modes, triangles for $l = 1$ and squares for $l = 2$.

the second step guided by the $\chi^2_{\rm seis}$ values from the first grid, whith $\chi^2_{\rm seis}$ defined as

$$\chi^2 = \frac{1}{N}\sum_{n,l}\left(\frac{\nu_{\rm ref}(n,l) + \left(\frac{1}{Q_{nl}}\right)\left(\frac{a}{r}\right)\left[\frac{\nu_{\rm ref}(n,l)}{\nu_0}\right]^b - \nu_{\rm obs}(n,l)}{\sigma(\nu_{\rm obs}(n,l))}\right)^2 . \qquad (3.6.3)$$

The input physics used in the ASTEC code was the same as that used in the modelling of KIC 11026764, that is described in Metcalfe et al. (2010), labeled as "Model A". The input parameters for the two grids are shown in Table 3.13. The properties of the best model

Table 3.13: Input parameters used by Team1 to compute the models of the two grids for KIC 10273246. $M/{\rm M}_\odot$ is the mass in solar units, Z/X is the initial ratio of heavy elements to hydrogen abundances, and Y the helium abundance. $\alpha_{\rm ML}$ and $\alpha_{\rm OV}$ are the mixing length parameter and the overshooting, respectively.

Parameter	Grid I	Grid II
$M/{\rm M}_\odot$	1.15 - 1.55 (with steps of 0.05)	1.28 - 1.32 (with steps of 0.02)
Z/X	0.01 - 0.03 (with steps of 0.01)	0.010 - 0.016 (with steps of 0.002)
Y	-	0.24 - 0.032 (with steps of 0.02)
$\alpha_{\rm ML}$	1.8	1.8
$\alpha_{\rm OV}$	0	0
Diffusion & gravitational settling	None	None

found by Team1 are shown in Table 3.18. **Team2** Team2 used the Geneva stellar evolution

code (Eggenberger et al. 2008) to compute a grid of rotating models with an initial velocity of 50 km/s on the ZAMS. The input physics used to compute the models are described in Metcalfe et al. (2010), in Section "Model B". The input parameters given to the code are shown in Table 3.14. The oscillation frequencies of the models of the grid were computed

Table 3.14: Input parameters used by Team2 to compute the models. $M/M_\odot$ is the mass in solar units, Z/X is the initial ratio of heavy elements to hydrogen abundances, and Y the helium abundance. α_{ML} and α_{OV} are the mixing length parameter and the overshooting parameter, respectively.

Parameter	Grid
$M/M_\odot$	1.16 - 1.34 (with steps of 0.03)
Z/X	0.010 - 0.022 (with steps of 0.006)
Y	0.25 - 0.29 (with steps of 0.02)
α_{ML}	0.7998[1]
α_{OV}	0.1
Diffusion & gravitational settling	He & heavy elements

[1] Solar calibrated model

with the ADIPLS code. These frequencies were corrected for the near-surface effects in the way described by Kjeldsen et al. (2008). The search of the best model was done by minimizing the χ^2_{seis} (c.f. Eq. (3.6.3)), although they did not scale the surface contribution for the mixed modes by the mode inertia. After finding the best model, they refined their grid around the solution using smaller time steps. The parameters of the best model found from this team are shown in Table 3.18.

Team3

This team used AMP to model KIC 10273246. AMP is a web-based interface tied to a TeraGrid computing resource (Woitaszek et al. 2009) that uses the ASTEC and the ADIPLS codes together with a parallel genetic algorithm (GA; Metcalfe & Charbonneau 2003) to optimize the fit between the model output and the observational seismic and non-seismic constraints. GA optimizes four adjustable model parameters, namely the mass M, the mass fraction of metals Z, the initial helium mass fraction Y_0, and the mixing-length parameter α_{ML}, within a broad parameter space as shown in Table 3.15. The stellar age (t) is optimized internally during each model evaluation by matching the observed value of $\Delta\nu_{n0}$. A more detailed description of the method, as well as the input physics used in the ASTEC code, is given in Metcalfe et al. (2009). To evaluate the differences between each model and the observations, two χ^2 calculations are performed. One related to the non-seismic constraints

Table 3.15: Parameter space used by AMP. $M/M_\odot$ is the mass in solar units, Z/X is the initial ratio of heavy elements to hydrogen abundances, and Y the helium abundance. α_{ML} and α_{OV} are the mixing length parameter and the overshooting parameter, respectively.

Parameter	Parameter space
$M/M_\odot$	0.75 - 1.75 (with steps of 0.01)
Z	0.002 - 0.05 (with steps of 0.0005)
Y	0.22 - 0.32 (with steps of 0.001)
α_{ML}	1 - 3 (with steps of 0.02)
α_{OV}	0
Diffusion & gravitational settling	He settling

χ^2_{spec} and the other related to the seismic ones χ^2_{seis}. The former is defined as

$$\chi^2_{spec} = \frac{1}{N_s} \sum_{i=1}^{N_s} \left(\frac{P_{ref,i} - P_{obs,i}}{\sigma_{obs,i}} \right)^2 , \tag{3.6.4}$$

where $P_{obs,i}$ are the N_s observed non-seismic constraints, while $P_{ref,i}$ are the values of the corresponding observables from the reference model. The definition of χ^2_{seis} is the same as given in Eq. (3.5.2). They considered $b = 4.82$ rather than 4.90, which is the calibrated value obtained using the BISON data for the Sun (Chaplin et al. 1999). Note that AMP also applies the empirical correction suggested by Kjeldsen et al. (2008) to the model frequencies before comparing them to the observed ones. AMP minimizes the mean of these two χ^2 values. After finding the global minimum, AMP performs a local optimization method, which employs a modified Levenberg-Marquardt (LM) algorithm with Singular Value Decomposition (SVD) (see Metcalfe et al. 2009, for details).

The parameters of the best model found by AMP are shown in Table 3.18.

Team4

Team4 uses a slightly different method than the ones previously mentioned to find the best model. The method is described in Deheuvels & Michel (2011) and consists in finding the models that reproduce the first observed frequency of the avoided crossing. For KIC 10273246 this frequency occurs at $\sim$700 μHz. After finding the models that reproduce the first avoided crossing, a χ^2 minimization is performed to determine the stellar mass and age. The parameters used to compute the χ^2 are the following: T_{eff}, log g, [Fe/H] and the $l = 0, 1, 2$ frequencies. The stellar evolution code Cesam2k (Morel 1997) was used by Team4 to compute the evolutionary models. The parameter range used to compute the grid

is shown in Table 3.16. The oscillation frequencies were computed with the oscillation code

Table 3.16: Input parameters used by Team4 to compute the models. $M/M_\odot$ is the mass in solar units, Z/X is the initial ratio of heavy elements to hydrogen abundances, and Y the helium abundance. α_{CGM} and α_{OV} are the CGM parameter and the overshooting parameter, respectively.

Parameter	Grid
$M/M_\odot$	n/a*
Z/X	[0.011, 0.014, 0.016, 0.018, 0.023]
Y	0.24 - 0.28 (with steps of 0.01)
α_{CGM}	0.56 - 0.68 (with steps of 0.04)
α_{OV}	0.00 - 0.20 (with steps of 0.05)
Diffusion & gravitational settling	None

*Within the method proposed by Deheuvels & Michel (2011), for a given set of Z/X, Y, α_{CGM}, and α_{OV}, they are able to estimate the mass with good precision from the large frequency separation and the frequency of the mixed modes.

LOSC (Scuflaire et al. 2008). The model frequencies were corrected for the near-surface effects as given in Eq. (3.6.3). The b value used by Team4 was 4.25. This was found by searching for a solar model using the same conditions as the models for KIC 10273246, i.e. using the Cesam2K code and the CGM formalism for convection, to determine the solar value of the exponent b using the GOLF data (Gelly et al. 2002). Here, the CGM formalism involves a free parameter assumed to be some fraction α_{CGM} of the local pressure scale height H_p.

The parameters of the best model found by Team4 are shown in Table 3.18.

Team5

Team5 tried to find a model for KIC 10273246 mainly based on its oscillation properties such as the large frequency separation and the individual frequencies. The main difference between the method used by Team5 and the other teams was that this team computed model nonadiabatic oscillation frequencies rather than the adiabatic ones. Consequently, they did not need to apply the empirical surface correction to their computed frequencies, as for their solar models' $l = 0$ to $l = 2$ modes the nonadiabatic frequencies agree quite well with those observed. However, this agreement is not so good for very high frequencies of the Sun, namely for $\nu > 4000\,\mu$Hz and for l values of several hundred.

The evolutionary code used by Team5 to compute the models was the code from Iben (1963, 1965). All physics input has been updated since 1965. The opacities are OPAL tables from Iglesias & Rogers (1996), with the Grevesse & Noels (1993) solar mixture. The low-

temperature opacities are from Alexander and Ferguson (1995) (private communication) also using the Grevesse & Noels (1993) solar mixture. The equation of state is the SIREFF (discussed in Guzik & Swenson 1997). Diffusion is from the treatment of Burgers (1969) and diffuses many of the elements individually, including He, C, N, O, Mg, and the electron, as discussed in Cox et al. (1989). It was implemented in the Iben code by Iben & MacDonald (1985) for modelling white dwarfs, but after thermal and chemical, as well as gravitational diffusion, were added. Further discussion for the case of solar models is given by Guzik & Mussack (2010).

The nonadiabatic oscillation frequencies of the models were computed with the oscillation code of Pesnell (1990). The code also allows the computation of the adiabatic frequencies, so that they can be compared to the nonadiabatic ones.

Table 3.17: Input parameters considered by Team5 to compute the models. $M/\mathrm{M}_\odot$ is the mass in solar units, Z/X is the initial ratio of heavy elements to hydrogen abundances, and Y the helium abundance. α_{ML} and α_{OV} are the mixing length parameter and the overshooting parameter, respectively.

Parameter	Combination 1	Combination 2	Combination 3
$M/\mathrm{M}_\odot$	[1.18,1.28,1.45]	1.28	1.28
Z/X	0.024	[0.018,0.023]	0.023
Y	0.28	[0.28,0.26]	0.28
α_{ML}	1.92	[1.92,3.5]	1.92
α_{OV}	0	0	0
Diffusion & gravitational settling	None	None	Yes (see text)

Team5 did not use a grid approach to find the best model. They varied the input parameters within few values. They also considered cases with diffusive settling of He and heavier elements. Table 3.17 shows the values used by Team5 to compute the models. The model parameters that give the lowest χ^2_{seis} are shown in Table 3.18. The model has the largest χ^2_{seis} of all teams and a $T_{\mathrm{eff}} = 5760\,\mathrm{K}$ which is not within the 3-σ error for the observed value. This is probably due to the fact that the parameter space explored in this case was very limited.

3.6.2.4 Results, Discussion and Conclusions

Figure 3.8 shows the HR diagram with the position of KIC 10273246 and with the position of the best model found by each team (represented by a star), with the exception of Team5.

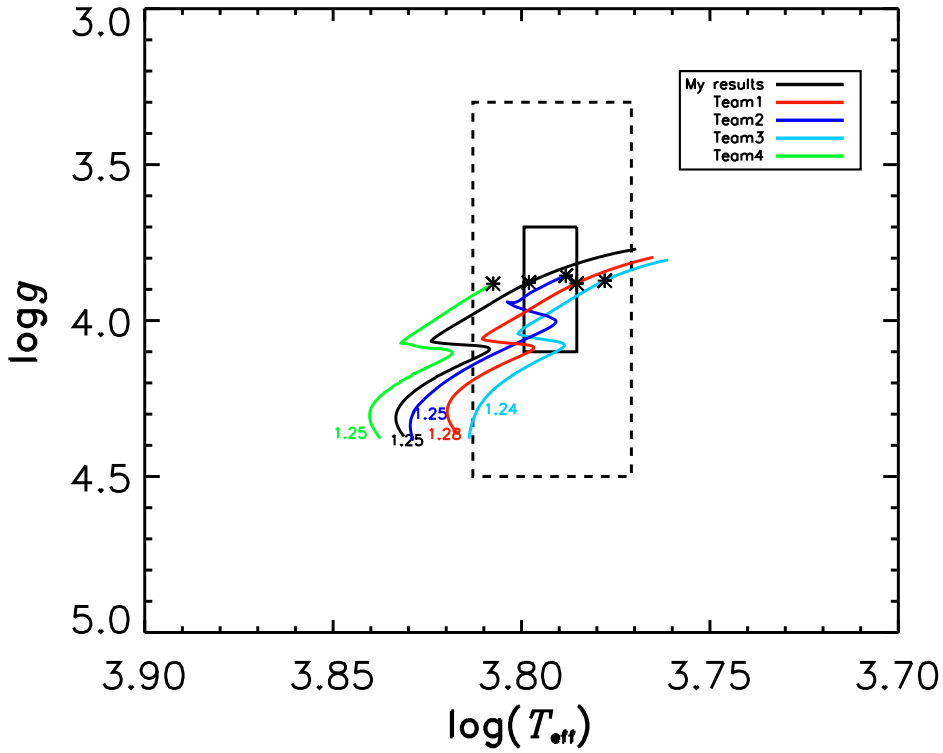

Figure 3.8: The position of KIC 10273246 in the HR diagram shown by the 1-σ uncertainty (filled line box) and by the 3-σ uncertainty (dashed-line box) on the observed parameters. Also shown are the position of the best models found by the different teams (star symbol) along with their evolutionary tracks. Different colours show the results from different teams. The numbers represent the mass, in solar units.

All the models lie within the 3-σ error-box (dashed line) of KIC 10273246. The best fitted values for KIC 10273246, as given by the different teams, are shown in Table 3.18. This Table also shows the $\chi^2_{\rm seis}$ value as defined in Eq. (3.5.2), which represents the quality of the fit.

Inspection of the échelle diagram of Figure 3.7 shows that the near-surface corrections seem to work relatively well for the higher frequencies, say $\nu > 1000\,\mu$Hz, but increase the disagreement for the modes with the lower frequencies. This possible failure of the empirical surface corrections for stars hotter than the Sun has been noted also in other recent works (Doğan et al. 2010; Reese et al. 2012); (Metcalfe 2012, private communication). Nevertheless, Mathur et al. (2012) analysed 22 solar-type stars observed by *Kepler*, some of which with effective temperatures similar to that of KIC 10273246, and the near surface

Table 3.18: The parameters of the best models found for KIC 10273246 from the six different teams. The mass, M, luminosity, L, and radius, R, are expressed in solar units. $T_{\rm eff}$ is the effective temperature, Y_i and Z_i are the initial helium and heavy-element abundances, $Z/X_{\rm i}$ is the initial mass ratio of heavy elements to hydrogen, and α corresponds to $\alpha_{\rm CGM}$ for Team4 and to $\alpha_{\rm ML}$ to the other teams. The metallicity, [Fe/H] was computed using the solar value $[{\rm Fe/H}]_\odot = 0.0245$ (Grevesse & Noels 1993).

Team	$M/{\rm M}_\odot$	$(Z/X_{\rm i})$	Y_i	α	$\alpha_{\rm OV}$	τ (Gyr)	$L/{\rm L}_\odot$	$R/{\rm R}_\odot$	$T_{\rm eff}\,K$	$\log g$	[Fe/H]	$\chi^2_{\rm seis}$
My results	1.25	0.014	0.264	2.00	0.0	3.563	6.336	2.131	6281	3.878	-0.24	37
Team1	1.28	0.014	0.230	2.00	0.0	4.108	5.744	2.149	6101	3.881	-0.24	23
Team2	1.25	0.016	0.270	1.80	0.1	3.800	6.060	2.184	6141	3.856	-0.18	26
Team3	1.24	0.016	0.249	1.86	0.0	4.290	5.293	2.136	5996	3.872	-0.18	11
Team4	1.25	0.011	0.260	0.64	0.0	3.455	6.817	2.114	6420	3.882	-0.33	15
Team5	1.28	0.024	0.260	1.92	0.0	4.480	5.176	2.180	5760	3.868	-0.01	72
mean	1.258	0.0158	0.255			3.949	5.904	2.149	6116	3.873		
st.dev.	(0.017)	(0.004)	(0.014)			(0.409)	(0.628)	(0.028)	(228)	(0.001)		
Creevey et al. (2012)	1.26 ± 0.10					3.7 ± 0.7	5.3 ± 1.1	2.11 ± 0.05		3.88 ± 0.02		

correction seemed to work well. This has to be further investigated and reinforces the need for a better modelling of the surface layers of stars.

In this work, the different teams made the analysis independently and they also used different evolutionary codes with different input physics such as diffusion, core overshoot, and rotation. The mean values of the mass, luminosity, radius, age and log g are well in agreement, within 1-σ, with those found by the pipeline analysis on the average asteroseismic properties given by Creevey et al. (2012) (see Table 3.18).

We will soon have new frequencies for KIC 10273246, since the star has been put back in the list of *Kepler* WG1 targets. We expect that with the new frequencies we may be able to make some inferences about the interior of the star. Also, we may need to refine our grids in order to find parameters that represent better the observed oscillation frequencies.

3.6.3 16 Cygni

The asteroseismic modelling of 16 Cygni was part of a project within WG1, workpackage PS4. I contributed to the modelling of this star, using the method described in Section 3.5.

16 Cygni is a triple system with two solar-analogs and a red dwarf companion that is 10 magnitudes fainter (Turner et al. 2001; Patience et al. 2002). The goal of the project was to model the two solar-analogs of the system. The component A (16 Cyg A, HD 186408, KIC 12069424) and the component B (16 Cyg B, HD 186427, KIC 12069449) are very bright G-type dwarfs, with visual magnitudes of 5.96 (G1.5Vb) and 6.20 (G3V), respectively. The system has a 1.5 Jupiter-mass exoplanet in an eccentric 800-day orbit around 16 Cyg B (Cochran et al. 1997) and since its discovery a major interest on these stars has appeared. Although being a binary system, there are no constraints on their masses because the available data suggest that component B is at a distance of 860 AU from component A with an orbital period longer than 18,000 years (Hauser & Marcy 1999). Their ages were estimated near 6-8 Gyr (Wright et al. 2004; Valenti & Fischer 2005). 16 Cyg A & B were observed during three months by the *Kepler* satellite which provided exquisite frequency-power spectra for both stars. Both spectra show clear solar-like oscillations with more than fifteen radial overtones including many octupole ($l = 3$) modes.

3.6.3.1 Seismic and non-seismic constraints

Ten teams within WG1 provided estimates of the frequencies of the observed modes, applying peak-bagging techniques developed for application to CoRoT (Appourchaux et al.

2008) and *Kepler* data (e.g. Campante et al. 2011; Mathur et al. 2011). One of teams was chosen to provide the final set of frequencies for the two stars (see Metcalfe et al. (2012) for details). These included a total of 46 and 41 individual frequencies for 16 Cyg A & B, respectively. The frequencies are shown in Table 3.19.

To complement the seismic data we used the non-seismic constraints from Ramírez et al. (2009) obtained from spectroscopic analysis. The authors give the effective temperature, logarithm of gravity, and metallicity for both components (see Table 3.20). Their values of the effective temperature were used to obtain bolometric corrections from Flower (1996) and adopting $M_{\mathrm{bol},\odot} = 4.73 \pm 0.03$ from Torres (2010), the extinction estimates from Ammons et al. (2006) with the updated Hipparcos parallaxes (van Leeuwen 2007) were combined to obtain the luminosity constraints for both stars. These are shown in Table 3.20.

3.6.3.2 Modelling 16 Cyg A and 16 Cyg B

Although 16 Cyg A & B are members of a binary system and presumably formed simultaneously from the same material, the modelling was performed independently without forcing both stars to have the same age and chemical composition. The stars were firstly modelled by AMP, which yielded one best model for each of them with a χ^2_{seis} less than 10 and a χ^2_{spect} less than 1, so the models give a reasonable good match to both constraints. The optimal parameters found by AMP for both stars are shown in Table 3.21 along with the asteroseismic χ^2. The statistical uncertainties on each parameter (σ_{stat}) were determined using Singular Value Decomposition (SVD) (Metcalfe et al. 2009).

Based on the results from AMP, six teams, including myself, used different stellar evolution codes and fitting methods to model both stars. The goal was to evaluate the possible sources of systematic uncertainty from the ingredients and assumptions of AMP models.

To perform the modelling of both stars, I constructed two grids (Grid I) of evolutionary models (one for 16 Cyg A and one other for 16 Cyg B) which input parameters are shown in Table 3.22. Then, based on the results of Grid I, I refined it until getting the parameters shown in Grid II. The input physics used to compute the models are described in Section 3.2. Diffusion and settling were not considered, nor were rotation or magnetic fields. The method that I used to perform the modelling is described in Section 3.5. For the models that lie inside the 1-σ constraints for the log g, [Fe/H], T_{eff}, and L, oscillation frequencies were computed. The best fit is given by the model whose frequencies reproduce best the observed frequencies, i.e., the model that has the lowest χ^2_{seis} as defined by Eq. (3.5.6). To apply the correction term we used $b = 4.90$ and $\nu_0 = 2161\,\mu$Hz for 16 Cyg A and $\nu_0 = 2503\,\mu$Hz for

Table 3.19: Observed oscillation frequencies for 16 Cyg A & B.

	16 Cyg A				16 Cyg B			
n^a	$\ell = 0$ (μHz)	$\ell = 1$ (μHz)	$\ell = 2$ (μHz)	$\ell = 3$ (μHz)	$\ell = 0$ (μHz)	$\ell = 1$ (μHz)	$\ell = 2$ (μHz)	$\ell = 3$ (μHz)
13	...	...	1591.21 ± 0.86	...	...	...	...	...
14	1598.51 ± 0.27	1644.24 ± 0.33	1693.73 ± 0.46	1736.03 ± 1.84	...	...	1920.99 ± 0.24	...
15	1700.43 ± 0.34	1746.93 ± 0.24	1795.87 ± 0.40	1839.07 ± 1.64	1928.81 ± 0.28	1982.66 ± 0.16	2036.59 ± 0.20	...
16	1802.15 ± 0.17	1849.11 ± 0.13	1898.08 ± 0.27	1944.07 ± 1.57	2044.21 ± 0.15	2098.20 ± 0.17	2152.91 ± 0.19	2202.75 ± 0.65
17	1904.62 ± 0.15	1951.98 ± 0.16	2001.82 ± 0.17	2045.09 ± 0.80	2159.36 ± 0.16	2214.00 ± 0.18	2269.07 ± 0.21	2317.08 ± 0.44
18	2007.45 ± 0.13	2055.41 ± 0.16	2105.60 ± 0.15	2150.15 ± 0.19	2276.03 ± 0.12	2330.88 ± 0.16	2386.30 ± 0.17	2436.78 ± 0.33
19	2110.94 ± 0.11	2158.89 ± 0.12	2208.90 ± 0.19	2253.41 ± 0.35	2392.87 ± 0.14	2448.17 ± 0.11	2503.56 ± 0.13	2553.00 ± 0.23
20	2214.33 ± 0.17	2262.32 ± 0.16	2312.49 ± 0.29	2356.92 ± 0.46	2509.75 ± 0.13	2565.35 ± 0.10	2619.99 ± 0.23	2672.34 ± 0.28
21	2317.18 ± 0.17	2366.15 ± 0.16	2416.24 ± 0.33	2461.26 ± 1.04	2626.43 ± 0.11	2682.38 ± 0.14	2737.44 ± 0.31	2788.74 ± 1.40
22	2420.75 ± 0.30	2470.23 ± 0.25	2520.91 ± 0.81	...	2743.15 ± 0.25	2799.67 ± 0.22	2854.52 ± 0.39	2906.96 ± 0.93
23	2524.94 ± 0.39	2575.97 ± 0.31	2624.05 ± 0.51	...	2860.63 ± 0.26	2917.75 ± 0.22	2972.73 ± 0.70	...
24	2629.36 ± 0.36	2678.47 ± 0.47	2730.06 ± 1.03	...	2978.95 ± 0.40	...	3089.46 ± 0.87	...
25	2736.22 ± 1.45	2783.71 ± 1.22	...	...	3096.00 ± 0.54	3152.45 ± 0.61	...	...
26	2838.68 ± 0.38	2889.61 ± 0.38	...	...	3215.94 ± 0.91	3274.63 ± 0.55	...	...

[a] Radial order n from the optimal AMP models.

Table 3.20: Spectroscopic constraints used to model 16 Cyg A and 16 Cyg B. The effective temperature, $T_{\rm eff}$, logarithm of gravity, $\log g$, and metallicity, [Fe/H] are from Ramírez et al. (2009). The luminosity, L, in solar units, was determined from the combination of the bolometric magnitude and the distance.

	$T_{\rm eff}$ (K)	$\log g$ (dex)	[Fe/H] (dex)	L ($L_\odot$)
16 Cyg A	5825 ± 50	4.33 ± 0.07	0.096 ± 0.026	1.56 ± 0.05
16 Cyg B	5750 ± 50	4.34 ± 0.07	0.052 ± 0.021	1.27 ± 0.04

Table 3.21: The best parameters found for 16 Cyg A and for 16 Cyg B. Shown are the results from AMP and my results. The mass, M and radius, R, are expressed in solar units. τ is the age, Y_i and Z_i are the initial helium and heavy-element abundances, and $\alpha_{\rm ML}$ is the mixing-length parameter. $\sigma_{\rm stat}$ is the statistical uncertainty on each parameter derived by AMP.

	$M/M_\odot$	$R/R_\odot$	τ (Gyr)	Z_i	Y_i	$\alpha_{\rm ML}$	$\chi^2_{\rm seis}$
16 Cyg A							
AMP	1.10	1.236	6.5	0.022	0.25	2.06	5.47
$\sigma_{\rm stat}$	0.01	0.016	0.2	0.002	0.01	0.03	
My results	1.10	1.237	7.5	0.023	0.25	2.00	5.70
16 Cyg B							
AMP	1.06	1.123	5.8	0.020	0.25	2.05	9.80
$\sigma_{\rm stat}$	0.01	0.020	0.1	0.001	0.01	0.03	
My results	1.05	1.121	7.3	0.021	0.25	2.00	7.97

16 Cyg B.

The best fit parameters for each star are shown in Table 3.21, and the échelle diagrams are shown in Figure 3.9.

3.6.3.3 Conclusions and Discussion

We derived the properties of each star, 16 Cyg A and 16 Cyg B independently by fitting stellar models to the oscillation frequencies (see Table 3.19) and other observational constraints (see Table 3.20) simultaneously. Figure 3.9 shows the échelle diagrams for 16 Cyg A (upper panel) and for 16 Cyg B (lower panel) before (left panel) and after (right panel) applying the near surface corrections to the model frequencies. We see that after the corrections are applied, there is a clearly better match between the observed and the frequencies of the best model. We find that the near surface corrections work well for both 16 Cyg A and 16 Cyg B,

Table 3.22: Parameters space used to compute the evolutionary models for 16 Cyg A (2nd column) and for 16 Cyg A (3rd column). $M/M_{\odot}$ is the mass in solar units, Z/X is the initial ratio of heavy elements to hydrogen abundances, Y the helium abundance, $\alpha_{\rm ML}$ is the mixing-length parameter and $\alpha_{\rm OV}$ is the overshoot parameter. The models were computed without diffusion or settling. In parenthesis are the steps.

	16 Cyg A		16 Cyg B	
Parameter	*Grid I*	*Grid II*	*Grid I*	*Grid II*
$M/M_{\odot}$	0.95 - 1.15 (0.05)	[0.95,1.00,1.03,1.05,1.07,1.10,1.15]	0.95 - 1.15 (0.05)	[0.95,1.00,1.03,1.04,1.05] [1.06,1.07,1.08,1.10,1.15]
Z/X	0.029 - 0.032 (0.001)	[0.029,0.030,0.0305] [0.031,0.0315,0.032]	0.026 - 0.029 (0.001)	0.026 - 0.029 (0.001)
Y	0.24 - 0.28 (0.02)	[0.24, 0.245,0.25,0.26,0.27,0.28]	0.24 - 0.28 (0.02)	[0.24, 0.245,0.25,0.26,0.27,0.28]
$\alpha_{\rm ML}$	1.2 - 2.2 (0.2)	[1.2,1.4,1.6,1.8,2.0,2.1,2.2,2.3]	1.2 - 2.2 (0.2)	1.2 - 2.2 (0.2)
α_{OV}	0	0	0	0

whose spectroscopic parameters are closer to those of the Sun.

Our results were analysed together with the results from five more different teams that also provided their best matching parameters to the observables of 16 Cyg A and 16 Cyg B. The results are shown in Table 3.23.

The properties of both stars were firstly given by AMP (see first row of Table 3.23). Then the systematic uncertainties on the derived parameters were evaluated from the results of the six teams, that use a variety of stellar evolution codes and fitting methods. Moreover, the physical ingredients adopted by each team differed slightly from those employed by AMP, which allowed the exploitation of the degree of model-dependence on the AMP results. The adopted parameters for 16 Cyg A and 16 Cyg B are shown at the bottom of Table 3.23, in the bold row. They were obtained by performing a mean over the individual values weighted by $1/\chi^2$. The systematic uncertainty ($\sigma_{\rm sys}$) on each parameter reflects the variance of the results, again weighted by $1/\chi^2$. Although both stars were modelled independently by the different teams, with the exception of the Geneva and YREC codes (which forced the model for component B to have the same age as the optimal model for the component A), the adopted stellar properties of 16 Cyg A& B reinforce the conclusion that the two stars share a common age ($\tau = 6.8 \pm 0.4$ Gyr) and initial composition ($Z_i = 0.024 \pm 0.002$, $Y_i = 0.25 \pm 0.01$), as expected for a binary system.

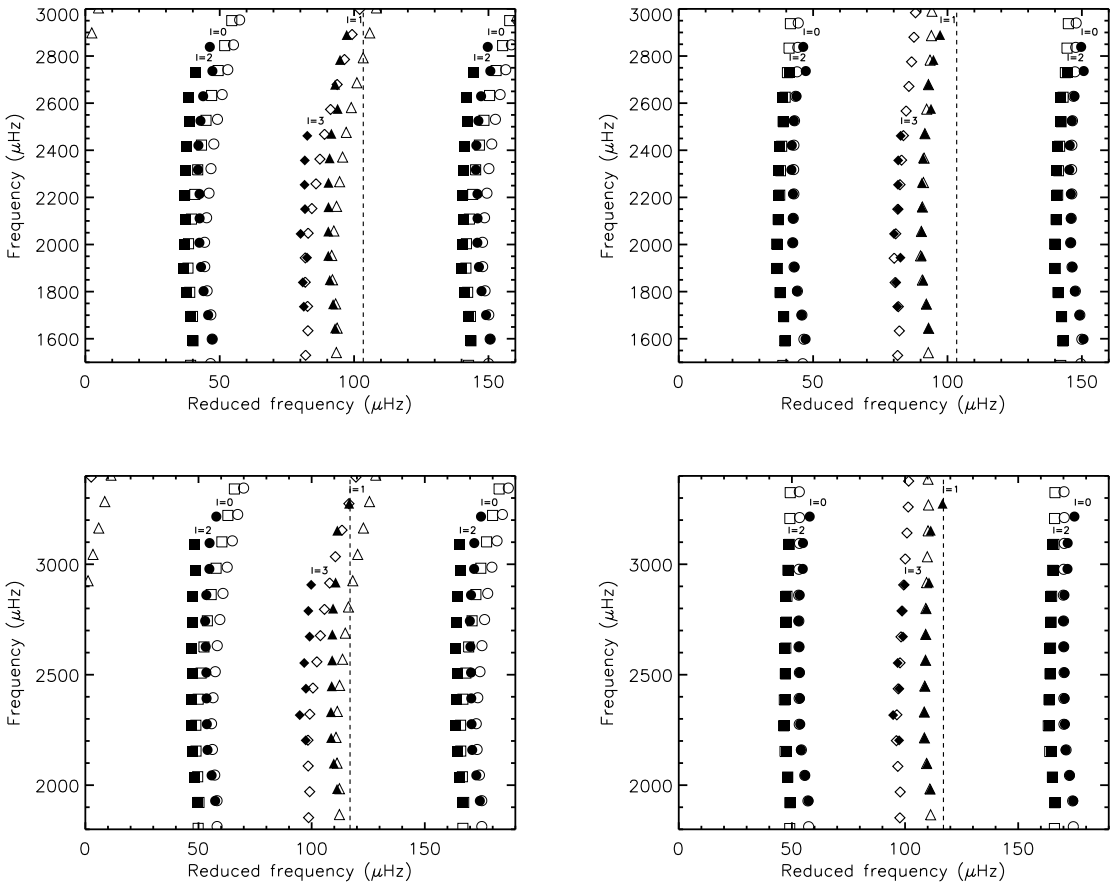

Figure 3.9: Échelle diagrams for 16 Cyg A (upper panel) and for 16 Cyg B (lower panel), before (left panel) and after (right panel) applying the near surface corrections to the model frequencies. The Échelle diagrams were plotted with a frequency separation of $\Delta\nu = 103.4\,\mu$Hz and $\Delta\nu = 117.0\,\mu$Hz, for 16 Cyg A & B, respectively. Shown are the frequencies of the best model (open symbols) obtained from my analysis and the observed frequencies (solid symbols) (c.f. Table 3.19). Circles are used for $l = 0$ modes, triangles for $l = 1$, squares for $l = 2$, and diamonds for $l = 3$.

3.7 Conclusions

In this Chapter we have presented our work on the asteroseismic modelling of three solar-like pulsators, namely β Hyi, KIC 10273246, and 16 Cyg. We refer to *asteroseismic modelling* to the method of finding a set of model parameters that best fit the seismic and non-seismic data of a pulsating star. The best fit is found by performing a χ^2 minimization between the model parameters and the observables.

The three stars that we have modelled have different stellar parameters, namely β Hyi has a

mass and effective temperature close to those of the Sun, but it is more evolved, KIC 10273246 is hotter than the Sun, and 16 Cyg is slightly more massive and more evolved than the Sun.

The method that we used to model these three stars include the observed individual frequencies as constraints to the models. Moreover, we try to fit within 1-σ or 3-σ the fundamental parameters such as the luminosity (or $\log g$), $T_{\rm eff}$, and the metallicity, [Fe/H], if applicable.

When the individual frequencies are used as constraints to models of solar-like pulsators a correction to the model frequencies is necessary. Such a correction has been suggested by Kjeldsen et al. (2008) and it is needed due to our incapability to model properly the surface layers of stars. We applied this empirical correction to the frequencies of our computed models before comparing them to the observed frequencies.

We found that for all of the three stars under study, the $\chi^2_{\rm seis}$ is greater than 1. This means that either the observational uncertainties are underestimated or the models fail in reproducing the data even when the empirical surface corrections are applied. The fact that $\chi^2_{\rm seis} > 1$ is also seen in recent works such as the one concerning the asteroseismic modelling of the star KIC 11026764 (Metcalfe et al. 2010) and in a more recent work by Mathur et al. (2012) that modelled a sample of 22 *Kepler* stars.

Of the three stars presented in this Chapter, we found that the best $\chi^2_{\rm seis}$ is the one from β Hyi followed by 16 Cyg. In both cases, the observed frequencies seem to fit well the model ones. The difference in $\chi^2_{\rm seis}$ for these stars is associated to the fact that the uncertainties in the observed frequencies of 16 Cyg are, in general, much smaller than those of β Hyi. Concerning, KIC 10273246, this star is slightly hotter than 16 Cyg and β Hyi. The correction applied to the model frequencies of KIC 10273246 seem not to work as well as for the other two stars. For instance, the fit at lower frequencies becomes worse after applying the empirical correction.

The fact that $\chi^2_{\rm seis} > 1$ when using the individual frequencies to model solar-like pulsators may suggest that our models or our procedure to model these stars start to fail, as the seismic data becomes more precise. This reinforces the idea that the physics of the existing evolutionary codes needs to be improved, specially in what concerns convection, so that a better characterization of the surface layers of stars can be achieved.

Table 3.23: Table from Metcalfe et al. (2012) that shows the stellar model-fitting results for 16 Cyg A & B. My results are shown in the line identified by 'ASTEC1'.

	16 Cyg A							16 Cyg B						
	$R/R_\odot$	$M/M_\odot$	t(Gyr)	Z_i	Y_i	α	χ^2	$R/R_\odot$	$M/M_\odot$	t(Gyr)	Z_i	Y_i	α	χ^2
AMP	1.236	1.10	6.5	0.022	0.25	2.06	5.47	1.123	1.06	5.8	0.020	0.25	2.05	9.80
σ_{stat}	0.016	0.01	0.2	0.002	0.01	0.03	...	0.020	0.01	0.1	0.001	0.01	0.03	...
ANKİ ...	1.260	1.14	6.4	0.024	0.26	1.94	21.41	1.138	1.08	6.4	0.022	0.26	1.94	23.29
ASTEC1.	1.237	1.10	7.5	0.023	0.25	2.00	5.70	1.121	1.05	7.3	0.021	0.25	2.00	7.97
ASTEC2.	1.235	1.10	6.8	0.022	0.25	2.00	7.70	1.134	1.09	6.3	0.025	0.25	2.00	8.47
CESAM .	1.253	1.14	7.0	0.027	0.24[a]	0.72[b]	3.53	1.136	1.09	6.9	0.025	0.24[a]	0.73[b]	4.78
Geneva ..	1.236	1.10	6.7[c]	0.024[c]	0.26[c]	1.80[c]	10.82	1.122	1.06	6.7[c]	0.024[c]	0.26[c]	1.80[c]	10.98
YREC ...	1.244	1.11	6.9	0.026	0.26	2.08	5.68	1.121	1.05	6.9[d]	0.022	0.26	1.84	3.17
adopted	**1.243**	**1.11**	**6.9**	**0.024**	**0.25**	**2.00**	...	**1.127**	**1.07**	**6.7**	**0.023**	**0.25**	**1.92**	...
σ_{sys}	0.008	0.02	0.3	0.002	0.01	0.08	...	0.007	0.02	0.4	0.002	0.01	0.09	...

[a] Values of $Y_i < 0.24$ excluded from search.

[b] Value of α from the Canuto et al. (1996) treatment of convection, excluded from average.

[c] Age, composition, and mixing-length constrained to be identical in both components.

[d] Age of 16 Cyg B constrained to be identical to the value found for 16 Cyg A.

Chapter 4

Convective cores

4.1 Introduction

According to stellar structure theory, stars slightly more massive than the Sun ($M > 1.0$ $M_\odot$) may develop a convective core at some stages of their evolution on the main-sequence phase. This occurs when radiation can no longer transport the amount of energy produced by nuclear burning in the internal regions of a star, when that energy becomes too high. For these stars hydrogen burning happens through the CNO cycle, which has a strong dependence on the temperature. Convection is then the most effective process to transport the energy, hence a convective core is present. Knowing some of the physical properties of the core of a star is of great importance since it is this region that mostly determines the evolution of a star. Since convection implies chemical mixing, the evolution of these stars is severely influenced by the presence, and the extent, of the convective core.

When we analyse models of an intermediate-mass star (1 $M_\odot < M \leq 2$ $M_\odot$) with a convective core, we see that the core's size does not remain constant during the evolution of the star. It increases during the initial stages of evolution before beginning to shrink, later on (see Figure 4.1). Also, some physical ingredientes such as the convective core overshoot, if present in the modelling, will influence the extent and evolution of the convective core (see Figure 4.2).

A convective core is believed to be homogeneously mixed since the timescale for mixing of elements is much shorter than the nuclear timescale. Thus, if diffusion is not taken into account, the growing core causes a discontinuity in the composition at the edge of the core (Mitalas 1972; Saio 1975) (Figure 4.1, upper panel). Since pressure and temperature are continuous, this results in a density discontinuity. If diffusion is present, instead of a

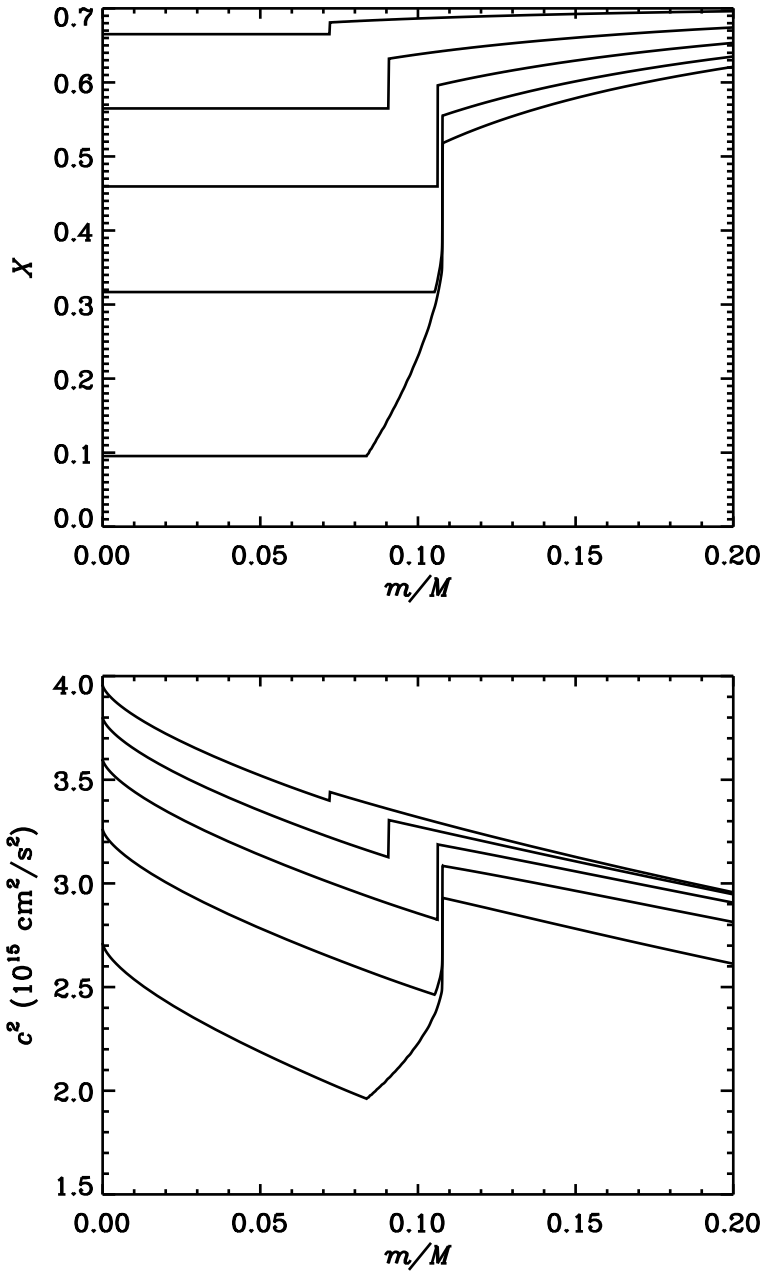

Figure 4.1: The hydrogen profile (upper panel) and the sound speed profile (lower panel) in the inner region of a 1.4 $M_\odot$ star with $\alpha_{OV} = 0.1$ and with solar metallicity, $Z/X = 0.0245$. The different curves correspond to different stages of evolution, with ages: 0.21 Gyr (top curve), 0.75 Gyr, 1.29 Gyr, 1.86 Gyr and 2.51 Gyr (bottom curve). The length of the constant line in X indicates the fractional mass of the convectively mixed core, the latter being fully mixed due to convection. The mass fraction of this region increases during the first part of evolution before decreasing in later stages. If we had included diffusion in these models, we would have found a strong gradient in the hydrogen abundance rather than a discontinuity, in the growing phase of the core. The discontinuity seen in c^2 is caused by the discontinuity in X.

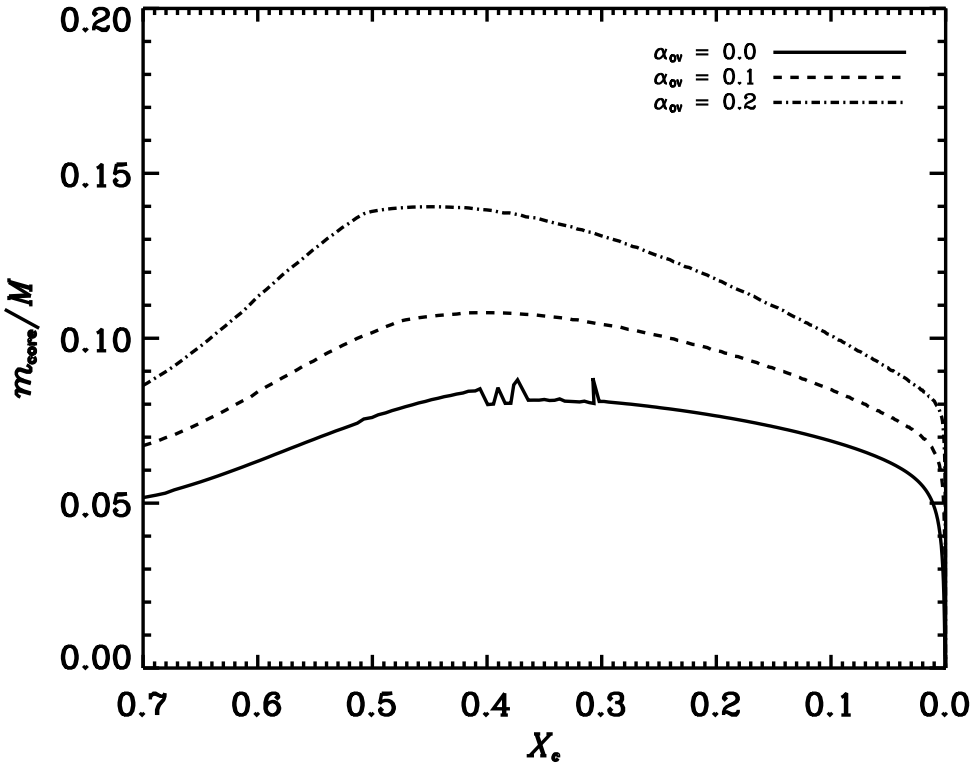

Figure 4.2: Evolution of the fractional mass of the convectively mixed core, m_{core}/M for models with mass of 1.4 $M_\odot$ and solar metallicty, $Z/X = 0.0245$. The black line represents the model without core overshoot, $\alpha_{OV} = 0.0$, the dashed line with $\alpha_{OV} = 0.1$ and the dashed-dot line $\alpha_{OV} = 0.2$.

discontinuity, there will be a very sharp gradient in the chemical abundance and density at the edge of the convective core. Moreover, a retreating core leaves behind a non-uniform chemical profile (Faulkner & Cannon 1973) causing also a sharp gradient in the chemical abundance (Figure 4.1, upper pannel, bottom curve).

As mentioned in Chapter 1, the oscillation frequencies of a pulsating star depend on its global properties, such as the mass and radius, but they are also affected by the presence and by the location of sharp variations in the density or in the chemical composition inside the star. Different combinations of low-degree p modes have been shown to probe the interior of stars (e.g., Christensen-Dalsgaard 1984), the most commonly used being the large and small frequency separations, already defined in Chapter 1. These two diagnostic tools are, however, affected by the poorly modelled outer layers of stars. More recently, Roxburgh & Vorontsov (2003) proposed smooth 5 points small frequency separations, d_{01} and d_{10}, as a diagnostic of stellar interiors. Moreover, the authors demonstrated that the effect of the outer stellar regions in the oscillation frequencies is cancelled out when one considers the ratios of these diagnostics (see also, Roxburgh & Vorontsov 2004; Roxburgh 2005; Otí Floranes et al. 2005). The small separations are defined by,

$$d_{01}(n) = \frac{1}{8}(\nu_{n-1,0} - 4\nu_{n-1,1} + 6\nu_{n,0} - 4\nu_{n,1} + \nu_{n+1,0}) \tag{4.1.1}$$

$$d_{10}(n) = -\frac{1}{8}(\nu_{n-1,1} - 4\nu_{n,0} + 6\nu_{n,1} - 4\nu_{n+1,0} + \nu_{n+1,1}) \tag{4.1.2}$$

and the ratios by,

$$r_{01}(n) = \frac{d_{01}(n)}{\Delta_1(n)}, \qquad r_{10} = \frac{d_{10}(n)}{\Delta_0(n+1)}\,, \tag{4.1.3}$$

$$r_{02}(n) = \frac{d_{02}(n)}{\Delta_1(n)}\,, \tag{4.1.4}$$

where $\Delta_l(n) = \nu_{n,l} - \nu_{n-1,l}$ and $d_{02} \equiv \delta\nu_{n0}$ has been defined in Chapter 1, Eq. (1.0.21). The down side of these diagnostic tools, namely the d_{02}, d_{01}, d_{10} or their respective ratios is that they do not isolate the signature of the edge of the core, although they are strongly affected by it.

Cunha & Metcalfe (2007) carried out a theoretical analysis based on the properties of the oscillations of stellar models slightly more massive than the Sun and derived the expected signature of the border of a small convective core on the oscillation frequencies. The authors assumed that this signature is caused by the discontinuity in the composition and hence in the sound speed at the edge of the growing convective core. They have shown that the following combination of oscillation frequencies is sensitive to the properties of the

sound speed discontinuity, and is also capable of isolating the consequent perturbation on the oscillation frequencies:

$$dr_{0213} = \frac{D_{02}}{\Delta\nu_{n-1,1}} - \frac{D_{13}}{\Delta\nu_{n,0}}. \tag{4.1.5}$$

This diagnostic tool corresponds to a difference of ratios between the scaled small separations, $D_{l,l+2} \equiv (\nu_{n,l} - \nu_{n-1,l+2})/(4l + 6)$, and the large separations $\Delta\nu_{n,l} \equiv \nu_{n+1,l} - \nu_{n,l}$ for different combinations of mode degrees. More recently, Cunha & Brandão (2011) improved the analysis presented in Cunha & Metcalfe (2007), by considering a different expression to describe the sound speed variation at the edge of the growing convective core, which is more in line with the variation observed from the equilibrium models. Moreover, they showed that the derivative of the diagnostic tool dr_{0213} can potentially be used to infer the amplitude of the relative sound speed variation at the edge of the growing core. This is because

$$dr_{0213} \approx \frac{\delta\nu^c}{6\Delta\nu_{n-1,1}}, \tag{4.1.6}$$

with $\delta\nu^c = (2\pi)^{-1}\delta\omega$. Here, $\delta\omega$ is the perturbation to the oscillation frequency induced by the discontinuity at the edge of the core, which can be computed from the relative perturbation to the sound speed squared, $\delta c^2/c^2$ through the relation,

$$2I_1\omega\delta\omega \approx -[\delta c^2/c^2]_{r=r_d}[h\overline{\psi^2}]_{r=r_d} + \frac{[\delta c^2/c^2]_{r=rd}}{\Delta^2}\int_{r_d-\Delta}^{r_d}\frac{\mathrm{d}}{\mathrm{d}r}\left\{h(r - r_d + \Delta)^2\right\}\overline{\psi^2}\mathrm{d}r. \tag{4.1.7}$$

$[\delta c^2/c^2]_{r=r_d}$ and Δ are, respectively, the size of the jump and the width of the perturbation. r_d is the radial position at which the jump in the sound speed occurs (see, Figure 4.3). I_1 is related to the mode inertia, h is a function of r that depends on the equilibrium properties of the star, as well as on the frequency of the oscillations. Finally, $\overline{\psi^2} = \int \psi^2 dx$, where ψ is related to the displacement eigenfunction, and x follows from a particular transformation of the independent variable r (see Cunha & Metcalfe 2007, for details).

Cunha (2012) (private communication) showed that Eq. (4.1.7) can be written as

$$2I_1\omega\delta\omega \approx -\frac{[\delta c^2/c^2]_{r=r_d}}{\Delta^2}\int_{r_d-\Delta}^{r_d} h[r - r_d + \Delta]^2\frac{\mathrm{d}\overline{\psi^2}}{\mathrm{d}r}\mathrm{d}r, \tag{4.1.8}$$

or simply

$$2\pi\delta\nu^c = \delta\omega = -[\delta c^2/c^2]_{r=r_d}T(t_\mathrm{m},\omega)\ f(t_\mathrm{m},\omega) \tag{4.1.9}$$

where $T(t_\mathrm{m},\omega)$ is a term which is weakly dependent on the model's age, t_m, and the oscillation frequency, ω, and $f(t_\mathrm{m},\omega)$ is also weakly model's age dependent but strongly dependent on the oscillation frequency. As shown in Figure 4.4, for each model, there is a region of frequencies in which the frequency derivative of dr_{0213} is approximately constant. Since $\Delta\omega dr_{0213} \propto \delta\nu^c$, in that region we have $\Delta\nu\,\mathrm{d}dr_{0213}/\mathrm{d}\nu \propto [\delta c^2/c^2]_{r=r_d}$, which means that the

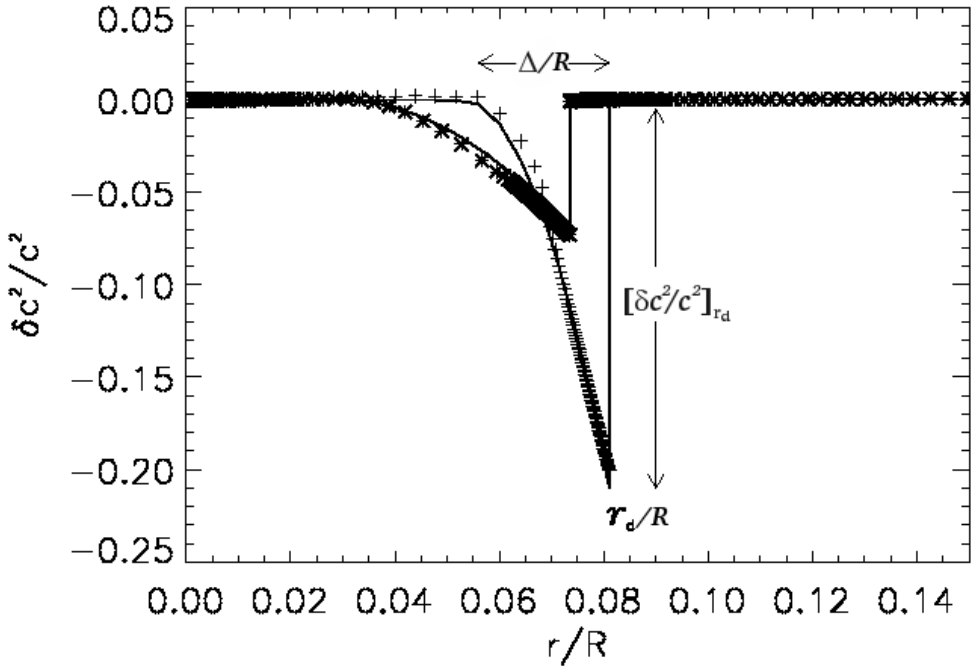

Figure 4.3: The relative perturbation to the sound speed squared, $\delta c^2/c^2$ in the inner regions of two models with $M = 1.3\,M_\odot$ and ages of 2.25 Gyr (smaller amplitude) and 4.0 Gyr (larger amplitude). The symbols represent the difference between the sound speed of the original model and the otherwise similar one with no jump in the sound speed (the so called "smooth"m̃odel in Cunha & Brandão (2011)). The continuous lines correspond to the parametrization of $\delta c^2/c^2$ used to compute the perturbation on the oscillation frequencies, $\delta\omega$ (Eq. (1) of Cunha & Brandão (2011)). Also shown are the quantities $[\delta c^2/c^2]_{r=r_d}$, Δ and r_d, which appear in, for the model of 4.0 Gyr of age.

size of the jump at the edge of the growing core can be, in principle, obtained from the derivative of the diagnostic tool dr_{0213}.

The downside of this diagnostic tool is that it requires knowledge of the modes of degree from 0 to 3. However, the $l = 3$ modes are significantly harder to detect than the $l \leq 2$, from space-based data. For this reason, Cunha & Brandão (2011) also analysed the effect that the sound speed variation at the edge of the growing core has on the diagnostic tools built from modes of degree up to 2 (c.f. Eqs. (1.0.21), (4.1.1) and (4.1.2)) and showed that their derivatives are also significantly increased, when compared with otherwise similar models with no discontinuity. This increase depends strongly on stellar age, similarly to what Cunha & Metcalfe (2007) found for the dr_{0213}. An example of this is shown in Figure 4.4

Finally, although not deriving the signal that the edge of a convective core produces on the oscillation frequencies, Mazumdar et al. (2006) analysed simulated data from stellar models with varying parameters, and suggested a combination of small separations, averaged over radial order, that can be used to estimate the masses of the convective cores and the stellar ages. Moreover, they explained how the small separations can be combined to provide sensitive tests for the presence of convective overshoot at the edge of the core.

One of the main goals of inferring information of the deepest layers of stars is to improve the description of particular physical processes such as diffusion and convective overshoot, in stellar evolution codes. That, in turn, will improve the mass and age determinations derived from asteroseismic studies.

In this Chapter we will present our work on the study of the properties of the convective cores in main-sequence models of solar-like pulsators. The work is driven, in particular, by the following questions: can we detect the signature of a small convective core on the oscillation frequencies of solar-like pulsators for which photometric data with the quality, such as that of the *Kepler* satellite exists? What is the dependence of this signature on the stellar mass and physical parameters? What is the precision required on the individual frequencies in order to detect the signature of a convective core? Will the detection of such a signature provide information about the stellar age?

In this study, we will focus on the analysis of the diagnostic tools presented in the Eqs. (4.1.3), (4.1.4) and (4.1.5), that involve modes of degree $l \leq 3$. The main goal of this work is to study, in a systematic manner, the behaviour of these diagnostic tools. For that, we derived these tools for a set of stellar models considering a large parameter space and attempted to identify in them some signature of the convective core, and hence of the evolutionary state of the stars.

4.2 Method

We started by computing a set of evolutionary tracks with different values for the mass, M, for the core overshoot parameter, $\alpha_{\rm OV}$, and for the metallicity, Z/X, using the ASTEC code. Figure 4.5 shows a set of evolutionary tracks with different masses computed for a fixed value of the metallicity, namely $Z/X = 0.0245$, and without convective core overshoot. The effect of changing the metallicity and the convective core overshoot are shown, as an example, in Figure 4.6 and in Figure 4.7, respectively. All of these evolutionary tracks contain a fixed number of models, not equally spaced in time, from the ZAMS to the post-

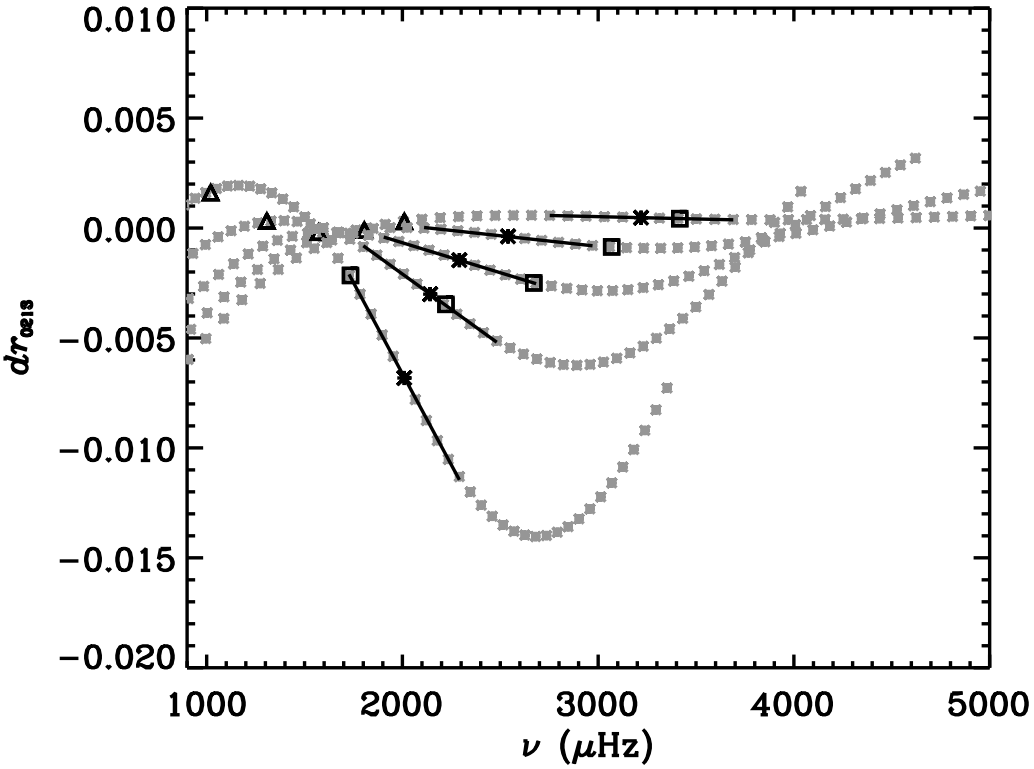

Figure 4.4: The diagnostic tool dr_{0213} as a function of frequency, ν, for a sequence of 1.4 $M_\odot$ models with solar metallicity and without core overshoot. The different curves correspond to models with different ages, the most evolved model being the one with the slope of maximum absolute value. The dark stars represent the frequencies for which the derivative is minimum (maximum absolute slope) for each model, and the straight black lines that cross that minimum correspond to the linear region where the slopes are computed, i. e., the region of approximately constant slope. The triangles represent the frequency of maximum power, ν_{max}, and squares represent the acoustic cut-off frequency, ν_c, computed for each model. Note that for the oldest model, the region of constant slope is above the cut-off frequency for the physics considered in our models.

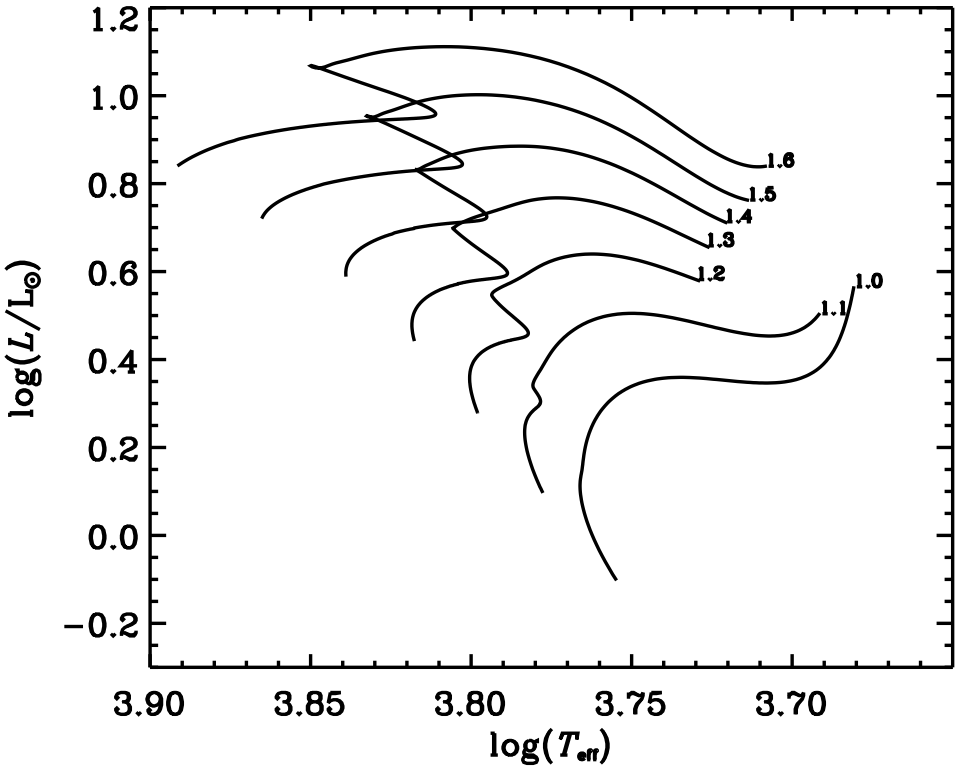

Figure 4.5: The HR diagram for a set of models with solar metallicity, $Z/X = 0.0245$ and no convective core overshoot. The models were evolved from the ZAMS to the post-main sequence. Each evolutionary track contains 300 models at different evolutionary stages. Since the number of the computed models is fixed and the time step varies with mass and also along the evolution, the exact position of the last model of each evolutionary track depends on its mass. The numbers at the end of each evolutionary track correspond to the mass, in solar units.

main sequence.

The parameter space that we considered in the modelling is shown in Table 4.1. We constructed two grids of evolutionary tracks, Grid I and Grid II. For the former we considered solar metallicity, i.e. [Fe/H] = 0 where $(Z/X)_\odot = 0.0245$ (Grevesse & Noels 1993), and varied $\alpha_{\rm OV}$, while in Grid II we fixed $\alpha_{\rm OV} = 0.1$ and considered two extreme values for the metallicity, namely [Fe/H] = -0.5 and [Fe/H] = 0.5. To convert from [Fe/H] to Z/X we used Eq. (3.6.1). The value of helium, Y , was obtained from the relation 3.6.2. We focused our work on intermediate-mass models, i.e. $1.0\,{\rm M}_\odot \leq {\rm M} \leq 1.6\,{\rm M}_\odot$, because it is in this mass range that we expect main-sequence stars to show solar-like pulsations. We fixed the mixing-length parameter to 1.8. We note that changing the mixing length parameter does

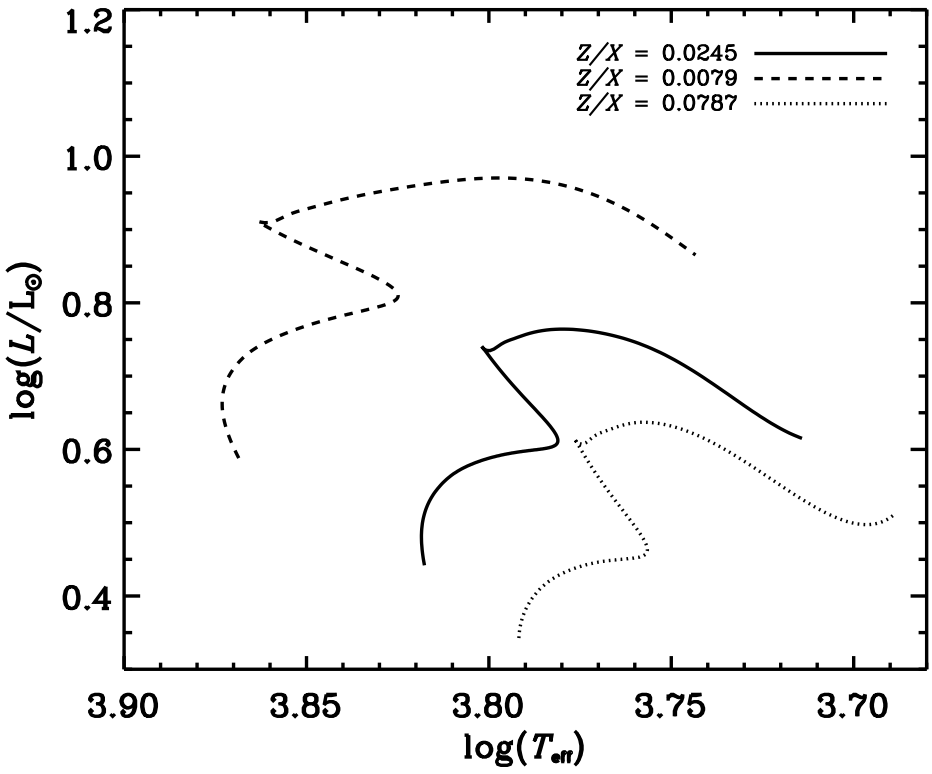

Figure 4.6: The HR diagram for a model of a $1.3\,M_\odot$ with a convective core overshoot of $0.1H_p$. The evolutionary track represented by a solid line corresponds to the model computed with solar metallicity, $Z/X = 0.0245$. The evolutionary tracks represented by the dashed and the dotted lines correspond to models computed for a metallicity lower and higher than solar, respectively.

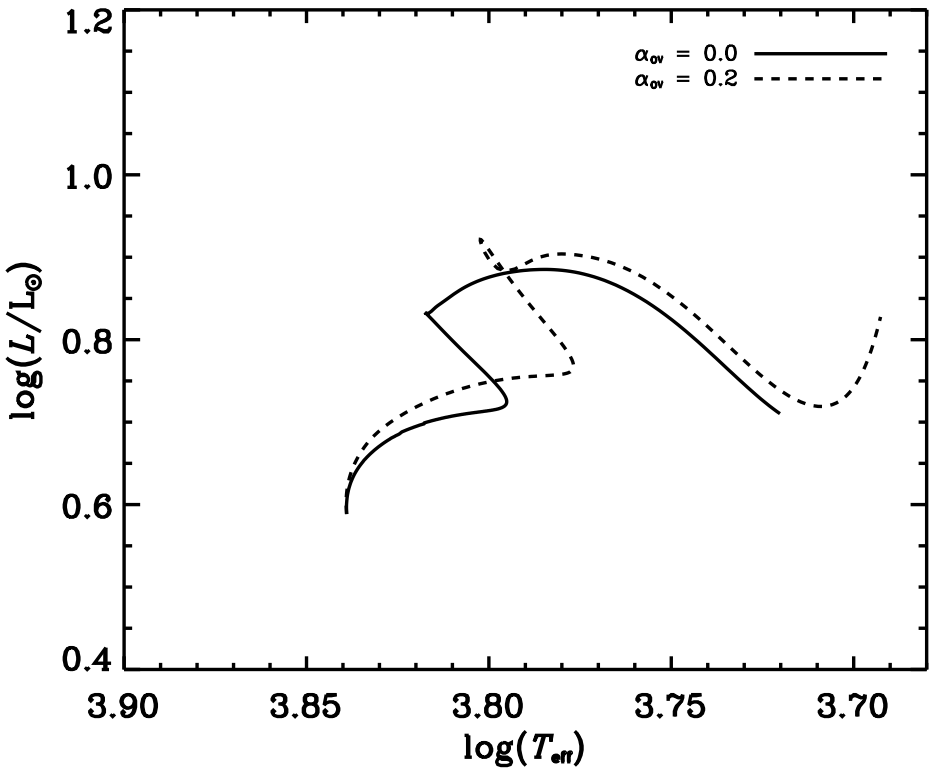

Figure 4.7: The HR diagram of a 1.4 $M_\odot$ model without convective core overshoot (solid line) and with a convective core overshoot of 0.2 (dashed line).

Table 4.1: Parameters used to compute the evolutionary tracks. $M/\mathrm{M}_\odot$ is the mass in solar units, Z/X is the initial ratio of heavy elements to hydrogen abundances, and Y the helium abundance. α_{ML} is the mixing-length parameter and α_{OV} the core overshoot parameter. We considered $(Z/X)_\odot = 0.0245$ (Grevesse & Noels 1993).

Parameter	Grid I	Grid II
$M/\mathrm{M}_\odot$	1.00 - 1.6 (with steps of 0.1)	1.00 - 1.6 (with steps of 0.1)
Z/X	0.0245	[0.0079, 0.0787]
Y	0.278	[0.255, 0.340]
α_{ML}	1.8	1.8
α_{OV}	0.0 - 0.2 (with steps of 0.1)	0.1

not affect the convective core. In this region, the temperature gradient is approximately its adiabatic value and therefore independent of the details in the theory of convection. The values for the metallicity were chosen so that they comprise those derived for the solar-like stars observed by the *Kepler* satellite. The value of the convective overshoot for stars with masses $M < 1.7\,\mathrm{M}_\odot$ is quite unknown with literature values of α_{OV} ranging from 0.00 to 0.25 (Ribas et al. 2000). We considered values for the convective core overshoot between 0.0 and 0.2. The physics considered in the modelling is that described in Section 3.2. Diffusion and settling were not taken into account. Since our goal in this part of the work was only to study the dependence of the diagnostic tools on the input parameters, we did not construct refined grids.

Each evolutionary track contains up to 200 models within the main-sequence phase, i.e. models with hydrogen abundance in the core, $X_c > 10^{-2}$. The true number of models depends mainly on the mass associated with the track. Rather than analysing all the $\lesssim 200$ models, we considered 12 models along the main-sequence phase that are equally spaced in $\log g$, $\log T_{\mathrm{eff}}$, and $\log(L/\mathrm{L}_\odot)$. The reason for not considering all the models along the main-sequence phase was that it would be more computational and human time consuming, and it would not give significant additional information, since our main goal was only to have a global idea of the diagnostic tools' dependencies. To select the 12 models, we started by computing the total parameter 'distance' that a given model travels along the main-sequence in a 3-D space with the following parameters: $\log g$, $\log T_{\mathrm{eff}}$, and $\log(L/\mathrm{L}_\odot)$. The total distance was equally divided in 12 segments, and the 12 models were chosen such as to have their $\log g$, $\log T_{\mathrm{eff}}$, and $\log(L/\mathrm{L}_\odot)$ the closest to the respective values for the 12 segments. Figure 4.8 shows the HR diagram for a set of main-sequence models with mass varying between 1.0 and 1.6 $\mathrm{M}_\odot$, with solar metallicity, and no convective core overshoot. The twelve models are represented by the black star symbol. In this plot the models shown are

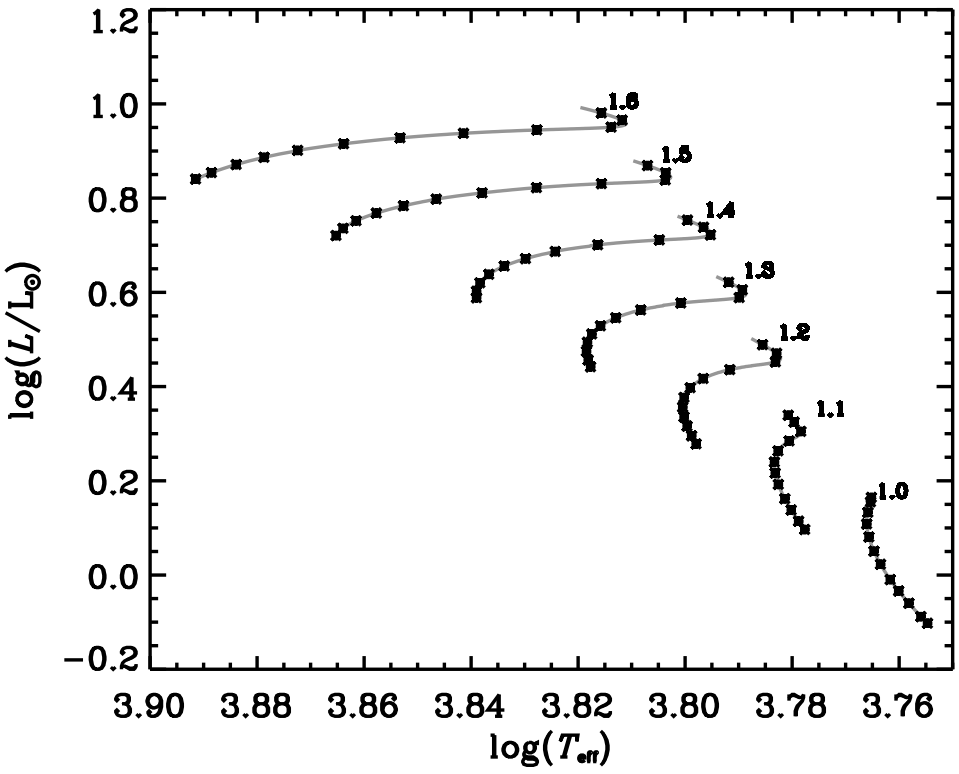

Figure 4.8: The HR diagram for a set of main-sequence models with solar metallicity, and no convective core overshoot. The numbers at the end of each evolutionary track correspond to the mass, in solar units. The 12 selected models within each evolutionary track are shown by a star symbol (see text for details).

not equally spaced since, for clarity, the third dimension, namely log g is not represented. The reason we chose this approach to select the models was that we wanted models that are equally spaced for each track and that is dynamic with the mass, since the distance travelled along the main-sequence phase varies with varying mass. Thus, we had to find a constant step for each track.

For the 12 models within each track we computed oscillation frequencies using the ADIPLS code. Note that the model frequencies were computed up to values above the cut-off frequency ($\nu_c = (2\pi)^{-1}\omega_c$) (cf. Eq. (1.0.11)). Although frequencies that are above the cut-off frequency are not expected to be observed, the reason for us to compute them was because for some models in our grids it is in this range of frequencies that the slopes of the diagnostic tools are approximately constant (see Figure 4.4). Since our first aim was to see how the slopes of the diagnostic tools in this constant region depend on the relative variation of the sound speed at the discontinuity and, thus, on age, we had to consider the high frequencies. The model frequencies were then used to compute the diagnostic tools, d_{01}, d_{10}, d_{02} and their respective ratios r_{01}, r_{10}, r_{02}, and dr_{0213}.

In the case of stars with convective cores we expect the frequency slopes of the diagnostic tools to be a measure of the jump in the sound speed at the edge of the growing convective core (Cunha & Brandão 2011). We started by inspecting the behaviour of the diagnostic tool, dr_{0213}, as a function of frequency and determining the frequency at which the maximum absolute value of the derivative of dr_{0213} was placed, $f_{\rm max}$ associated to a radial order, $n_{\rm max}$. We then computed the slope around $f_{\rm max}$ by performing a linear least square fit to the 10 frequencies of modes of consecutive radial orders, n, centred on $n_{\rm max}$. As for the quantities d_{01}, d_{10}, d_{02}, and their respective ratios, we computed their slopes in the same range of frequency as considered for dr_{0213}. The reason for adopting this procedure was the fact that the behaviour of dr_{0213} as a function of frequency is much smoother. Since our aim was to compute all quantities and slopes in an automated manner, we took advantage of the fact that it is easier to find a global absolute maximum for this quantity, than for the others. Note that in relation to the quantities d_{01} and d_{10} they are both 5-point combinations of modes of $l = 0$ and 1, the first centred on modes of degree $l = 0$ and the second on modes of $l = 1$. In practice, we consider these two quantities together, denoting the result by d_{010}, and the ratios by r_{010}. For these two cases, the slopes are also determined in the same frequency range as that considered for dr_{0213}, but instead of using 10 frequencies we consider 20. In Figure 4.9 we show as an example, the diagnostic tools dr_{0213}, r_{010} and r_{02} computed for a 1.4 $M_\odot$ model without overshoot and with solar metallicity at an age of 1.29 Gyr, and the frequency region where the slopes are measured.

To have an estimation of the error associated with the slope computed for each diagnostic

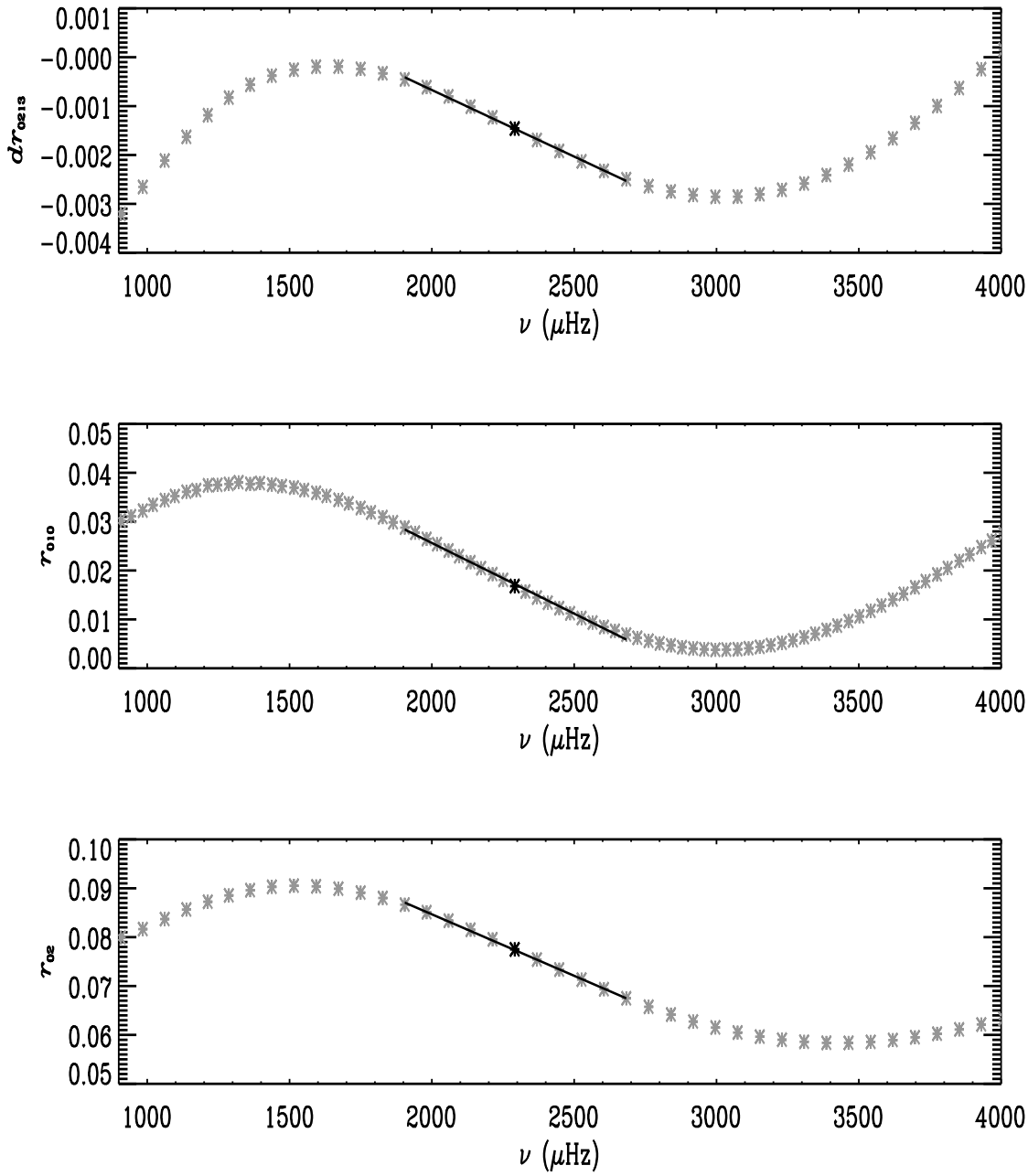

Figure 4.9: The three diagnostic tools, namely dr_{0213} (upper panel), r_{010} (middle panel) and r_{02} (lower panel) as a function of frequency, computed for a 1.4 $M_\odot$ model without core overshoot and with solar metallicity. This model has an age of 1.29 Gyr and corresponds to the 6th model of the 1.4 $M_\odot$ evolutionary track of Figure 4.8.

tool, we chose seven models with different values for the mass and input physics, and with different values of $\delta c^2/c^2$. For these models we randomly generated 10000 sets of model frequencies within the error, assuming a relative error of 10^{-4} for each individual frequency. For each generation, we computed the slopes in the same manner as described above. We then computed the mean of the 10000 values obtained for the slopes and the standard deviation was considered to be our error estimation for the slopes of the diagnostic tools.

As mentioned above, models that have a convective core show a discontinuity. A measure of this discontinuity can be obtained by computing the size of the jump of the sound-speed squared, δc^2. We aim at finding a relation between the relative size of the jump of the sound-speed squared, $\delta c^2/c^2$, and the slopes of the diagnostic tools. Thus, for the models for which we computed the diagnostic tools and that have a convective core, we also computed $\delta c^2/c^2$. To compute the latter, we started by identifying the location (in terms of r/R) of the discontinuity in c^2. To do so we analysed the values of the derivative of the sound-speed squared in the inner regions of the models. As an example, in Figure 4.10 we show the sound-speed profile (upper panel) and its corresponding frequency derivative (lower panel) in the inner regions of a 1.4 $M_\odot$ model at an age of 1.56 Gyr. As expected, the derivative changes the sign, from negative to positive, at the location of the discontinuity. This fact was used to determine the precise location of the jump in an automated manner, for all models. With that we were able to automatically compute the actual size of the sound-speed jump by measuring the difference between the maximum and minimum values of c^2 at the discontinuity. These two values are shown, as an example, by the two black stars in the upper panel of Figure 4.10.

4.3 Results

We verified that no convective core exist in our 1.0 $M_\odot$ sequences of models. Moreover, these models do not show strong sound-speed gradients in the innermost layers, although the sound-speed gradients are being built up as the star evolves. In Figure 4.11, upper panel, we show an example of the sound-speed profile in the innermost regions of a 1.0 $M_\odot$ model with solar metallicity. As can be seen from this figure, there is no discontinuity in c^2. On the other hand, the presence or absence of a convective core in models with 1.1 $M_\odot$ depends on the metallicity considered. All models in our lowest metallicity sequences of 1.1 $M_\odot$, namely with $Z/X = 0.0079$ have no convective core. The most evolved models with 1.1 $M_\odot$ and with solar $Z/X = 0.0245$ metallicity show a convective core (Figure 4.11, middle panel)

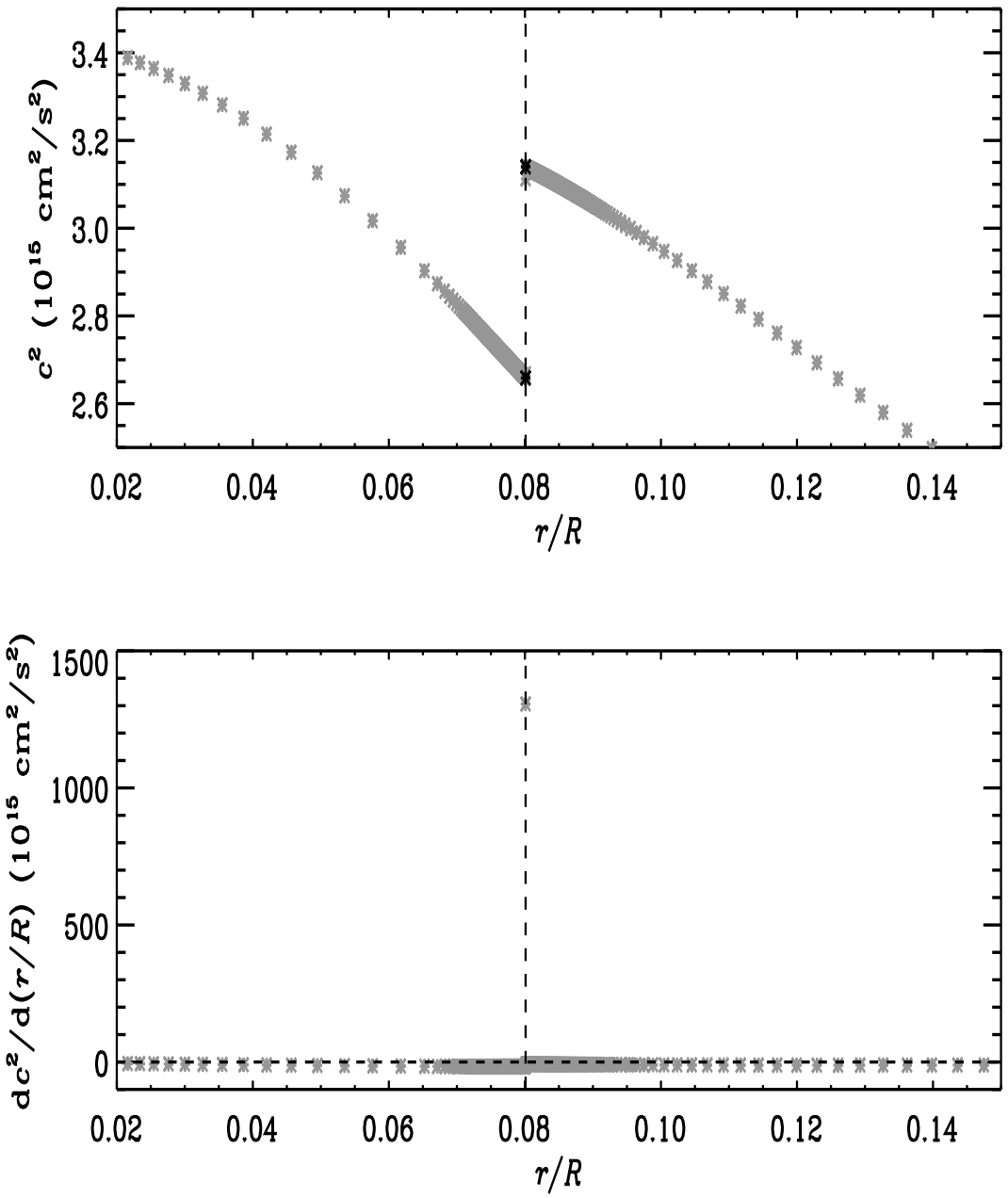

Figure 4.10: The upper panel shows the square of the sound speed in the innermost regions of a 1.4 $M_\odot$ model with an age of 1.56 Gyr computed with solar metallicity and assuming an overshoot from the convective core of $\alpha_{\rm OV} = 0.1$. The lower panel shows the derivative of the square of the sound speed, $dc^2/d(r/R)$, in the same region. The dashed vertical lines in both panels correspond to the location of the discontinuity where the derivative changes its sign from negative to positive. The dashed horizontal line represents the zero in $dc^2/d(r/R)$. The two black star symbols in the upper panel mark the position of the two extremes of the discontinuity, that are used to compute its size in an automated manner.

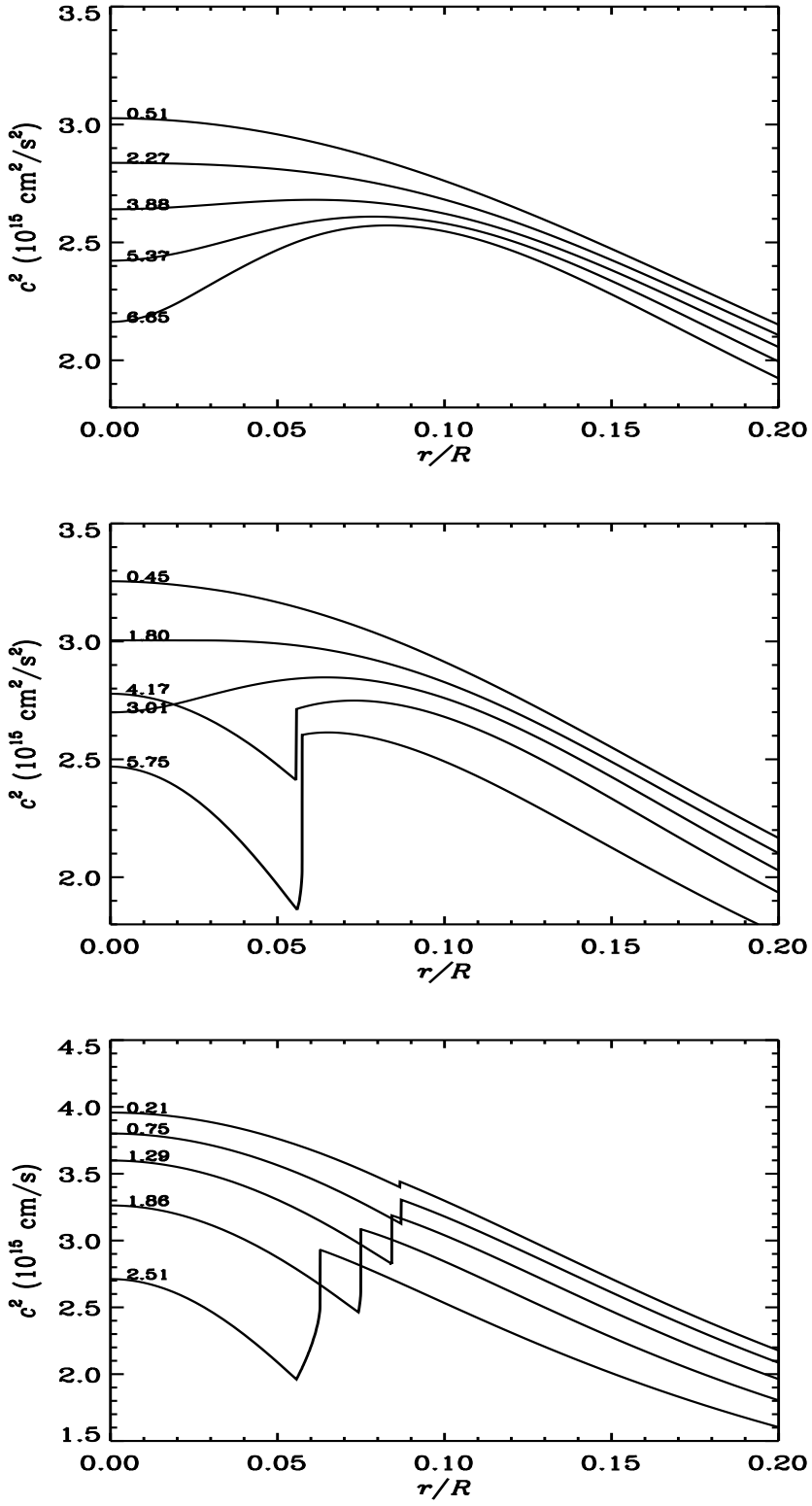

Figure 4.11: The sound-speed profile in the inner layers of a $M = 1.0\,\mathrm{M}_\odot$ (upper panel), $M = 1.1\ \mathrm{M}_\odot$ (middle panel) and $M = 1.4\,\mathrm{M}_\odot$ (lower panel) with different ages. The numbers at the beginning of the curves indicate the age of the models in Gyr. These models were computed with solar metallicity and assuming overshoot from the convective core of $\alpha_{\mathrm{OV}} = 0.1$.

and the $1.1\,M_\odot$ models with high metallicity, $Z/X = 0.0787$ all have a convective core. Models with $M \geq 1.2\,M_\odot$ all have convective cores and show a discontinuity of the sound speed (Figure 4.11, lower panel).

Figure 4.12, upper panel, shows the maximum absolute derivative of the quantity $6\Delta\nu\, dr_{0213}$ computed in the frequency region of constant slope for all the models within our sequence of evolutionary tracks as a function of the mass of the models. Models without a convective core are shown in red. The lower panel of Figure 4.12 shows the size of the jump of the sound-speed squared, $\delta c^2/c^2$, as a function of the mass of the models. Note that no stars of $M = 1.0\,M_\odot$ are shown in this plot, because these stars do not have convective cores, hence no discontinuity in the sound speed. From this figure, and for the physics considered in the models, we can see that the maximum absolute derivative of the quantity $6\Delta\nu\, dr_{0213}$ is no higher than ∼0.008, independently of the mass of the models. This maximum value of ∼0.008 is, in turn, associated to a maximum value for $\delta c^2/c^2$ of ∼0.4, the latter being determined by the change of the chemical composition (hence, in the mean molecular weight) at the discontinuity. In the same figure, upper panel, we can also see that models with $|\,\mathrm{d}\,(6\Delta\nu\, dr_{0213})/\mathrm{d}\nu\,| \gtrsim 0.002$ all have a convective core, while models with $|\,\mathrm{d}\,(6\Delta\nu\, dr_{0213})/\mathrm{d}\nu\,| \lesssim 0.002$ may or may not have a convective core, depending on the mass. Therefore, for a given observation of a star, if we find that $|\,\mathrm{d}\,(6\Delta\nu\, dr_{0213})/\mathrm{d}\nu\,| \gtrsim 0.002$, we can say with confidence that the star has a convective core.

Unfortunately, the frequency region where the maximum absolute slope is computed is not always in the range of the observed frequencies. For instance, for the main-sequence solar-like pulsators observed by the *Kepler* satellite, we note that approximately a dozen of radial orders, centred on $\nu_{\max}$, are observed. Moreover, no frequencies above the cutt-off frequency, ν_c, are expected to be observed. To illustrate the impact of these observational limitations, we show in Figure 4.13 again the plot present in the upper panel of Figure 4.12 but considering only models for which the frequency region of maximum slope is between $\nu_{max} - 8\Delta\nu$ and $\nu_{max} + 8\Delta\nu$ (upper panel) or between ν_{max} and ν_c (lower panel). The different metallicities considered in the models are shown with different symbols. Models with $|\,\mathrm{d}\,(6\Delta\nu\, dr_{0213})/\mathrm{d}\nu\,| \gtrsim 0.003$ and for which the frequency region of the maximum slope is between $\nu_{max} - 8\Delta\nu$ and $\nu_{max} + 8\Delta\nu$ all have the highest metallicity, namely $Z/X = 0.0787$.

If the $l = 3$ modes are not observed, the two diagnostic tools d_{010} and d_{020}, or their respective ratios, which consider modes of degree up to 2 should be preferred. Note, however, that these two quantities measure differently the structure of the core, hence they do not isolate the sharp structural variation in the sound speed. As a consequence, when using these two diagnostic tools one should have in mind that the effect of the whole core, and not

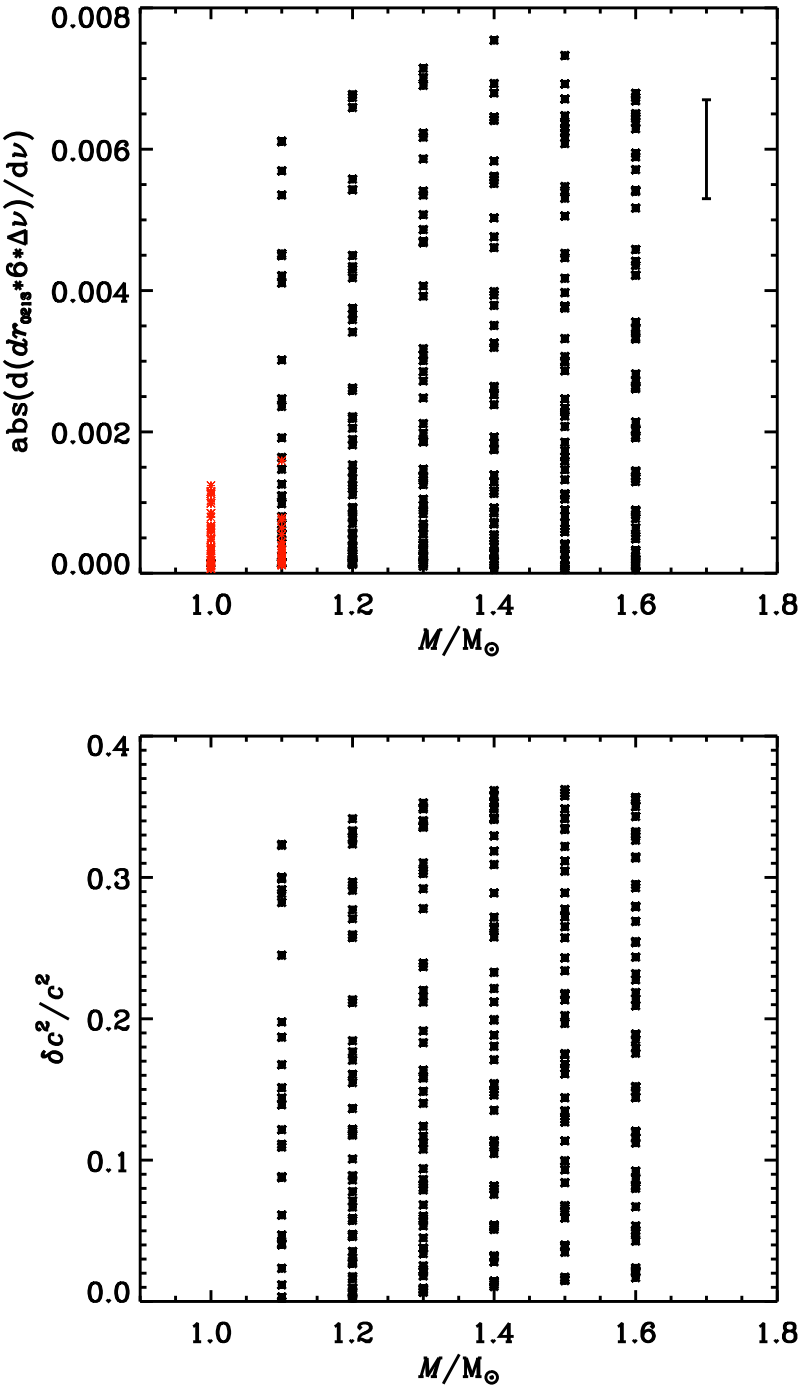

Figure 4.12: Upper panel: The symbols represent the absolute derivative of the quantity $6\Delta\nu\, dr_{0213}$ computed at maximum slope for the models with different masses and input physics considered in each evolutionary track, as a function of the mass of the model. Red stars correspond to models with no convective core. The typical error bar for the slope of $6\Delta\nu\, dr_{0213}$ is also shown in this plot. The plot in the lower panel shows, for the same models as shown in the plot of the upper panel and with convective cores, the size of the jump as a function of the mass of the model.

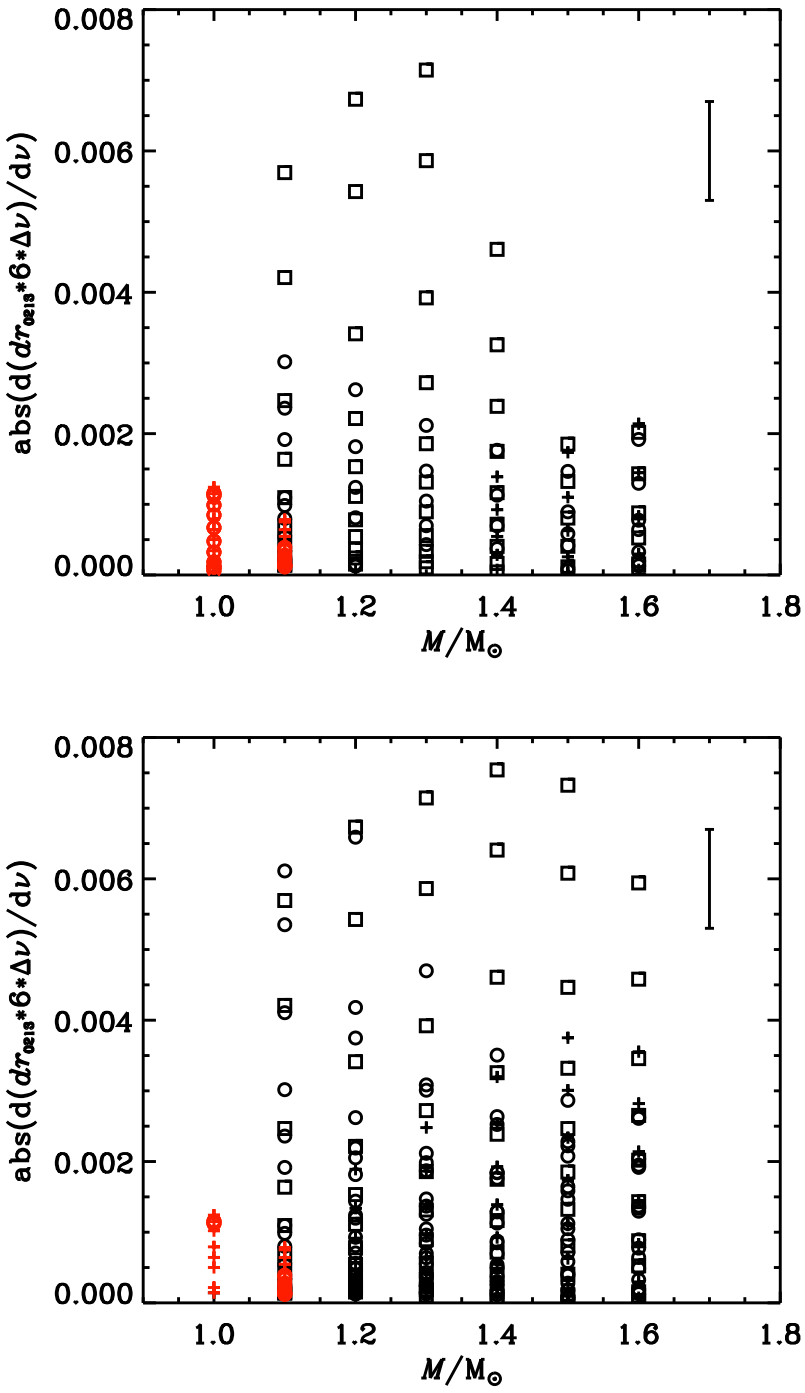

Figure 4.13: The same plot as the upper panel of Figure 4.12, but considering only models for which the frequency region of maximum slope is between $\nu_{max} - 8\Delta\nu$ and $\nu_{max} + 8\Delta\nu$ (upper panel) or between ν_{max} and ν_c (lower panel). The different symbols represent different metallicities, namely crosses represent $Z/X = 0.0079$, circles represent $Z/X = 0.0245$ and squares represent $Z/X = 0.0787$. In red are shown the models with no convective core.

only the discontinuity, is present. Nevertheless, it is interesting to see that when analysing the slopes of $\Delta\nu\, r_{02}$ and $\Delta\nu\, r_{010}$ we obtain similar results as the ones previously mentioned for the diagnostic tool dr_{0213}. We verified that models with $|\,\mathrm{d}\,(\Delta\nu\, r_{010})/\mathrm{d}\nu| \gtrsim 0.003$ or $|\,\mathrm{d}\,(\Delta\nu\ r_{02})/\mathrm{d}\nu| \gtrsim 0.003$ all have convective cores. Moreover, within these models, those for which the measured slope is in the expected observed frequency range, namely between $\nu_{max} - 8\Delta\nu$ and $\nu_{max} + 8\Delta\nu$, are the most metallic ones.

So, in summary, for the diagnostic tools considered, we are confident that a detection of a slope with absolute value larger than ~0.003 is a strong indication of the presence of a convective core. Also, for relatively low masses, these are expected to be observed preferentially in high metallicity stars.

For the models with a convective core and for which we computed the slopes of the diagnostic tools and the size of the jump in c^2, we checked if a relation between these two quantities exists. In Figure 4.14, upper panel, we show the relation between the slopes computed for the diagnostic tool $6\Delta\nu\, dr_{0213}$ and the relative size of the jump in the sound speed squared, $\delta c^2/c^2$. This plot shows a strong dependence of the slopes on the size of the jump, as expected from the work of Cunha & Brandão (2011) and expression 4.1.9.

In the same figure, in the middle and lower panels, we show the same relation, but for the quantities $\Delta\nu\, r_{010}$ and $\Delta\nu\, r_{02}$, respectively. Although the two latter diagnostic tools do not isolate the effect of the jump in the sound speed, the similarity with the plot for the first diagnostic tool indicates that their slopes are strongly affected by this discontinuity.

By inspecting these plots, a relatively large spread is found at larger values of $\delta c^2/c^2$, thus, larger ages. For the younger stars, with $\delta c^2/c^2 \lesssim 0.2$, the relation was found not to depend significantly on the mass, core overshooting, or metallicity, at least for the physics that we considered in our set of models. However, at latter stages, that is no longer the case. To illustrate this, we show, in Figure 4.15, the dependence of the relation between $\mathrm{d}(6\Delta\nu\, dr_{0213})/\mathrm{d}\nu$ and $\delta c^2/c^2$ on the metallicty. In Figure 4.16 we show the dependence of the same relation on the overshooting and, finally, in Figure 4.17 we show the dependence on the mass. A dependence of the relation on metallicity and overshoot clearly emerges as the stars approach the TAMS. On the other hand, no clear dependence on stellar mass is seen even at the latest stages considered.

From these results we can say that, in principle, it is possible, for particular stars, to get a measure of the size of the jump in the sound speed from the analysis of the observed oscillation frequencies. Such measure, in turn, can in principle be related to the evolutionary state of the star. To test this possibility, we inspected directly the relation between the slopes of the different diagnostic tools and the fraction of evolution (t/t_{TAMS}) along the main-

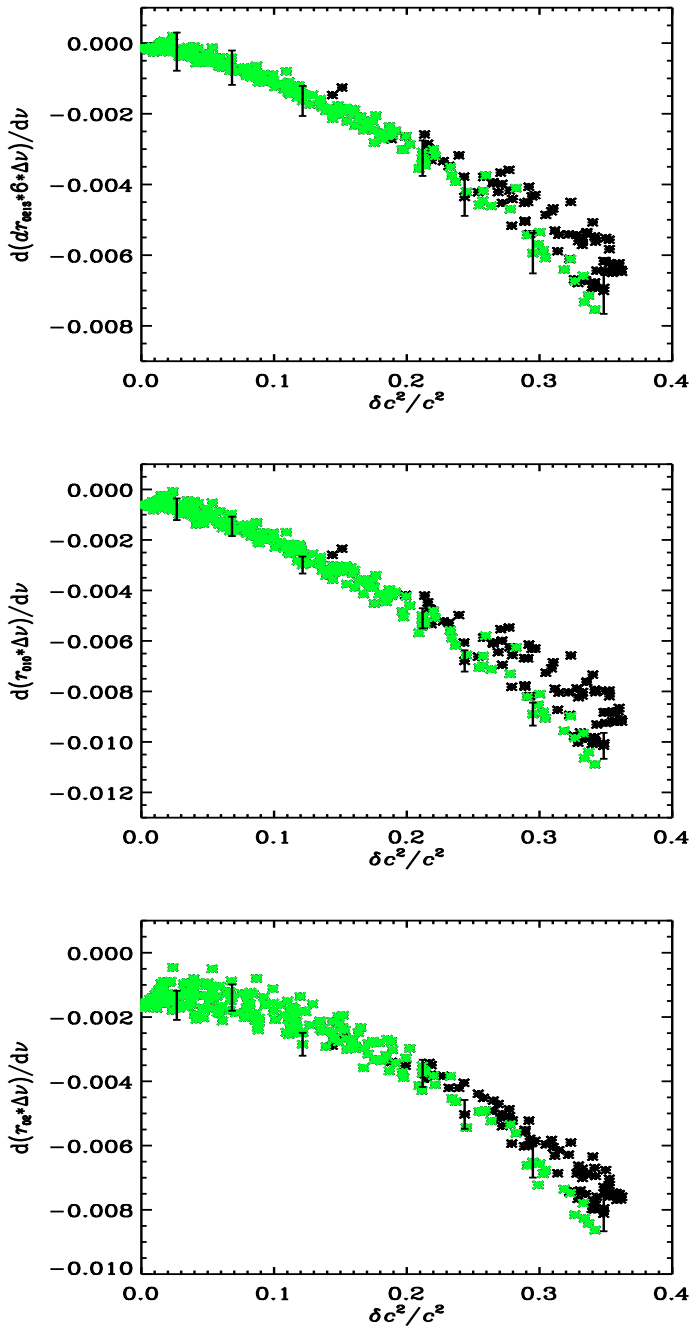

Figure 4.14: The slopes of the diagnostic tool $6\Delta\nu\, dr_{0213}$ (upper panel), $\Delta\nu\, r_{010}$ (middle panel) and $\Delta\nu\, r_{02}$ (lower panel) as a function of the relative size of the sound-speed squared, $\delta c^2/c^2$. Each point represented by a star symbol corresponds to one model of our grids for which we have computed both the slopes and the size of the discontinuity of c^2. Green stars represent the models for which the slope of the diagnostic tools was measured between $\nu_{\rm max}$ and ν_c. The error bars shown were computed for some of the models of our grid.

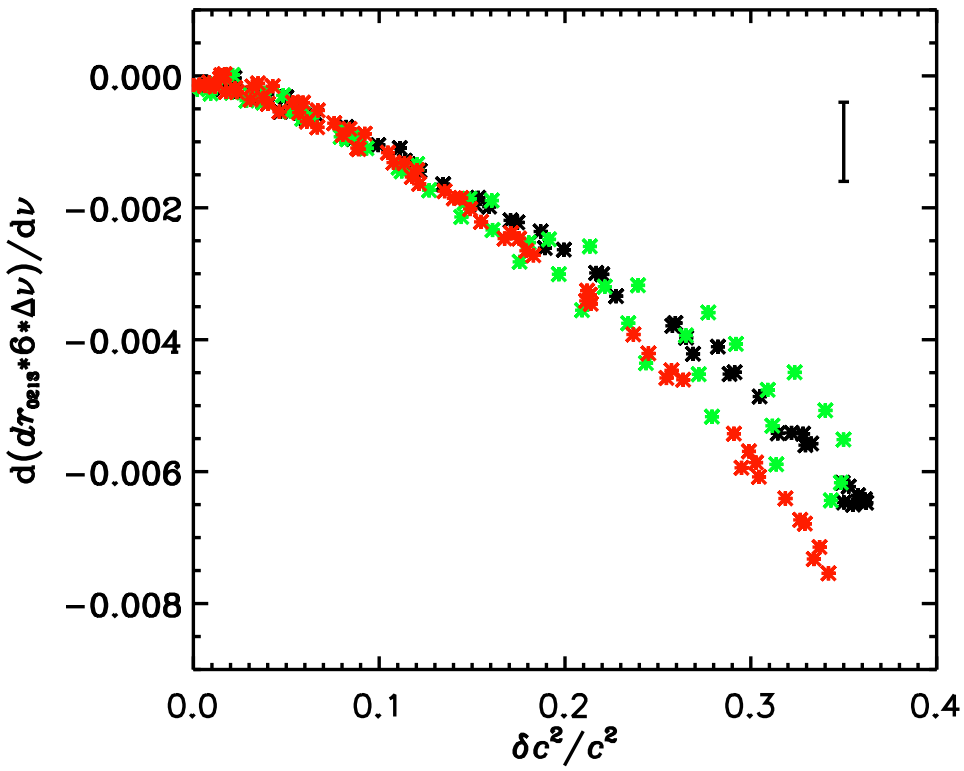

Figure 4.15: The slope of the diagnostic tool, $6\Delta\nu\, dr_{0213}$ as a function of the relative size of the jump in the sound-speed squared, $\delta c^2/c^2$. The black stars represent models with solar metallicity, $Z/X = 0.0245$, the green stars represent models with $Z/X = 0.0079$, and the red stars represent models with $Z/X = 0.0787$. The models have $\alpha_{\rm OV} = 0.1$. The typical error bar for $\mathrm{d}(dr_{0213}6\Delta\nu)/\mathrm{d}\nu$ is shown in the upper right corner of the plot.

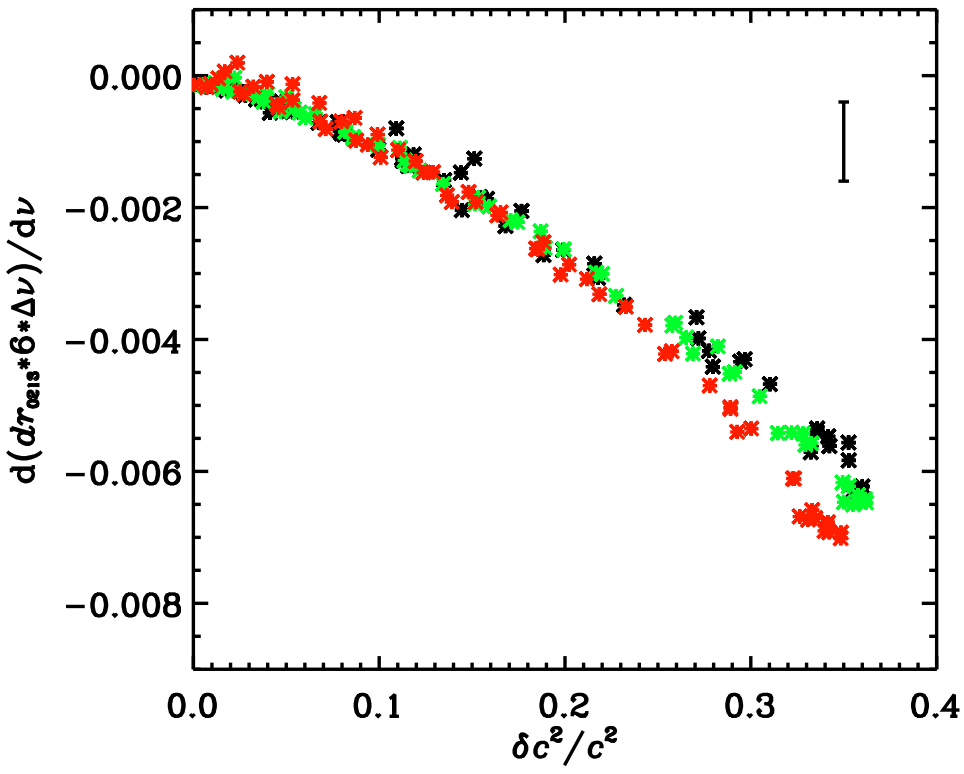

Figure 4.16: The same as in Figure 4.15 but here the black stars represent models without overshooting, $\alpha_{\rm OV} = 0.0$, the green stars represent models with $\alpha_{\rm OV} = 0.1$, and the red stars represent models with $\alpha_{\rm OV} = 0.2$. The models have $Z/X = 0.0245$. The typical error bar for $\mathrm{d}(dr_{0213}6\Delta\nu)/\mathrm{d}\nu$ is shown in the upper right corner of the plot.

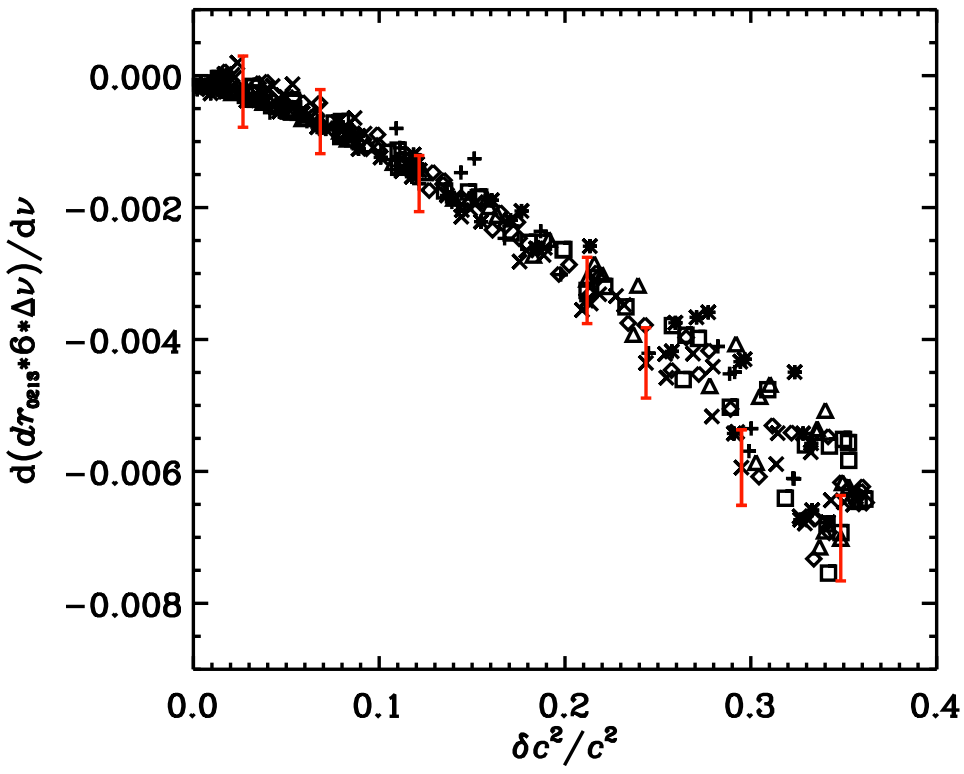

Figure 4.17: The same as in Figure 4.15 but here the different symbols correspond to different values of the mass, namely $M = 1.1\,\mathrm{M}_\odot$ are represented by crosses, $M = 1.2\,\mathrm{M}_\odot$ by stars, $M = 1.3\,\mathrm{M}_\odot$ by triangles, $M = 1.4\,\mathrm{M}_\odot$ by squares, $M = 1.5\,\mathrm{M}_\odot$ by diamonds and $M = 1.6\,\mathrm{M}_\odot$ by X. The error bars for $\mathrm{d}(dr_{0213}6\Delta\nu)/\mathrm{d}\nu$ are shown for some models.

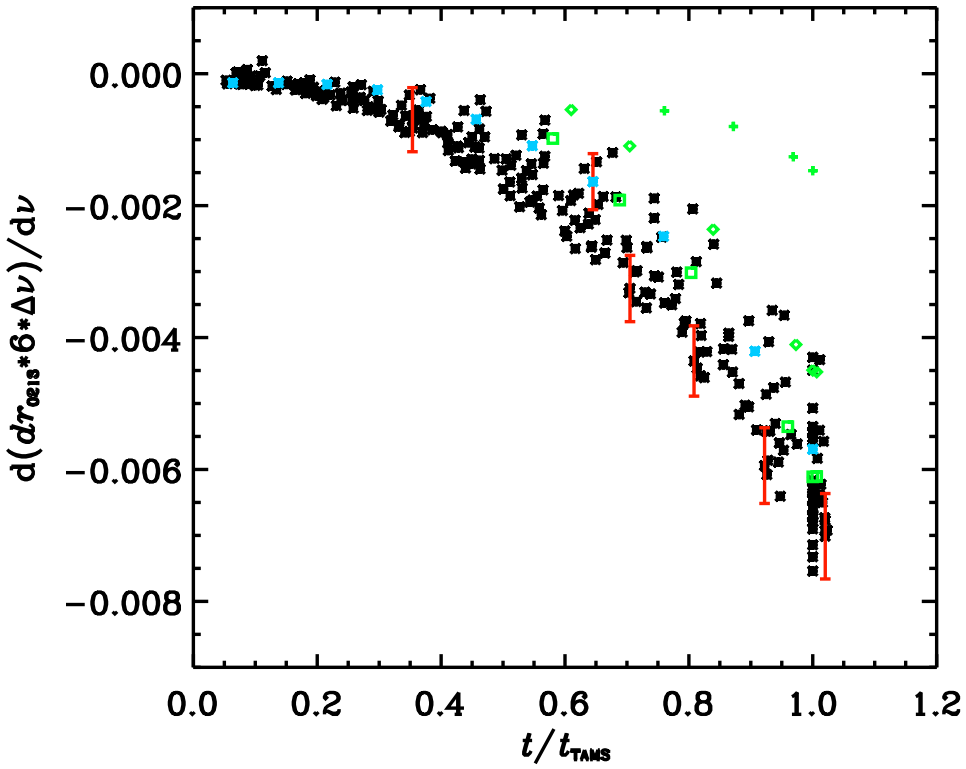

Figure 4.18: The slope of the diagnostic tool, $6\Delta\nu\ dr_{0213}$ as a function of the fraction of stellar evolution, $t/t_{\rm TAMS}$, for all models of our grid that have a convective core. These are all models with $1.2 \leq M \leq 1.6\,\mathrm{M}_{\odot}$ and models with $M = 1.1\,\mathrm{M}_{\odot}$ with metallicities $Z/X = 0.0245$ (green symbols) and $Z/X = 0.0787$ (light blue symbols). The different symbols in green represent different values for the overshoot parameter, namely $\alpha_{\rm OV} = 0.0$ (crosses), $\alpha_{\rm OV} = 0.1$ (diamonds) and $\alpha_{\rm OV} = 0.2$ (squares).

sequence phase of a star. By fraction of evolution we mean the ratio between the age of a star at a given evolutionary stage, t, in the main-sequence and the age of a star within the same evolutionary track but at the TAMS, $t_{\rm TAMS}$. We considered the stellar fraction of evolution and not the stellar age alone since the latter is strongly dependent on the stellar mass. Figure 4.18 shows, for all models with a convective core, the slopes of the diagnostic tool $6\Delta\nu\,dr_{0213}$ as a function of the fraction of main-sequence stellar evolution, $t/t_{\rm TAMS}$. By inspecting this figure, we see a large spread in the slopes at the higher evolution fractions, namely at $t/t_{\rm TAMS} \gtrsim 0.6$. This is due to the fact that models with $M = 1.1\,\mathrm{M}_{\odot}$, solar metallicity and $\alpha_{\rm OV} = 0.0$ have a very small central convective region and, therefore, only a small discontinuity in the chemical composition at the edge of that region. This is illustrated in Figure 4.19 where we compare the cases of models with $M = 1.1\,\mathrm{M}_{\odot}$ and solar metallicity

and diferent values for the overshoot parameter. Moreover, we find that models with $M = 1.2\,M_\odot$ and no overshooting still have a relatively small convective core, hence a slope still smaller than that of higher mass models at the later stages of their evolution. Figure 4.20, upper panel, shows the same plot as in Figure 4.18 but for models with $M \geq 1.3 M_\odot$ only. The dispersion seen in this case is significantly smaller than in Figure 4.18. Figure 4.20, middle and lower panels show, respectively, the slopes of the diagnostic tools $\Delta\nu\, r_{010}$ and $\Delta\nu\, r_{02}$, as a function of the fraction of evolution, for the models with $M \geq 1.3\,M_\odot$.

In summary, Figure 4.20 shows that for relatively massive solar-like pulsators ($M \geq 1.3\,M_\odot$), one may set constraints to the fraction of evolution along the main-sequence by inspecting the slopes of the diagnostic tools considered here, in particular the dr_{0213} and the r_{010}.

For relatively evolved stars such constraints are, however, limited to metallic stars, since only for those one may observe the slope at its maximum.

An interesting question to ask is what do models with a similar relative size of the jump of the sound-speed squared have in common. If we plot, e.g., the models for which $\delta c^2/c^2 = 0.330 \pm 0.005$, in the HR diagram, as shown in Figure 4.21, upper panel, we see that they are all in the same evolutionary stage, namely at the TAMS. They all have $0.90 < 1 - X_c < 0.96$. This shows that $\delta c^2/c^2$ can potentially be used to identify the TAMS. In the lower panel of this figure we show again the slope of the diagnostic tool $6\Delta\nu\, dr_{0213}$ as a function of $\delta c^2/c^2$, where the black stars symbols correspond to the models considered in the upper panel. A large spread in the slope is seen in this relation. Nevertheless, if we consider that among these only the stars with high metallicities may have this large slope in $6\Delta\nu\, dr_{0213}$ observed, we can confidently say that the observation of a slope in this quantity of $\sim$0.007 is indicative that the star has reached the TAMS.

4.4 Conclusions

We used four seismic diagnostic tools, namely r_{01}, r_{10}, r_{02}, and the diagnostic tool, dr_{0213} to study the cores of models of different masses, metallicities and convective core overshoots, and different evolutionary states in the main sequence. Note that, in practice, we analysed the r_{01} and r_{10} together, referring to it as r_{010}.

We verified that there is a maximum absolute value for the computed frequency derivatives of all diagnostic tools, which, in turn, is related to the maximum value achieved by the relative size of the jump in the sound-speed squared. The maximum absolute values that we obtained for the frequency slopes of $6\Delta\nu\, dr_{0213}$, $\Delta\nu\, r_{010}$ and $\Delta\nu\, r_{02}$ were $\sim$0.007, $\sim$0.011

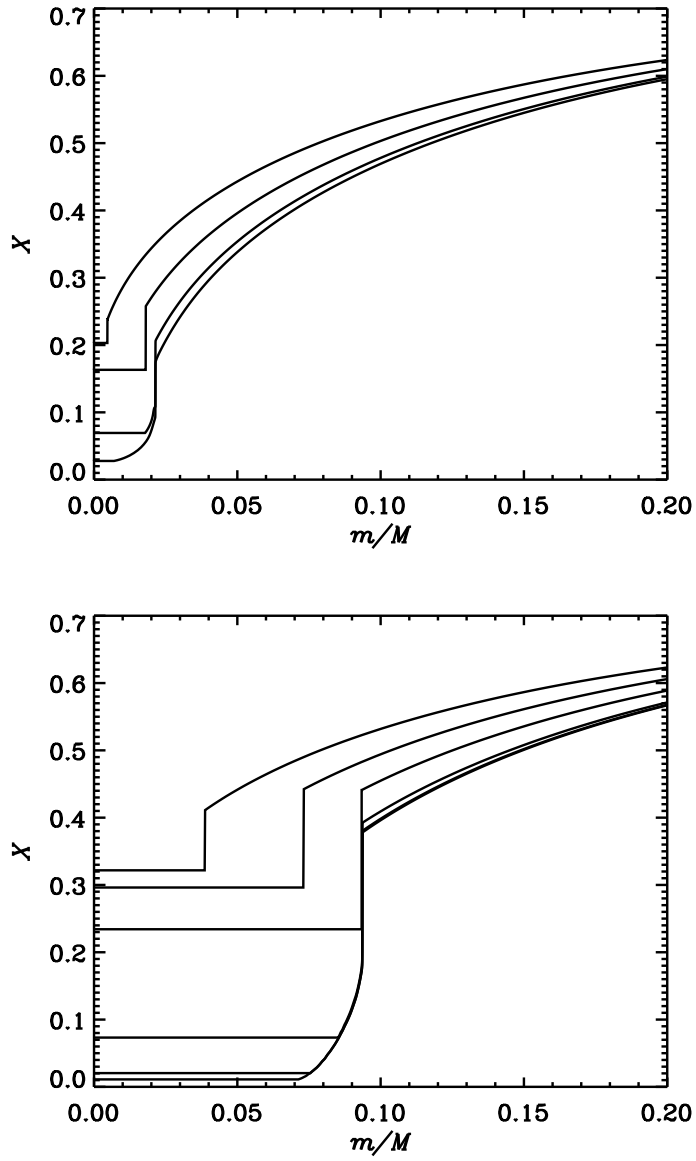

Figure 4.19: The hydrogen profile of a $M = 1.1\,\mathrm{M}_\odot$ model with $Z/X = 0.0245$ and with $\alpha_{\mathrm{OV}} = 0.0$ (upper panel) and a $M = 1.1\,\mathrm{M}_\odot$ model with $Z/X = 0.0245$ and with $\alpha_{\mathrm{OV}} = 0.2$ (lower panel). The different curves correspond to different stages of evolution. Only models with a convective core are shown.

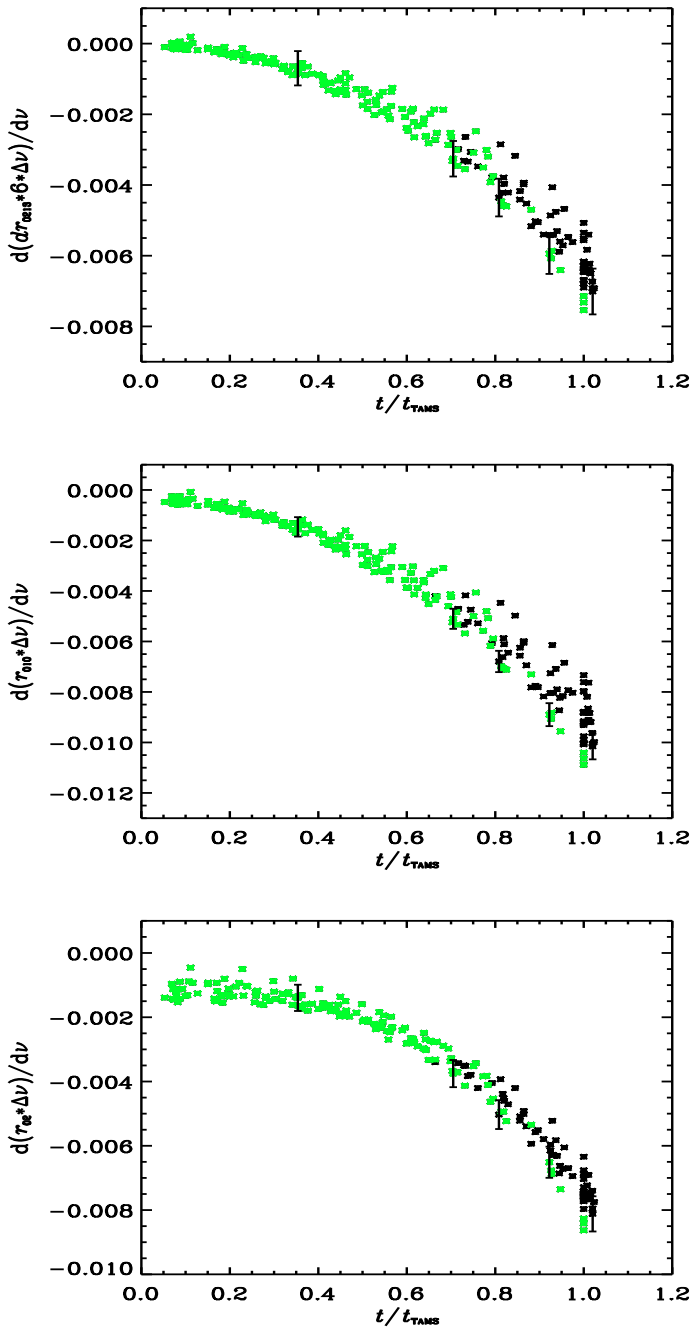

Figure 4.20: Upper panel: The same as in Figure 4.18 but here only considering models with $M \geq 1.3\,M_{\odot}$. The same models are shown in the middle and lower panels for the slopes of the diagnostic tools $\Delta\nu\, r_{010}$ and $\Delta\nu\, r_{02}$, respectively. Green symbols represent those models for which the derivative of the diagnostic tools has its maximum between ν_{max} and ν_c.

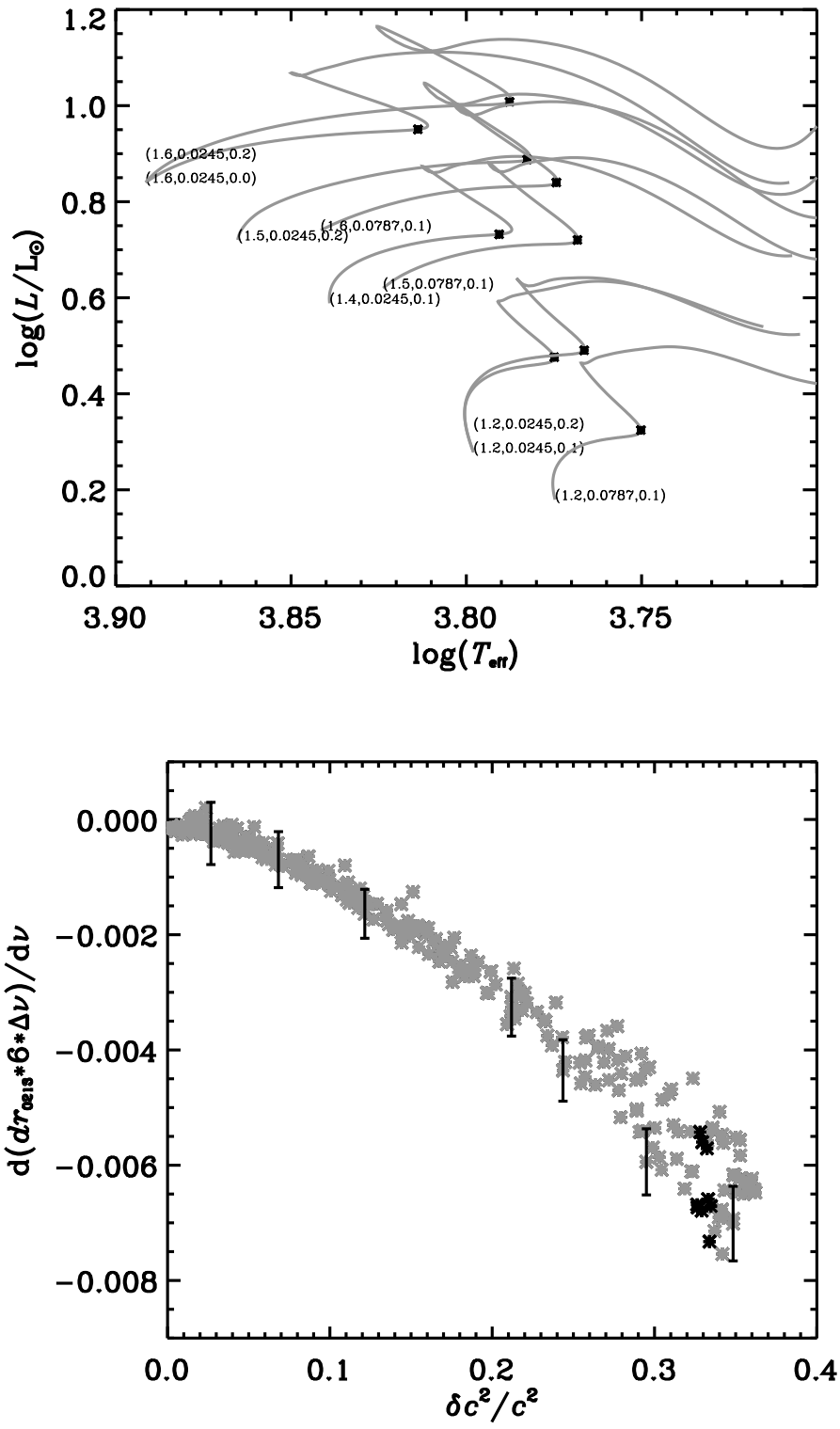

Figure 4.21: Upper panel: the position in the HR diagram of models that have a common $\delta c^2/c^2 = 0.330 \pm 0.005$ are represented by the black star symbol. Also shown are the evolutionary tracks that correspond to these models. The brackets in the beginning of each track show the value of its mass, in solar units, Z/X and $\alpha_{\rm OV}$, respectively. Lower panel: the values of the slopes of the $6\Delta\nu\ dr_{0213}$ for these models (black stars).

and ∼0.009, respectively. Moreover, we found that models with $|\,\mathrm{d}\,(6\Delta\nu\, dr_{0213})/\mathrm{d}\nu\,| \gtrsim 0.002$, $|\,\mathrm{d}\,(\Delta\nu\, r_{010})/\mathrm{d}\nu\,| \gtrsim 0.003$ and $|\,\mathrm{d}\,(\Delta\nu\, r_{02})/\mathrm{d}\nu\,| \gtrsim 0.003$ all have convective cores. Within these models, those for which the measured slope is in the expected observed frequency range, namely between $\nu_{max} - 8\Delta\nu$ and $\nu_{max} + 8\Delta\nu$, are the most metallic ones, with $Z/X = 0.0787$. Models with $|\,\mathrm{d}\,(6\Delta\nu\, dr_{0213})/\mathrm{d}\nu\,| \lesssim 0.002$, $|\,\mathrm{d}\,(\Delta\nu\, r_{010})/\mathrm{d}\nu\,| \lesssim 0.003$ and $|\,\mathrm{d}\,(\Delta\nu\, r_{02})/\mathrm{d}\nu\,| \lesssim 0.003$, may or may not have a convective core, depending on the mass.

We also verified that there is a strong dependence of the frequency slopes of all diagnostic tools on the relative size of the jump in the sound-speed squared, $\delta c^2/c^2$. It is, therefore, in principle, possible to use the frequency of the modes of degree $l \leq 2$ to infer about the relative size of the sound speed, $\delta c^2/c^2$.

We verified that for models with a convective core there is a relation between the maximum slopes of the diagnostic tools and the fraction of stellar main-sequence evolution, t/t_{TAMS}. This relation is stronger for models with $M \geq 1.3\,\mathrm{M}_{\odot}$. For these masses one may expect to be able to use the slopes of dr_{0213} or r_{010} to infer about t/t_{TAMS}, at least for stars in which the maximum slope is within the observable range.

Finally, we found that when the absolute slope of $6\Delta\nu\, dr_{0213}$ is as big as ∼0.007 then star is at the TAMS.

Chapter 5

Concluding remarks

This dissertation concerned the study of two classes of pulsating stars, namely the rapidly oscillating A peculiar (roAp) stars and the solar-like pulsators.

RoAp stars are a class of pulsators potentially very interesting for asteroseimic studies. They are classical pulsators, with pulsation amplitudes larger than those observed for the solar-like pulsators, which makes them easier to detect. They pulsate in low-degree, high overtone, non-radial acoustic (p-) modes. Moreover, their oscillations are affected by intense magnetic fields. In principle, asteroseismology of roAp stars makes it possible to probe their internal structure and magnetic fields. However, detailed asteroseimic studies of roAp stars have in some cases been limited because the fundamental parameters are poorly known. An example is the large uncertainty associated with the determination of the effective temperature of these stars, spanning 500 K or more. This large range, may be explained, in part, by the chemical peculiarities and by the strong magnetic fields present in roAp stars.

The effective temperature of a star can be obtained from the combination of its bolometric flux and angular diameter. In this work, we have presented a method to calculate the bolometric flux of roAp stars. Rather than using the bolometric corrections available in the literature, we computed the bolometric flux of these stars directly from their observed spectra, calibrated in flux, together with the synthetic spectra of the Kurucz model atmospheres that matches the photometric data and/or interpolations in the regions for which no observed spectra were available. The need for such an analysis results from the fact that the available bolometric corrections for normal stars are not suitable for roAp stars. We have applied this method to two roAp stars, namely β CrB and γ Equ, for which interferometric observations of their angular diameters were available. Both stars are binary, so we also estimated the contribution of the secondary to the bolometric flux of the binary. We conclude that our

method to determine the effective temperature of roAp stars is less model dependent than those derived from photometric indices for which bolometric corrections are needed. The main difficulties associated with the method that we used to compute the bolometric flux, and that result in an increasing uncertainty on its determination, are the fact that the full spectrum of the star is not always available and that the data available in the literature for the secondary star of these binary systems is lacking.

Regarding the modelling of solar-like pulsators, I present asteroseimic studies performed on three targets, namely β Hyi, KIC 10273246, and 16 Cyg. These are three examples for which the observed individual oscillation frequencies can be used together with non-seismic data to constrain a star's global parameters, with high precision. We used the stellar evolutionary code, ASTEC, to compute a grid of evolutionary models and for those that lay inside $1-$ or $3-\sigma$ uncertainty for the non-seismic data, their oscillation frequencies were computed with the ADIPLS code. We then compared the individual model frequencies to the observed ones in order to find the best matching model of the star, and hence, to infer about its global properties.

Care should be taken when using the individual frequencies to model solar-like pulsators since they are strongly affected by the stellar near-surface layers, which we still fail in properly model. An empirical correction has been proposed by Kjeldsen et al. (2008) that corrects the shift that exists between the frequencies of the model that best reproduces the interior of the Sun and its observed frequencies. The authors argue that when modelling stars other than the Sun, a shift between the model frequencies and the observed ones may also exist, and that their proposed correction may be applied to such stars. In the present work, we aimed at testing this empirical correction. We found that it seems to work rather well for β Hyi and for 16 Cyg, but it did not work so well for KIC 10273246, which is a star hotter than the former two. Nevertheless, for all the three stars under study we found the minimum of the $\chi^2_{\rm seis}$ function, that evaluates the difference between the model and observed frequencies, to be greater than one. This may suggest that either the observational uncertainties associated to the observed frequencies are underestimated or that the models fail in reproducing the data even when the empirical surface corrections are applied. As the data is becoming more precise, thanks to space missions such as *Kepler*, improvements to the physics of the models are needed, such as the description of convection within the surface layers of stars that show a convective envelope.

In addition, some specific features are seen in the oscillation spectra of β Hyi and KIC 10273246, associated to the so-called mixed modes. We show that these modes are useful to constrain the stellar age, but that they also affect the results regarding the other global parameters of the star.

Finally, in this thesis, we analysed the effect that the presence of a small convective core in main-sequence solar-like pulsators has on their oscillation frequencies. We also analysed the relations that may exist between this effect (or signature) and some of the properties of the convective core, and hence the evolutionary state of the stars. Moreover, we studied the dependence of these relations on the stellar mass and physical parameters.

We computed main-sequence evolutionary tracks with masses between 1.0 and 1.6 $M_\odot$ using the ASTEC code, and for some selected models within each track we computed their oscillation frequencies with the ADIPLS code. Using these model frequencies we constructed three diagnostic tools suggested in the literature, namely, dr_{0213}, r_{01}, r_{10} and r_{02}, that use mode degrees, l, up to 3. In practice, we considered r_{01} and r_{10} together denoting it by r_{010}.

The presence of a growing convective core in main-sequence solar-type pulsators causes a discontinuity in the chemical composition, hence, a discontinuity in the sound-speed profile at the edge of the core. Moreover, a retreating convective core also leaves a discontinuity in the chemical composition and, consequently, a discontinuity in the sound-speed profile.

We verified that there is a relation between the frequency derivatives of all of the above mentioned diagnostic tools and the relative size of the jump in the sound-speed squared. Although the only studied diagnostic tool that is capable of isolating the signature of the edge of the core is dr_{0213}, we verified that the other two diagnostic tools, namely r_{010} and r_{02} are also affected by the presence of the convective core. This is an important result since not always modes with degree up to 3 are available. We found that there is a maximum absolute value for the frequency derivatives of all of the diagnostic tools under study, which, in turn is related to a maximum value achieved by the relative size of the jump in the sound-speed squared. Moreover, we found that models for which the absolute derivatives of the diagnostic tools are above a given threshold, ~0.003, all have a convective core.

In our work, the frequency derivatives of the diagnostic tools were measured in a frequency region centred in the frequency for which the derivative absolute value is maximum. Unfortunately, this region may not always be within the range of the observed frequencies of real stars. With this in mind, we inspected the models for which the frequency derivatives were computed within the observed frequency range, that we chose, based on the data from the *Kepler* satellite, to be between $\nu_{\max} \pm 8\Delta\nu$, and verified that those that have the derivatives of the diagnostic tool above ~0.003 are the most metallic ones of our grid.

Regarding the stellar evolutionary state of a star measured in terms of the fraction of main-sequence stellar evolution, $t/t_{\rm TAMS}$, we found it to be related to the maximum slope of the diagnostic tools, this relation being stronger for stars with $M \geq 1.3\,M_\odot$. Also, we found that if the maximum absolute derivative of the diagnostic tool $6\Delta\nu\, dr_{0213}$ is as big as ~0.007 then

we can confidently say that the star is at the TAMS.

We must note that these conclusions were obtained based on models with a given physics. It would be interesting to perform a similar analysis by including different physics to the models, in particular diffusion. Moreover, with the unprecedented quality data that we are obtaining from the *Kepler* satellite, we hope to apply our analysis to the observations of real stars.

Bibliography

Abt, H. A. 1985, ApJS, 59, 95

Adelberger, E. G., Austin, S. M., Bahcall, J. N., et al. 1998, Reviews of Modern Physics, 70, 1265

Aerts, C., Christensen-Dalsgaard, J., & Kurtz, D. W. 2010, Asteroseismology, Springer, Heidelberg

Aizenman, M., Smeyers, P., & Weigert, A. 1977, A&A, 58, 41

Alekseeva, G. A., Arkharov, A. A., Galkin, V. D., et al. 1996, Baltic Astronomy, 5, 603

Ammons, S. M., Robinson, S. E., Strader, J., et al. 2006, ApJ, 638, 1004

Angulo, C., Arnould, M., Rayet, M., et al. 1999, Nuclear Physics A, 656, 3

Antoci, V., Handler, G., Campante, T. L., et al. 2011, NAT, 477, 570

Appourchaux, T., Michel, E., Auvergne, M., et al. 2008, A&A, 488, 705

Arentoft, T., Kjeldsen, H., & Bedding, T. R. 2009, in Astronomical Society of the Pacific Conference Series, Vol. 416, Astronomical Society of the Pacific Conference Series, ed. M. Dikpati, T. Arentoft, I. González Hernández, C. Lindsey, & F. Hill, 347

Baglin, A., Michel, E., Auvergne, M., & COROT Team. 2006, in ESA Special Publication, Vol. 624, Proceedings of SOHO 18/GONG 2006/HELAS I, Beyond the spherical Sun

Bahcall, J. N., Pinsonneault, M. H., & Basu, S. 2001, ApJ, 555, 990

Balmforth, N. J. & Gough, D. O. 1990, ApJ, 362, 256

Basu, S. & Antia, H. M. 2008, Phys. Rep., 457, 217

Batalha, N. M., Borucki, W. J., Koch, D. G., et al. 2010, ApJL, 713, L109

Bazot, M., Campante, T. L., Chaplin, W. J., et al. 2012, A&A, 544, A106

Bazot, M., Ireland, M. J., Huber, D., et al. 2011, A&A, 526, L4

Bedding, T. R. & Kjeldsen, H. 2003, Publications of the Astronomical Society of Australia, 20, 203

Bedding, T. R., Kjeldsen, H., Arentoft, T., et al. 2007, ApJ, 663, 1315

Bedding, T. R., Kjeldsen, H., Campante, T. L., et al. 2010, ApJ, 713, 935

Belkacem, K., Goupil, M. J., Dupret, M. A., et al. 2011, A&A, 530, A142

Bergeron, J. & Monnet, G., eds. 2002, Scientific Drivers for ESO Future VLT/VLTI Instrumentation

Bessell, M. S. 1999, PASP, 111, 1426

Bessell, M. S. 2005, ARA&A, 43, 293

Bessell, M. S., Castelli, F., & Plez, B. 1998, A&A, 333, 231

Bevington, P. R. & Robinson, D. K. 2003, Data reduction and error analysis for the physical sciences

Blackwell, D. E. & Lynas-Gray, A. E. 1998, A&AS, 129, 505

Böhm-Vitense, E. 1958, Zeitschrift fur Astrophysik, 46, 108

Borucki, W. J., Koch, D., Basri, G., et al. 2010, Science, 327, 977

Boyajian, T. S., McAlister, H. A., van Belle, G., et al. 2012, ApJ, 746, 101

Broomhall, A.-M., Chaplin, W. J., Davies, G. R., et al. 2009, MNRAS, 396, L100

Brown, T. M., Christensen-Dalsgaard, J., Weibel-Mihalas, B., & Gilliland, R. L. 1994, ApJ, 427, 1013

Brown, T. M., Gilliland, R. L., Noyes, R. W., & Ramsey, L. W. 1991, ApJ, 368, 599

Brown, T. M., Latham, D. W., Everett, M. E., & Esquerdo, G. A. 2011, AJ, 142, 112

Bruntt, H., Kervella, P., Mérand, A., et al. 2010, A&A, 512, A55

Bruntt, H., North, J. R., Cunha, M., et al. 2008, MNRAS, 386, 2039

Burgers, J. M. 1969, Flow Equations for Composite Gases, ed. Burgers, J. M.

Burnashev, V. I. 1985, Abastumanskaia Astrofizicheskaia Observatoriia Biulleten, 59, 83

Campante, T. L., Handberg, R., Mathur, S., et al. 2011, A&A, 534, A6

Canuto, V. M. 1997, ApJL, 489, L71

Canuto, V. M., Goldman, I., & Mazzitelli, I. 1996, ApJ, 473, 550

Canuto, V. M. & Mazzitelli, I. 1991, ApJ, 370, 295

Casagrande, L. 2007, in Astronomical Society of the Pacific Conference Series, Vol. 374, From Stars to Galaxies: Building the Pieces to Build Up the Universe, ed. A. Vallenari, R. Tantalo, L. Portinari, & A. Moretti, 71

Caughlan, G. R. & Fowler, W. A. 1988, Atomic Data and Nuclear Data Tables, 40, 283

Chaplin, W. J. & Basu, S. 2008, Sol. Phys., 251, 53

Chaplin, W. J., Bedding, T. R., Bonanno, A., et al. 2011, ApJL, 732, L5

Chaplin, W. J., Elsworth, Y., Isaak, G. R., Miller, B. A., & New, R. 1999, MNRAS, 308, 424

Christensen-Dalsgaard, J. 1982, Advances in Space Research, 2, 11

Christensen-Dalsgaard, J. 1984, in Space Research in Stellar Activity and Variability, ed. A. Mangeney & F. Praderie, 11

Christensen-Dalsgaard, J. 2002, Reviews of Modern Physics, 74, 1073

Christensen-Dalsgaard, J. 2008a, Ap&SS, 316, 13

Christensen-Dalsgaard, J. 2008b, Ap&SS, 316, 113

Christensen-Dalsgaard, J., Dappen, W., Ajukov, S. V., et al. 1996, Science, 272, 1286

Christensen-Dalsgaard, J. & Frandsen, S. 1983, Solar Physics, 82, 165

Christensen-Dalsgaard, J., Monteiro, M. J. P. F. G., & Thompson, M. J. 1995, MNRAS, 276, 283

Christensen-Dalsgaard, J. & Thompson, M. J. 1997, MNRAS, 284, 527

Claverie, A., Isaak, G. R., McLeod, C. P., van der Raay, H. B., & Cortes, T. R. 1979, Nature, 282, 591

Cochran, W. D., Hatzes, A. P., Butler, R. P., & Marcy, G. W. 1997, ApJ, 483, 457

Cohen, M., Wheaton, W. A., & Megeath, S. T. 2003, AJ, 126, 1090

Cox, A. N., Guzik, J. A., & Kidman, R. B. 1989, ApJ, 342, 1187

Creevey, O. L., Doğan, G., Frasca, A., et al. 2012, A&A, 537, A111

Creevey, O. L., Monteiro, M. J. P. F. G., Metcalfe, T. S., et al. 2007, ApJ, 659, 616

Cunha, M. S. 2002, MNRAS, 333, 47

Cunha, M. S., Aerts, C., Christensen-Dalsgaard, J., et al. 2007, A&A Rev., 14, 217

Cunha, M. S. & Brandão, I. M. 2011, A&A, 529, A10

Cunha, M. S. & Metcalfe, T. S. 2007, ApJ, 666, 413

Cutri, R. M., Skrutskie, M. F., van Dyk, S., et al. 2003, VizieR Online Data Catalog, 2246, 0

Daeppen, W., Mihalas, D., Hummer, D. G., & Mihalas, B. W. 1988, ApJ, 332, 261

Deheuvels, S. & Michel, E. 2011, A&A, 535, A91

di Benedetto, G. P. 1998, A&A, 339, 858

Di Mauro, M. P., Christensen-Dalsgaard, J., & Paternò, L. 2003, Ap&SS, 284, 229

Doğan, G., Bonanno, A., Bedding, T. R., et al. 2010, Astronomische Nachrichten, 331, 949

Doğan, G., Brandão, I. M., Bedding, T. R., et al. 2010, Ap&SS, 328, 101

Dravins, D., Linde, P., Ayres, T. R., et al. 1993a, ApJ, 403, 412

Dravins, D., Linde, P., Fredga, K., & Gahm, G. F. 1993b, ApJ, 403, 396

Dravins, D., Lindegren, L., Nordlund, A., & Vandenberg, D. A. 1993c, ApJ, 403, 385

Dravins, D. & Nordlund, A. 1990, A&A, 228, 203

Dupret, M.-A., Goupil, M.-J., Samadi, R., Grigahcène, A., & Gabriel, M. 2006, in ESA Special Publication, Vol. 624, Proceedings of SOHO 18/GONG 2006/HELAS I, Beyond the spherical Sun

Dziembowski, W. A., Gough, D. O., Houdek, G., & Sienkiewicz, R. 2001, MNRAS, 328, 601

Eggenberger, P., Meynet, G., Maeder, A., et al. 2008, Ap&SS, 316, 43

Evans, D. S., Menzies, A., & Stoy, R. H. 1957, MNRAS, 117, 534

Fabricius, C., Høg, E., Makarov, V. V., et al. 2002, A&A, 384, 180

Faulkner, D. J. & Cannon, R. D. 1973, ApJ, 180, 435

Ferguson, J. W., Alexander, D. R., Allard, F., et al. 2005, ApJ, 623, 585

Fernandes, J. & Monteiro, M. J. P. F. G. 2003, A&A, 399, 243

Flower, P. J. 1996, ApJ, 469, 355

Fossat, E., Regulo, C., Roca Cortes, T., et al. 1992, A&A, 266, 532

Frohlich, C., Andersen, B. N., Appourchaux, T., et al. 1997, Solar Physics, 170, 1

Garcia, R. A. 2011, in Proceedings of the IX Scientific Meeting of the Spanish Astronomical Society, Highlights of Spanish Astrophysics VI, in press [arXiv:1101.0236v1]

Garhart, M. P., Smith, M. A., Turnrose, B. E., Levay, K. L., & Thompson, R. W. 1997, IUE NASA Newsletter, 57, 1

Gelly, B., Lazrek, M., Grec, G., et al. 2002, A&A, 394, 285

Gilliland, R. L., Jenkins, J. M., Borucki, W. J., et al. 2010, ApJL, 713, L160

Girardi, L., Bressan, A., Bertelli, G., & Chiosi, C. 2000, VizieR Online Data Catalog, 414, 10371

Gong, Z., Däppen, W., & Zejda, L. 2001, ApJ, 546, 1178

González-Riestra, R., Cassatella, A., & Wamsteker, W. 2001, a&a, 373, 730

Gough, D. O. 1977a, ApJ, 214, 196

Gough, D. O. 1977b, in IAU Colloq. 36: The Energy Balance and Hydrodynamics of the Solar Chromosphere and Corona, ed. B. Bonnet & P. Delache, 3–36

Gough, D. O. 1990, in Lecture Notes in Physics, Berlin Springer Verlag, Vol. 367, Progress of Seismology of the Sun and Stars, ed. Y. Osaki & H. Shibahashi, 283

Gough, D. O. 1993, in Astrophysical Fluid Dynamics - Les Houches 1987, 399–560

Gray, D. F. 2005, The Observation and Analysis of Stellar Photospheres, ed. Gray, D. F.

Gray, R. O. 2007, in Astronomical Society of the Pacific Conference Series, Vol. 364, The Future of Photometric, Spectrophotometric and Polarimetric Standardization, ed. C. Sterken, 305

Gray, R. O., Corbally, C. J., Garrison, R. F., et al. 2006, AJ, 132, 161

Grec, G., Fossat, E., & Pomerantz, M. A. 1983, Sol. Phys., 82, 55

Grevesse, N. & Noels, A. 1993, in Origin and Evolution of the Elements, ed. S. Kubono & T. Kajino, 14

Groote, D. & Kaufmann, J. P. 1983, A&AS, 53, 91

Gruberbauer, M., Saio, H., Huber, D., et al. 2008, A&A, 480, 223

Grundahl, F., Christensen-Dalsgaard, J., Arentoft, T., et al. 2009a, Communications in Asteroseismology, 158, 345

Grundahl, F., Christensen-Dalsgaard, J., Kjeldsen, H., et al. 2009b, in Astronomical Society of the Pacific Conference Series, Vol. 416, Solar-Stellar Dynamos as Revealed by Helio- and Asteroseismology: GONG 2008/SOHO 21, ed. M. Dikpati, T. Arentoft, I. González Hernández, C. Lindsey, & F. Hill, 579

Guzik, J. A. & Mussack, K. 2010, ApJ, 713, 1108

Guzik, J. A. & Swenson, F. J. 1997, ApJ, 491, 967

Hanbury Brown, R., Davis, J., & Allen, L. R. 1967, MNRAS, 137, 375

Hanbury Brown, R. & Twiss, R. Q. 1956, Nature, 178, 1046

Haniff, C. 2007a, New Astronomy Review, 51, 565

Haniff, C. 2007b, New Astronomy Review, 51, 583

Hansen, C. J. & Kawaler, S. D. 1994, Stellar Interiors. Physical Principles, Structure, and Evolution., ed. Hansen, C. J. & Kawaler, S. D.

Hansen, C. J., Kawaler, S. D., & Trimble, V. 2004, Stellar interiors : physical principles, structure, and evolution, ed. Hansen, C. J., Kawaler, S. D., & Trimble, V.

Hauser, H. M. & Marcy, G. W. 1999, PASP, 111, 321

Hekker, S. & Aerts, C. 2010, A&A, 515, A43

Hoffleit, D. & Warren, J. W. H. 1995, VizieR Online Data Catalog: V/50, SIMBAD

Horch, E. P., Meyer, R. D., & van Altena, W. F. 2004, AJ, 127, 1727

Houdek, G. 2006, in ESA Special Publication, Vol. 624, Proceedings of SOHO 18/GONG 2006/HELAS I, Beyond the spherical Sun

Houdek, G., Balmforth, N. J., Christensen-Dalsgaard, J., & Gough, D. O. 1999, A&A, 351, 582

Houdek, G. & Gough, D. O. 2007, MNRAS, 375, 861

Howe, R. 2009, Living Reviews in Solar Physics, 6, 1

Hubrig, S., Nesvacil, N., Schöller, M., et al. 2005, A&A, 440, L37

Hummer, D. G. & Mihalas, D. 1988, ApJ, 331, 794

Iben, Jr., I. 1963, ApJ, 138, 452

Iben, Jr., I. 1965, ApJ, 142, 1447

Iben, Jr., I. & MacDonald, J. 1985, ApJ, 296, 540

Iglesias, C. A. & Rogers, F. J. 1996, ApJ, 464, 943

Jamar, C. 1978, A&A, 70, 379

Jamar, C., Macau-Hercot, D., Monfils, A., et al. 1976, Ultraviolet bright-star spectrophotometric catalogue. A compilation of absolute spectrophotometric data obtained with the Sky Survey Telescope (S2/68) on the European Astronomical Satellite TD-1, ed. Jamar, C., Macau-Hercot, D., Monfils, A., Thompson, G. I., Houziaux, L., & Wilson, R.

Johnson, H. L. 1966, ARA&A, 4, 193

Johnson, H. L. & Morgan, W. W. 1953, ApJ, 117, 313

Johnson, M. A., Betz, A. L., & Townes, C. H. 1974, Physical Review Letters, 33, 1617

Khan, A. L., Boschi, L., & Connolly, A., D. 2011, J. Geophys. Res., 116, B01301

Kharitonov, A. V., Tereshchenko, V. M., & Kniazeva, L. N. 1978, A spectrophotometric catalog of stars, ed. Kharitonov, A. V., Tereshchenko, V. M., & Kniazeva, L. N.

Kharitonov, A. V., Tereshchenko, V. M., & Knyazeva, L. N. 1988, The spectrophotometric catalogue of stars. Book of reference., ed. Kharitonov, A. V., Tereshchenko, V. M., & Knyazeva, L. N.

Kim, Y.-C., Fox, P. A., Demarque, P., & Sofia, S. 1996, ApJ, 461, 499

Kippenhahn, R. & Weigert, A. 1990, Stellar Structure and Evolution, ed. Kippenhahn, R. & Weigert, A.

Kjeldsen, H. & Bedding, T. R. 1995, A&A, 293, 87

Kjeldsen, H., Bedding, T. R., & Christensen-Dalsgaard, J. 2008, ApJL, 683, L175

Kjeldsen, H., Bedding, T. R., Viskum, M., & Frandsen, S. 1995, AJ, 109, 1313

Koch, D. G., Borucki, W. J., Basri, G., et al. 2010, ApJL, 713, L79

Kochukhov, O. & Bagnulo, S. 2006, A&A, 450, 763

Koornneef, J., Bohlin, R., Buser, R., Horne, K., & Turnshek, D. 1986, Highlights of Astronomy, 7, 833

Kurtz, D. W., Elkin, V. G., Cunha, M. S., et al. 2006, MNRAS, 372, 286

Kurtz, D. W., Elkin, V. G., & Mathys, G. 2007, MNRAS, 380, 741

Kurtz, D. W., Matthews, J. M., Martinez, P., et al. 1989, MNRAS, 240, 881

Labeyrie, A. 1975, ApJL, 196, L71

Latham, D. W., Brown, T. M., Monet, D. G., et al. 2005, in Bulletin of the American Astronomical Society, Vol. 37, American Astronomical Society Meeting Abstracts, #110.13

Lawson, P. R. 2000, in Principles of Long Baseline Stellar Interferometry, ed. P. R. Lawson, 325

Lazrek, M., Baudin, F., Bertello, L., et al. 1997, Sol. Phys., 175, 227

Leckrone, D. S. 1973, ApJ, 185, 577

Leckrone, D. S., Fowler, J. W., & Adelman, S. J. 1974, A&A, 32, 237

Leighton, R. B., Noyes, R. W., & Simon, G. W. 1962, ApJ, 135, 474

Maeder, A. 1975, A&A, 40, 303

Maeder, A. 2009, Physics, Formation and Evolution of Rotating Stars, ed. Maeder, A.

Martinez, P., Weiss, W. W., Nelson, M. J., et al. 1996, MNRAS, 282, 243

Mason, B. D., Wycoff, G. L., Hartkopf, W. I., Douglass, G. G., & Worley, C. E. 2001, AJ, 122, 3466

Mathur, S., Handberg, R., Campante, T. L., et al. 2011, ApJ, 733, 95

Mathur, S., Metcalfe, T. S., Woitaszek, M., et al. 2012, ApJ, 749, 152

Mazumdar, A., Basu, S., Collier, B. L., & Demarque, P. 2006, MNRAS, 372, 949

Metcalfe, T. S., Chaplin, W. J., Appourchaux, T., et al. 2012, ApJL, 748, L10

Metcalfe, T. S. & Charbonneau, P. 2003, Journal of Computational Physics, 185, 176

Metcalfe, T. S., Creevey, O. L., & Christensen-Dalsgaard, J. 2009, ApJ, 699, 373

Metcalfe, T. S., Monteiro, M. J. P. F. G., Thompson, M. J., et al. 2010, ApJ, 723, 1583

Michaud, G. & Proffitt, C. R. 1993, in Astronomical Society of the Pacific Conference Series, Vol. 40, IAU Colloq. 137: Inside the Stars, ed. W. W. Weiss & A. Baglin, 246

Michelson, A. A. & Pease, F. G. 1921, Apj, 53, 249

Miglio, A., Montalbán, J., Noels, A., & Eggenberger, P. 2008, MNRAS, 386, 1487

Mihalas, D., Dappen, W., & Hummer, D. G. 1988, ApJ, 331, 815

Mihalas, D., Hummer, D. G., Mihalas, B. W., & Daeppen, W. 1990, ApJ, 350, 300

Mitalas, R. 1972, ApJ, 177, 693

Molenda-Żakowicz, J., Latham, D. W., Catanzaro, G., Frasca, A., & Quinn, S. N. 2011, MNRAS, 412, 1210

Monnier, J. D. 2003, Reports on Progress in Physics, 66, 789

Montagner, J. P. & Roult, G. 2008, Journal of Physics Conference Series, 118, 012004

Monteiro, M. J. P. F. G., Christensen-Dalsgaard, J., & Thompson, M. J. 2000, MNRAS, 316, 165

Monteiro, M. J. P. F. G. & Thompson, M. J. 1998, in IAU Symposium, Vol. 185, New Eyes to See Inside the Sun and Stars, ed. F.-L. Deubner, J. Christensen-Dalsgaard, & D. Kurtz, 317

Morel, M. & Magnenat, P. 1978, A&AS, 34, 477

Morel, P. 1997, A&AS, 124, 597

Netopil, M., Paunzen, E., Maitzen, H. M., North, P., & Hubrig, S. 2008, A&A, 491, 545

North, J. R., Davis, J., Bedding, T. R., et al. 2007, MNRAS, 380, L80

Oke, J. B. 1965, ARA&A, 3, 23

Osaki, J. 1975, PASJ, 27, 237

Otí Floranes, H., Christensen-Dalsgaard, J., & Thompson, M. J. 2005, MNRAS, 356, 671

Parker, P. D. M. 1986, in Physics of the Sun. Volume 1, ed. P. A. Sturrock, T. E. Holzer, D. M. Mihalas, & R. K. Ulrich, Vol. 1, 15–32

Patience, J., White, R. J., Ghez, A. M., et al. 2002, ApJ, 581, 654

Perraut, K., Brandão, I., Mourard, D., et al. 2011, A&A, 526, A89

Perryman, M. A. C. & ESA, eds. 1997, ESA Special Publication, Vol. 1200, The HIPPARCOS and TYCHO catalogues. Astrometric and photometric star catalogues derived from the ESA HIPPARCOS Space Astrometry Mission

Pesnell, W. D. 1990, ApJ, 363, 227

Pinsonneault, M. H., An, D., Molenda-Żakowicz, J., et al. 2011, ArXiv e-prints

Provost, J., Mosser, B., & Berthomieu, G. 1993, A&A, 274, 595

Prugniel, P., Vauglin, I., & Koleva, M. 2011, A&A, 531, A165

Quirrenbach, A. 2001, ARA&A, 39, 353

Ramírez, I. & Meléndez, J. 2005, ApJ, 626, 446

Ramírez, I., Meléndez, J., & Asplund, M. 2009, A&A, 508, L17

Rawlinson, N., Pozgay, S., & Fishwick, S. 2010, Physics of the Earth and Planetary Interiors, 178, 101

Reese, D. R., Marques, J. P., Goupil, M. J., Thompson, M. J., & Deheuvels, S. 2012, A&A, 539, A63

Renson, P. & Manfroid, J. 2009, A&A, 498, 961

Renzini, A. 1987, A&A, 188, 49

Ribas, I., Jordi, C., & Giménez, Á. 2000, MNRAS, 318, L55

Rogers, F. J. & Nayfonov, A. 2002, ApJ, 576, 1064

Rogers, F. J., Swenson, F. J., & Iglesias, C. A. 1996, ApJ, 456, 902

Roxburgh, I. W. 2005, A&A, 434, 665

Roxburgh, I. W. & Vorontsov, S. V. 1999, in Astronomical Society of the Pacific Conference Series, Vol. 173, Stellar Structure: Theory and Test of Connective Energy Transport, ed. A. Gimenez, E. F. Guinan, & B. Montesinos, 257

Roxburgh, I. W. & Vorontsov, S. V. 2001, MNRAS, 322, 85

Roxburgh, I. W. & Vorontsov, S. V. 2003, A&A, 411, 215

Roxburgh, I. W. & Vorontsov, S. V. 2004, in ESA Special Publication, Vol. 538, Stellar Structure and Habitable Planet Finding, ed. F. Favata, S. Aigrain, & A. Wilson, 403–406

Roxburgh, I. W. & Vorontsov, S. V. 2007, MNRAS, 379, 801

Rufener, F. & Nicolet, B. 1988, A&A, 206, 357

Ryabchikova, T., Piskunov, N., Kochukhov, O., et al. 2002, A&A, 384, 545

Saio, H. 1975, Sci. Rep. Tohoku Univ. Eighth Ser., 58, 9

Scholz, M. 2003, in Society of Photo-Optical Instrumentation Engineers (SPIE) Conference Series, Vol. 4838, Society of Photo-Optical Instrumentation Engineers (SPIE) Conference Series, ed. W. A. Traub, 163–171

Scuflaire, R., Montalbán, J., Théado, S., et al. 2008, A&SS, 316, 149

Serenelli, A. M. & Basu, S. 2010, ApJ, 719, 865

Shao, M. & Staelin, D. H. 1980, Appl. Opt., 19, 1519

Smith, J. A., Tucker, D. L., Kent, S., et al. 2002, AJ, 123, 2121

Solano, E. 1998, in ESA Special Publication, Vol. 413, Ultraviolet Astrophysics Beyond the IUE Final Archive, ed. W. Wamsteker, R. Gonzalez Riestra, & B. Harris, 743

Soubiran, C., Le Campion, J.-F., Cayrel de Strobel, G., & Caillo, A. 2010a, A&A, 515, A111

Soubiran, C., Le Campion, J.-F., Cayrel de Strobel, G., & Caillo, A. 2010b, VizieR Online Data Catalog, 1, 2029

Strömgren, B. 1966, ARA&A, 4, 433

Tassoul, M. 1980, ApJS, 43, 469

Tokovinin, A. A. 1984, Pis ma Astronomicheskii Zhurnal, 10, 293

Torres, G. 2010, AJ, 140, 1158

Trampedach, R. 2007, in American Institute of Physics Conference Series, Vol. 948, Unsolved Problems in Stellar Physics: A Conference in Honor of Douglas Gough, ed. R. J. Stancliffe, G. Houdek, R. G. Martin, & C. A. Tout, 141–148

Trampedach, R. 2010, Ap&SS, 328, 213

Trampedach, R., Stein, R. F., Christensen-Dalsgaard, J., & Nordlund, Å. 1999, in Astronomical Society of the Pacific Conference Series, Vol. 173, Stellar Structure: Theory and Test of Connective Energy Transport, ed. A. Gimenez, E. F. Guinan, & B. Montesinos, 233

Turner, N. H., ten Brummelaar, T. A., McAlister, H. A., et al. 2001, AJ, 121, 3254

Unno, W. 1967, PASJ, 19, 140

Valenti, J. A. & Fischer, D. A. 2005, VizieR Online Data Catalog, 215, 90141

van Leeuwen, F., ed. 2007, Astrophysics and Space Science Library, Vol. 350, Hipparcos, the New Reduction of the Raw Data

Vandakurov, Y. V. 1967, AZh, 44, 786

Ventura, P., Zeppieri, A., Mazzitelli, I., & D'Antona, F. 1998, A&A, 334, 953

Vernazza, J. E., Avrett, E. H., & Loeser, R. 1976, ApJS, 30, 1

Vorontsov, S. V. 1988, in IAU Symposium, Vol. 123, Advances in Helio- and Asteroseismology, ed. J. Christensen-Dalsgaard & S. Frandsen, 151

Walker, G., Matthews, J., Kuschnig, R., et al. 2003, PASP, 115, 1023

Wamsteker, W. 1981, A&A, 97, 329

Wheeler, J. C., Sneden, C., & Truran, J. J. W. 1989, ARA&A, 27, 279

White, T. R., Bedding, T. R., Stello, D., et al. 2011, ApJL, 742, L3

Woitaszek, M., Metcalfe, T., & Shorrock, I. 2009, in Proceedings of the 5th Grid Computing Environments Workshop, p. 1-7

Wright, J. T., Marcy, G. W., Butler, R. P., & Vogt, S. S. 2004, ApJS, 152, 261

List of Publications

Peer-reviewed Publications

Huber, D., Ireland, M. J., Bedding, T. R., **Brandão, I. M.**, Piau, L., Maestro, V., White, T. R., Bruntt, H., Casagrande, L., Molenda-Żakowicz, J., Silva Aguirre, V., Sousa, S. G., Barclay, T., Burke, C. J., Chaplin, W. J., Christensen-Dalsgaard, J., Cunha, M. S., De Ridder, J., Farrington, C. D., Frasca, A., García, R. A., Gilliland, R. L., Goldfinger, P. J., Hekker, S., Kawaler, S. D., Kjeldsen, H., McAlister, H. A., Metcalfe, T. S., Miglio, A., Monteiro, M. J. P. F. G., Pinsonneault, M. H., Schaefer, G. H., Stello, D., Stumpe, M. C., Sturmann, J., Sturmann, L., ten Brummelaar, T. A., Thompson, M. J., Turner, N., Uytterhoeven, K., 2012, **Fundamental Properties of Stars Using Asteroseismology from Kepler and CoRoT and Interferometry from the CHARA Array**, *The Astrophysical Journal*, **32**, 17 (DOI:10.1088/0004-637X/760/1/32) [http://iopscience.iop.org/0004-637X/760/1/32/]

Mathur, S., Metcalfe, T. S., Woitaszek, M., Bruntt, H., Verner, G. A., Christensen-Dalsgaard, J., Creevey, O. L., Doğan, G., Basu, S., Karoff, C., Stello, D., Appourchaux, T., Campante, T. L., Chaplin, W. J., García, R. A., Bedding, T. R., Benomar, O., Bonanno, A., Deheuvels, S., Elsworth, Y., Gaulme, P., Guzik, J. A., Handberg, R., Hekker, S., Herzberg, W., Monteiro, M. J. P. F. G., Piau, L., Quirion, P.-O., Régulo, C., Roth, M., Salabert, D., Serenelli, A., Thompson, M. J., Trampedach, R., White, T. R., Ballot, J., **Brandão, I. M.**, Molenda-Żakowicz, J., Kjeldsen, H., Twicken, J. D., Uddin, K., Wohler, B., 2012, **A Uniform Asteroseismic Analysis of 22 Solar-type Stars Observed by Kepler**, *The Astrophysical Journal*, **749**, 152 (DOI:10.1088/0004-637X/749/2/152) [http://iopscience.iop.org/0004-637X/749/2/152/]

Metcalfe, T. S., Chaplin, W. J., Appourchaux, T., García, R. A., Basu, S., **Brandão, I.**, Creevey, O. L., Deheuvels, S., Doğan, G., Eggenberger, P., Karoff, C., Miglio, A., Stello, D., Yldz, M., Çelik, Z., Antia, H. M., Benomar, O., Howe, R., Régulo, C., Salabert, D., Stahn, T., Bedding, T. R., Davies, G. R., Elsworth, Y., Gizon, L., Hekker, S., Mathur, S., Mosser, B., Bryson, S. T., Still, M. D., Christensen-Dalsgaard, J., Gilliland, R. L., Kawaler, S. D., Kjeld-

sen, H., Ibrahim, K. A., Klaus, T. C., Li, J., 2012, **Asteroseismology of the Solar Analogs 16 Cyg A and B from Kepler Observations**, *The Astrophysical Journal Letters*, **748**, 10 (DOI:10.1088/2041-8205/748/1/L10) [http://iopscience.iop.org/2041-8205/748/1/L10/]

Creevey, O. L., Doğan, G., Frasca, A., Thygesen, A. O., Basu, S., Bhattacharya, J., Biazzo, K., **Brandão, I. M.**, Bruntt, H., Mazumdar, A., Niemczura, E., Shrotriya, T., Sousa, S. G., Stello, D., Subramaniam, A., Campante, T. L., Handberg, R., Mathur, S., Bedding, T. R., García, R. A., Régulo, C., Salabert, D., Molenda-Żakowicz, J., Quirion, P.-O., White, T. R., Bonanno, A., Chaplin, W. J., Christensen-Dalsgaard, J., Christiansen, J. L., Elsworth, Y., Fanelli, M. N., Karoff, C., Kinemuchi, K., Kjeldsen, H., Gai, N., Monteiro, M. J. P. F. G., Suárez, J. C., 2012, **Fundamental properties of five Kepler stars using global asteroseismic quantities and ground-based observations**, *Astronomy & Astrophysics*, **537**, 111 (DOI:10.1051/0004-6361/201117037) [http://www.aanda.org/index.php?option=com_article&access=doi&doi=10.1051/0004-6361/201117037&Itemid=129]

Brandão, I. M., Doğan, G., Christensen-Dalsgaard, J., Cunha, M. S., Bedding, T. R., Metcalfe, T. S., Kjeldsen, H., Bruntt, H., Arentoft, T.,2011, **Asteroseismic modelling of the solar-type subgiant star β Hydri**, *Astronomy & Astrophysics*, **527**, A37 (DOI:10.1051/0004-6361/201015370) [http://www.aanda.org/index.php?option=com_article&access=doi&doi=10.1051/0004-6361/201015370&Itemid=129]

Campante, T. L., Handberg, R., Mathur, S., Appourchaux, T., Bedding, T. R., Chaplin, W. J., Garca, R. A., Mosser, B., Benomar, O., Bonanno, A., Corsaro, E., Fletcher, S. T., Gaulme, P., Hekker, S., Karoff, C., Régulo, C., Salabert, D., Verner, G. A., White, T. R., Houdek, G., **Brandão, I. M.**, Creevey, O. L., Doğan, G., Bazot, M., Christensen-Dalsgaard, J., Cunha, M. S., Elsworth, Y., Huber, D., Kjeldsen, H., Lundkvist, M., Molenda-Żakowicz, J., Monteiro, M. J. P. F. G., Stello, D., Clarke, B. D., Girouard, F. R., Hall, J. R., 2011, **Asteroseismology from multi-month Kepler photometry: the evolved Sun-like stars KIC 10273246 and KIC 10920273**, *Astronomy & Astrophysics* , **534**, 6 (DOI:10.1051/0004-6361/201116620) [http://www.aanda.org/index.php?option=com_article&access=doi&doi=10.1051/0004-6361/201116620&Itemid=129]

Kurtz, D. W., Cunha, M. S., Saio, H., Bigot, L., Balona, L. A., Elkin, V. G., Shibahashi, H., **Brandão, I. M.**, Uytterhoeven, K., Frandsen, S., Frimann, S., Hatzes, A., Lueftinger, T., Gruberbauer, M., Kjeldsen, H., Christensen-Dalsgaard, J., Kawaler, S. D., 2011, **The first evidence for multiple pulsation axes: a new rapidly oscillating Ap star in the Kepler field, KIC 10195926**, *Monthly Notices of the Royal Astronomical Society*, **414**, 2550

(DOI:10.1111/j.1365-2966.2011.18572.x) [http://onlinelibrary.wiley.com/doi/10.1111/j.1365-2966.2011.18572.x/abstract]

Mathur, S., Handberg, R., Campante, T. L., García, R. A., Appourchaux, T., Bedding, T. R., Mosser, B., Chaplin, W. J., Ballot, J., Benomar, O., Bonanno, A., Corsaro, E., Gaulme, P., Hekker, S., Régulo, C., Salabert, D., Verner, G., White, T. R., **Brandão, I. M.**, Creevey, O. L., Doğan, G., Elsworth, Y., Huber, D., Hale, S. J., Houdek, G., Karoff, C., Metcalfe, T. S., Molenda-Żakowicz, J., Monteiro, M. J. P. F. G., Thompson, M. J., Christensen-Dalsgaard, J., Gilliland, R. L., Kawaler, S. D., Kjeldsen, H., Quintana, E. V., Sanderfer, D. T., Seader, S. E., 2011, **Solar-like Oscillations in KIC 11395018 and KIC 11234888 from 8 Months of Kepler Data**, *The Astrophysical Journal*, **733**, 95 [DOI:10.1088/0004-637X/733/2/95] (http://iopscience.iop.org/0004-637X/733/2/95/)

Cunha, M. S., **Brandão**, 2011, **Probing tiny convective cores with the acoustic modes of lowest degree**, *Astronomy & Astrophysics*, **529**, 10 (DOI: 10.1051/0004-6361/201015188) [http://www.aanda.org/index.php?option=com_article&access=doi&doi=10.1051/0004-6361/201015188&Itemid=129]

Chaplin, W. J., Kjeldsen, H., Christensen-Dalsgaard, J., Basu, S., Miglio, A., Appourchaux, T., Bedding, T. R., Elsworth, Y., García, R. A., Gilliland, R. L., Girardi, L., Houdek, G., Karoff, C., Kawaler, S. D., Metcalfe, T. S., Molenda-Żakowicz, J., Monteiro, M. J. P. F. G., Thompson, M. J., Verner, G. A., Ballot, J., Bonanno, A., **Brandão**, Broomhall, A.-M., Bruntt, H., Campante, T. L., Corsaro, E., Creevey, O. L., Doğan, G., Esch, L., Gai, N., Gaulme, P., Hale, S. J., Handberg, R., Hekker, S., Huber, D., Jiménez, A., Mathur, S., Mazumdar, A., Mosser, B., New, R., Pinsonneault, M. H., Pricopi, D., Quirion, P.-O., Régulo, C., Salabert, D., Serenelli, A. M., Silva Aguirre, V., Sousa, S. G., Stello, D., Stevens, I. R., Suran, M. D., Uytterhoeven, K., White, T. R., Borucki, W. J., Brown, T. M., Jenkins, J. M., Kinemuchi, K., Van Cleve, J., Klaus, T. C., 2011, **Ensemble Asteroseismology of Solar-Type Stars with the NASA Kepler Mission**, *Science*, **332**, 213 (DOI:10.1126/science.1201827) [http://www.sciencemag.org/content/332/6026/213]

Perraut, K., **Brandão, I.**, Mourard, D., Cunha, M., Bério, Ph., Bonneau, D., Chesneau, O., Clausse, J. M., Delaa, O., Marcotto, A., Roussel, A., Spang, A., Stee, Ph., Tallon-Bosc, I., McAlister, H., Ten Brummelaar, T., Sturmann, J., Sturmann, L., Turner, N., Farrington, C., Goldfinger, P. J., 2011, **The fundamental parameters of the roAp star γ Equulei**, *Astronomy & Astrophysics*, **526**, A89 (DOI:10.1051/0004-6361/201015801) [http://www.aanda.org/index.php?option=com_article&access=doi&doi=10.1051/0004-6361/201015801&Itemid=129]

Balona, L. A., Cunha, M. S., Kurtz, D. W., **Brandão, I.**, Gruberbauer, M., Saio, H., Östensen, R., Elkin, V. G., Borucki, W. J., Christensen-Dalsgaard, J., Kjeldsen, H., Koch, D. G., Bryson, S. T., 2011, **Kepler observations of rapidly oscillating Ap, δ Scuti and γ Doradus pulsations in Ap stars**, *Monthly Notices of the Royal Astronomical Society*, **410**, 517-534 (DOI:10.1111/j.1365-2966.2010.17461.x) [http://onlinelibrary.wiley.com/doi/10.1111/j.1365-2966.2010.17461.x/abstract]

Chaplin, W. J., Appourchaux, T., Elsworth, Y., García, R. A., Houdek, G., Karoff, C., Metcalfe, T. S., Molenda-Żakowicz, J., Monteiro, M. J. P. F. G., Thompson, M. J., Brown, T. M., Christensen-Dalsgaard, J., Gilliland, R. L., Kjeldsen, H., Borucki, W. J., Koch, D., Jenkins, J. M., Ballot, J., Basu, S., Bazot, M., Bedding, T. R., Benomar, O., Bonanno, A., **Brandão, I.**, Bruntt, H., Campante, T. L., Creevey, O. L., Di Mauro, M. P., Doğan, G., Dreizler, S., Eggenberger, P., Esch, L., Fletcher, S. T., Frandsen, S., Gai, N., Gaulme, P., Handberg, R., Hekker, S., Howe, R., Huber, D., Korzennik, S. G., Lebrun, J. C., Leccia, S., Martic, M., Mathur, S., Mosser, B., New, R., Quirion, P.-O., Régulo, C., Roxburgh, I. W., Salabert, D., Schou, J., Sousa, S. G., Stello, D., Verner, G. A., Arentoft, T., Barban, C., Belkacem, K., Benatti, S., Biazzo, K., Boumier, P., Bradley, P. A., Broomhall, A.-M., Buzasi, D. L., Claudi, R. U., Cunha, M. S., D'Antona, F., Deheuvels, S., Derekas, A., García Hernández, A., Giampapa, M. S., Goupil, M. J., Gruberbauer, M., Guzik, J. A., Hale, S. J., Ireland, M. J., Kiss, L. L., Kitiashvili, I. N., Kolenberg, K., Korhonen, H., Kosovichev, A. G., Kupka, F., Lebreton, Y., Leroy, B., Ludwig, H.-G., Mathis, S., Michel, E., Miglio, A., Montalbn, J., Moya, A., Noels, A., Noyes, R. W., Pall, P. L., Piau, L., Preston, H. L., Roca Cortés, T., Roth, M., Sato, K. H., Schmitt, J., Serenelli, A. M., Silva Aguirre, V., Stevens, I. R., Suárez, J. C., Suran, M. D., Trampedach, R., Turck-Chièze, S., Uytterhoeven, K., Ventura, R., Wilson, P. A., 2010, **The Asteroseismic Potential of Kepler: First Results for Solar-Type Stars**, *The Astrophysical Journal Letters*, **713**, L169-L175 (DOI:10.1088/2041-8205/713/2/L169) []

Bruntt, H., Kervella, P., Mérand, A., **Brandão, I.**, Bedding, T. R., Ten Brummelaar, T. A., Coudé Du Foresto, V., Cunha, M. S., Farrington, C., Goldfinger, P. J., Kiss, L. L., McAlister, H. A., Ridgway, S. T., Sturmann, J., Sturmann, L., Turner, N., Tuthill, P. G., 2010, **The radius and effective temperature of the binary Ap star β CrB from CHARA/FLUOR and VLT/NACO observations**, *Astronomy & Astrophysics*, **512**, A55 (DOI:10.1051/0004-6361/200913405) [http://www.aanda.org/index.php?option=com_article&access=doi&doi=10.1051/0004-6361/200913405&Itemid=129]

Bruntt, H., Kurtz, D., Cunha, M. S., **Brandão, I.**, Handler, G., Bedding, T. R., Medupe, T., Buzasi, D. L., Mashigo, D., Zhang, I., van Wyk, F., 2009, **Asteroseismic analysis of the roAp star α Circini: 84 days of high precision photometry from the WIRE satellite**, *Monthly Notices of the Royal Astronomical Society*, **396**, 1189-1201 (DOI:10.1111/j.1365-2966.2009.14804.x) [http://onlinelibrary.wiley.com/doi/10.1111/j.1365-2966.2009.14804.x/abstract]

Bruntt, H., North, J. R., Cunha, M. S., **Brandão, I.**, Elkin, V. G., Kurtz, D., Davis, J., Bedding, T. R., Jacob, A. P., Owens, S. M., Robertson, J. G., Tango, W. J. Tuthill, P. G., Ireland, M. J. and Gameiro, J. F., 2008, **The fundamental parameters of the roAp star α Circini**, *Monthly Notices of the Royal Astronomical Society*, **386**, 2039-2046 (DOI:10.1111/j.1365-2966.2008.13167.x) [http://onlinelibrary.wiley.com/doi/10.1111/j.1365-2966.2008.13167.x/abstract]

Refereed Proceedings

Mathur, S., Campante, T. L., Handberg, R., García, R. A., Appourchaux, T., Bedding, T. R., Mosser, B., Chaplin, W. J., Ballot, J., Benomar, O., Bonanno, A., Corsaro, E., Gaulme, P., Hekker, S., Régulo, C., Salabert, D., Verner, G., White, T. R., **Brandão, I.**, Creevey, O. L., Doğan, G., Bazot, M., Cunha, M. S., Elsworth, Y., Huber, D., Hale, S. J., Houdek, G., Karoff, C., Lundkvist, M., Metcalfe, T. S., Molenda-Żakowicz, J., Monteiro, M. J. P. F. G., Thompson, M. J., Stello, D., Christensen-Dalsgaard, J., Gilliland, R. L., Kawaler, S. D., Kjeldsen, H., Clarke, B. D., Girouard, F. R., Hall, J. R., Quintana, E. V., Sanderfer, D. T., Seader, S. E., 2012, **Seismic Analysis of Four Solar-like Stars Observed during More Than Eight Months by Kepler**, *Astronomical Society of the Pacific*, **462**, 180 [http://aspbooks.org/custom/publications/paper/462-0180.html]

Kurtz, D. W., Cunha, M. S., Saio, H., Bigot, L., Balona, L. A., Elkin, V. G., Shibahashi, H., **Brandão, I.**, Uytterhoeven, K.: Frandsen, S., Frimann, S., Hatzes, A., Lueftinger, T., Gruberbauer, M., Kjeldsen, H., Christensen-Dalsgaard, J., Kawaler, S. D., 2012, **The First Evidence for Multiple Pulsation Axes: A New roAp Star in the Kepler Field, KIC 10195926**, *Astronomical Society of the Pacific*, **462**, 125 [http://aspbooks.org/custom/publications/paper/462-0125.html]

Doğan, G., **Brandão, I. M.**, Bedding, T. R., Christensen-Dalsgaard, J., Cunha, M. S., Kjeldsen, H., 2010, **Asteroseismic modelling of the solar-like star β Hydri**, *Astrophysics and Space Science*, **328**, 101-104 (DOI:10.1007/s10509-009-0225-1) [http://link.springer.com/

article/10.1007%2Fs10509-009-0225-1#]

Brandão, I. M., Cunha, M. S., Creevey, O. L., Christensen-Dalsgaard, J., 2010, **Seismic signatures of stellar cores of solar-like pulsators: Dependence on mass and age**, *Astronomische Nachrichten*, **331**, 940 (DOI:10.1002/asna.201011431) [http://onlinelibrary.wiley.com/doi/10.1002/asna.201011431/abstract]

Cunha, M. S., **Brandão, I. M.**, 2010, **Probing the cores of solar-like pulsators**, *Astronomische Nachrichten,* **331**, 925 (DOI:10.1002/asna.201011428) [http://onlinelibrary. wiley.com/doi/10.1002/asna.201011428/abstract]

Brandão, I. M., Bruntt, H., Cunha, M., Kurtz, W. D., 2008, **Interferometric and seismic constraints on the roAp star α Cir**, *Communications in Asteroseismology*, **157**, 234-238, [http://adsabs.harvard.edu/abs/2008CoAst.157..234B]

Brandão, I. M., Cunha, M. S., Gameiro, J. F., 2008, **Bolometric correction of the roAp star α Cir**, *Contributions of the Astronomical Observatory Skalnaté Pleso*, **38**, 397-398 [http://adsabs.harvard.edu/abs/2008CoSka..38..397B]

List of Communications

Contributed talks in Conferences

An in-depth asteroseismic study on the Kepler target KIC 10273246, in 4th KASC Workshop: From unprecedented data to revolutionary science, 11-15 July, 2011, Boulder, Colorado, USA [http://kasc.hao.ucar.edu/]

KIC 8677585: Possibly the first Ap star with roAp and γ Dor pulsations, in 3rd Kepler Asteroseismology Workshop: Kepler Asteroseismology in Action, 14-18 June, 2010, Aarhus, Denmark [http://phys.au.dk/kascIII]

Seismic signatures of stellar cores of solar-like pulsators: dependence on mass and age, in 4th HELAS International Conference - Seismological Challenges for Stellar Structure, 1-5 February, 2010, Lanzarote (Canary Islands, Spain) [http://www.iac.es/congreso/helas4/]

Interferometric and seismic contraints on the roAp star α Cir, in 18 Encontro Nacional de Astronomia e Astrofísica, Évora, Portugal, 18-19 September, 2008 [http://enaa2008.multimeios.pt/]

Interferometric and seismic contraints on the roAp star α Cir, in WrocÅaw HELAS Workshop Interpretation of Asteroseismic data, Wrocław, Poland, 23-27 de June, 2008 [http://seismo.astro.uni.wroc.pl/].

Posters in Conferences

Gülnur Doğan, Travis S. Metcalfe, Patrick Eggenberger, Sébastien Deheuvels, Maria Pia Di Mauro, Mário J. Monteiro, **Isa M. Brandão**, Orlagh Creevey, and KASC WG1 members, **Asteroseismic analysis of two solar-like subgiants: KIC 11395018 (Boogie) and KIC 10920273 (Scully)**, 4th KASC Workshop: From unprecedented data to revolutionary

science, 11-15 July, 2011, Boulder, Colorado, USA [http://kasc.hao.ucar.edu/]

Brandão, I. M., Cunha, M. S., Creevey, O. L., Christensen-Dalsgaard, J., **A first step towards the age determination of solar-like stars with asteroseismology**, Cool Stars 16, 29 August - 2 September, 2010, Seattle, Washington, USA [https://www.confcon.com/coolstars16/]

Creevey, O. L., Doğan, G., **Brandão, I. M.**, Metcalfe, T., Monteiro, M. J., Thompson, M. J., Molenda-Żakowicz, J., Chaplin, W. J., **The characters of (sun-like) stars**, 3rd Kepler Asteroseismology Workshop: Kepler Asteroseismology in Action, 14-18 June, 2010, Aarhus, Denmark [http://phys.au.dk/kascIII]

H. Bruntt , **I. M. Brandão**, Pierre Kervella , M. Cunha, D.W. Kurtz , T. Bedding , D. Buzasi, **Empirical correction of the temperature scale of Ap stars**, XXVIIth IAU General Assembly, JD4, 3-14 August, 2009, Rio de Janeiro, Brasil [http://www.astronomy2009.com.br/]

Cunha, M. S., **Brandão, I. M.**, Metcalfe, T. S., **Inference from small convective cores from space-based data**, em HELAS-NA5 workshop: Synergies between solar and stellar modelling, 22-26 June, 2009, Rome, Italy [http://www.helas-eu.org/workshops/roma/]

Doğan, G., **Brandão, I. M.**, Bedding, T. R., Bruntt, H., Christensen-Dalsgaard, J., Cunha, M. S., Kjeldsen, H., **Asteroseismic Modelling of the solar-like star β Hyi**, em HELAS-NA5 workshop: Synergies between solar and stellar modelling, 22-26 June, 2009, Rome, Italy [http://www.helas-eu.org/workshops/roma/]

Brandão, I. M., Dougan, G., Bedding, T. R., Bruntt, H., Christensen-Dalsgaard, J., Cunha, M. S., Kjeldsen, H., **Asteroseismic Modelling of β Hyi**, em First CoRoT International Symposium From stars to habitable planets, 2-5 January, 2009, Paris, France [http://www.symposiumcorot2009.fr/]

Cunha, M. S., **Brandão, I. M.**, Metcalfe, T. S., **On extracting signatures of small convective cores from space-based data**, em First CoRoT International Symposium From stars to habitable planets, 2-5 January, 2009, Paris, France [http://www.symposiumcorot2009.fr/]

Brandão, I. M., Cunha, M. S., Gameiro, J. F., **Bolometric Correction of the roAp star α Cir**, CP#AP Workshop 2007, 10-14 September, 2007, Vienna, Austria [http://www.univie.ac.at/cpworkshop2007/]

Brandão, I. M., Cunha, M. S., Gameiro, J. F., **Bolometric Correction of the roAp star α Cir**, in 17º Encontro Nacional de Astronomia e Astrofísica, 19-20 July, 2007, Porto, Portugal [http://www.astro.up.pt/investigacao/conferencias/xviienaa/index.php?opt=inicio]